Thermal Transport, Thermal Protrusion, and Thermally-Induced Material Transfer in the Head-Disk Interface of Heat-Assisted Magnetic Recording

by

Qilong Cheng

A dissertation submitted in partial satisfaction of the

requirements for the degree of

Doctor of Philosophy

in

Engineering - Mechanical Engineering

in the

Graduate Division

of the

University of California, Berkeley

Committee in charge:

Professor David B. Bogy, Chair
Professor Christopher Dames
Professor Per-Olof Persson

Fall 2021

Thermal Transport, Thermal Protrusion, and Thermally-Induced Material Transfer in the Head-Disk Interface of Heat-Assisted Magnetic Recording

Abstract

Thermal Transport, Thermal Protrusion, and Thermally-Induced Material Transfer in the Head-Disk Interface of Heat-Assisted Magnetic Recording

by

Qilong Cheng

Doctor of Philosophy in Engineering - Mechanical Engineering

University of California, Berkeley

Professor David B. Bogy, Chair

As data generated worldwide are growing explosively, it is crucial to increase the areal density of traditional storage devices to satisfy the requirements. Conventional hard disk drive (HDD) technology, perpendicular magnetic recording (PMR), has reached the superparamagnetic limit of ~ 1 Tb/in^2. To realize the areal density over 1 Tb/in^2, the size of the media bits must be further decreased to tens of nanometers, which requires high coercivity magnetic media. The high coercivity can avoid superparamagnetism and thus store data safely at the small bit size under room temperature, but it makes data writing challenging. To assist the writing process, energy is input to the media to lower its coercivity temporarily. Current technologies such as heat-assisted magnetic recording (HAMR) and microwave-assisted magnetic recording (MAMR) utilize two different methods to lower the coercivity. HAMR integrates a laser to locally heat the media to its Curie temperature (400–500 °C), while MAMR uses a spin torque oscillator to induce ferromagnetic resonance in the media grains.

In the HAMR head-disk interface (HDI), a recording head flies over a rotating disk with a relative velocity of 5–40 m/s and an initial spacing of 10–15 nm controlled by an air bearing. Then, the spacing is reduced by energizing a joule heater inside the head. The heater generates a protrusion on the head surface to lower the initial spacing to 1–2 nm so that data reading/writing can be performed using the read/write transducers in the head. The head is also integrated with a laser diode, a waveguide (WG) and a near-field transducer (NFT) for laser delivery. The laser beam is launched from the recording head and is focused on the recording disk to locally heat the disk (400–500 °C), which is even hotter than the head temperature (150–250 °C). Therefore, the head-disk interface of HAMR is a system that combines nanoscale spacing (< 15 nm), high temperatures (head $\sim$ 150–250 °C, disk $\sim$ 400–500 °C), steep thermal gradient (~ 10 K/nm), and a high-speed sliding condition (5–40 m/s). Furthermore, the introduction of the laser affects thermal transport and thermal protrusion, and causes thermally-induced material transfer in the interface, which needs to

be investigated both for fundamental understanding and for practical applications such as HAMR and other microelectronics devices.

To study the thermal transport across a closing gap between the head and the disk, we conducted static touchdown experiments using a custom-made setup where the disk is not rotating to exclude the air cooling effect. The head temperature rise was measured as a function of the heater power under various conditions such as different substrate materials, relative humidity and laser on/off. An enhanced thermal transport due to phonon heat conduction is observed for the gap $< \sim 2$ nm. The thermal transport across the gap becomes stronger when a better thermal conductor is used as the substrate or when the humidity is higher than 75%. With the presence of the laser, the head undergoes a joule heat dissipation inside the head and a back-heating from the hot spot on the substrate.

In the HAMR operations, the laser delivery involves energy loss, which leads to a localized angstrom-level laser-induced protrusion (LIP) and a fly height change (FHC). They need to be considered and compensated in the spacing control. Flying touchdown experiments were performed to evaluate their overall effect on the spacing change, then they were separated using their different time constants in microseconds and milliseconds. In addition, HAMR operations may utilize two heaters in the head. It is demonstrated that the head protrusion shape can be modulated by use of the dual heaters, and that the touchdown area can be controlled precisely.

During the laser exposure under HAMR operations, material transfer also happens due to the high level of thermal transport. The temperature of the hot spot on the disk is much higher than the lubricant evaporation temperature, so the lubricant is evaporated from the disk and then condenses on the head surface. The material accumulation on the head surface, also known as smear, is a challenging reliability issue for HAMR. We experimentally investigate the smear formation mechanism and propose two smear mitigation strategies. The results show that the smear forms when the lubricant evaporation occurs for a certain time, and that the smear can be mitigated by a mechanical burnishing approach or a thermal approach.

Next, we report a thermal mapping technique using a phase change material $Ge_2Sb_2Te_5$. $Ge_2Sb_2Te_5$ undergoes a crystalline transition at 149 °C with changes in its density and optical reflectivity. By use of these changes, we can map surface temperatures from nanoscale to microscale with minimal calibration, which is demonstrated using a recording head.

Finally, we propose a near-field thermal transport based scheme for lubricant thickness measurement. The thermal effect of the lubricant is investigated when the head approaches the disk in the flying touchdown experiments, which is then used to determine the lubricant thickness. Most previous lubricant measurements require an ex-situ tool such as optical surface analyzer (OSA), but the proposed scheme is an in-situ method with a sub-angstrom resolution and a faster response time. Using the scheme, we performed in-situ measurements of the lubricant depletion and reflow dynamics under HAMR operations.

To my parents, Huoping Cheng and Ru Wang

Human effort is the decisive factor.

Contents

List of Figures

List of Tables

List of Abbreviations

ABS	air bearing surface
AE	acoustic emission
AFM	atomic force microscopy
ASRC	Advanced Storage Research Consortium
CML	Computer Mechanics Laboratory
CW	continuous wave
DAQ	data acquisition
ECS	embedded contact sensor
ePMR	energy-assisted perpendicular magnetic recording
FCC	face-centered cubic
FHC	fly height change
HAMR	heat-assisted magnetic recording
HDD	hard disk drive
HDI	head-disk interface
HGA	head gimbal assembly
HMS	head-media spacing
HTC	heat transfer coefficient
LDV	laser Doppler velocimetry
LIP	laser-induced protrusion
MAMR	microwave-assisted magnetic recording
NFT	near-field transducer
OSA	optical surface analyzer
PCTC	phase change temperature contour
PFPE	perfluoropolyether
PMR	perpendicular magnetic recording
RH	relative humidity
RMS	root mean square
SEM	scanning electron microscopy
STEM	scanning transmission electron microscopy
SThM	scanning thermal microscopy
SSD	solid state drive
TCR	temperature coefficient of resistance

TD	touchdown
TDP	touchdown power
TDS	touchdown sensor
TEM	transmission electron microscopy
TFC	thermal fly-height control
TGA	thermogravimetric analysis
VCM	voice coil motor
vdW	van der Waals
WG	waveguide

Acknowledgments

My life over the past years has been a unique and colorful journey, and I would like to express my gratitude to all the people who helped me throughout my doctoral study.

First and foremost, I would like to sincerely thank my advisor, Prof. David B. Bogy, for his continuous support and guidance during my PhD study at UC Berkeley. I still remember the moment that he interviewed me when I was an undergraduate student and the moment that I got the doctoral offer from him. It is my fortune to have him as my advisor and work with him on the state-of-the-art research. I have learnt a lot from him on how to conduct research and how to manage a lab, which will absolutely benefit me in my future career. He is also a life mentor to me. Our discussions about academia, technology, politics and lifestyle always interest me and influence me. I also enjoyed our boat sailing on his REVELATION. He is undoubtedly the best advisor that I could wish for.

I would also like to thank Prof. Christopher Dames and Prof. Per-Olof Persson for serving on my qualifying exam committee and reviewing my dissertation. My gratitude also goes to Prof. Panayiotis Papadopoulos and Prof. Tarek Zohdi for serving on my qualifying exam committee. I also enjoyed taking courses at Berkeley, and I am grateful to all my teachers, including but not limited to the aforementioned professors and Profs. David Steigmann, Ömer Savaş and Lin Lin.

I want to thank all my colleagues at Computer Mechanics Laboratory (CML). I have enjoyed the collaborative atmosphere to learn from each other. It is my great pleasure to work with them: Yuan Ma, Haoyu Wu, Amin Ghafari, Siddhesh Sakhalkar, Yueqiang Hu, Roshan Mathew Tom, Yuying Wu and Dr. Bair Budaev. I would like to especially thank Yuan and Haoyu for sharing their experimental experience. Also, I want to thank Amin, Siddhesh and Roshan for contributing to our joint research projects, where Amin worked on the heat transfer models and computations, Siddhesh and Roshan performed the thermo-mechanical simulations, and I worked on the experiments.

My research projects in this dissertation could not have been accomplished without the support of the Advanced Storage Research Consortium (ASRC) and Western Digital. I would like to thank Sukumar Rajauria, Robert Smith, Erhard Schreck, Tan Trinh, Qing Dai, Shaomin Xiong and JP Peng of Western Digital and Huan Tang of Seagate for helpful discussions during ASRC review meetings and CML Sponsors' Meetings. Besides, I was fortunate to work as an intern at Western Digital in Summer 2018 and Summer 2020. I would like to thank Qing for offering me the position and thank Sukumar, Robert, Erhard, Tan, Na Wang and Jim Reiner for their help and support during the internship.

I would like to thank my friends at Berkeley: Bike Zhang, Shuxiao Chen, Xu Shen, Jieqiong Wang, Ruiqi Guo, Tongge Wu and Wenying Qiu. They brought much fun to my life at Berkeley. I also want to thank my friends in the mobile game Wang Zhe Rong Yao.

Finally, I want to thank my parents Huoping Cheng and Ru Wang for giving me life and raising me up. My accomplishment would have been impossible without their unconditional love, encouragement and support.

Chapter 1

Introduction

Human history has shifted from industrial production to an era where everything is relevant to information and computerization, which is also known as the Information Age. Data is indispensable and plays an essential role in people's lives. Meanwhile, the data generated worldwide are growing explosively and are expected to grow more rapidly in the future. According to the International Data Corporation, the global datasphere, which refers to the total amount of data created and consumed, will increase from 40 ZB in 2019 to 175 ZB in 2025 (1 ZB (zettabyte) = 10^9 TB (terabyte)) [1]. The storage for such a huge amount of data can be roughly classified into two categories - hard disk drives (HDDs) and NAND flash (including NAND flash based solid state drives (SSDs), memory cards, USB flash drives, etc.) An IBM report shows that the price-per-GB of HDD is one ninth that of NAND in 2018, and that the percentages of total manufactured storage for HDDs and NAND in 2018 were 76% and 20%, respectively [2]. Despite SSDs' increasing popularity in personal data storage such as laptops and smartphones, HDDs are still the major storage medium in data centers due to their low cost and longevity.

Conventional HDD technology, perpendicular magnetic recording (PMR), has reached the superparamagnetic limit of ~ 1 Tb/in^2 (areal density). To satisfy the storage requirements for worldwide explosive data growth, a new technology called heat-assisted magnetic recording (HAMR) has been proposed to realize a higher areal density [3–6]. HAMR technology uses high coercivity magnetic media with the bit size as small as tens of nanometers, and it integrates a laser to heat the media to assist data writing. The head-disk interface (HDI) of HAMR is a system that combines nanoscale spacing, high temperatures, steep thermal gradient, and a high-speed sliding condition. Furthermore, the introduction of the laser affects thermal transport and thermal protrusion, and causes thermally-induced material transfer in the interface. In this dissertation, experiments were performed to study these issues for fundamental understanding and for practical applications.

This chapter serves as an introduction to the dissertation. Section 1.1 discusses the basics of HDDs. Section 1.2 introduces HAMR technology and its existing reliability issues. The objective of this dissertation is demonstrated in Section 1.3. The organization and novel contributions of this dissertation are presented in Section 1.4.

1.1 Hard disk drive

The internal view of an HDD is shown in Figure 1.1 (image by cabrard on pixabay.com, with permission of Pixabay License). An HDD consists of a spindle, a head attached to a suspension, an actuator arm, a disk, a voice coil motor (VCM), etc. The spindle rotates the disk at a designed speed (typically 5400–10000 RPM). The disk stores binary data in the form of magnetic bits, which contain tens of grains with "up" or "down" magnetic orientation. The head flies over the rotating disk and contains read/write transducers (also termed as reader/writer) to perform data reading/writing. Data reading determines the "up" or "down" magnetic orientation in the magnetic bits, while data writing magnetizes the bits to "up" or "down" orientation by use of the head magnetic field. The head is attached to the end of the suspension, which is connected to the actuator arm. The data reading/writing commands in the HDD are sent and processed via the VCM.

Figure 1.1: Internal view of a hard disk drive (HDD).

The data are stored in circular tracks on the disk. Figure 1.2 shows the data reading/writing process in the HDD. During this operation, the computer gives commands of data reading or writing to the circuit board that includes the VCM. Then the circuit board instructs the actuator arm to move to the exact radial location, and assigns the head to read the data from the disk or write the data to the disk. The signals acquired by the head are sent back to the computer via the circuit board.

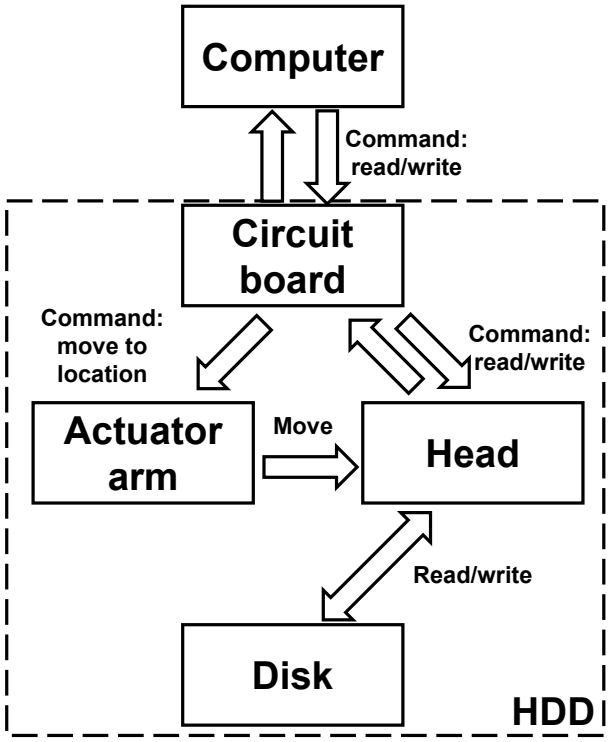

Figure 1.2: Data reading/writing process in HDD.

The data reading and writing are performed using the recording head. Figure 1.3 shows optical images of a recording head and its air bearing surface (ABS). The device in Figure 1.3(a) is also called a head gimbal assembly (HGA), which consists of flexible cables, a suspension and a slider. The flexible cables connect the components in the head with the circuit board in the HDD. The suspension is attached to the actuator arm such that the head can move with the arm. The slider is a small block that flies over the rotating disk. The slider is coupled to the suspension through a gimbal assembly, allowing its pitch and roll motions to follow the topography of the disk surface [7]. The surface of the slider facing the disk is called the air bearing surface (ABS) as shown in Figure 1.3(b). The ABS is specially designed with complex patterns to control the nanoscale spacing from the disk. When the slider comes closer to the rotating disk, the air between the slider and the disk is compressed

and forms an air bearing with a pressure distribution determined by the ABS profile. The high-pressure air bearing lifts the slider from the disk surface and thus the slider can fly over the rotating disk. The disk moving direction is denoted in Figure 1.3(b). The bottom edge of the slider that faces the oncoming disk is called the leading edge, while the opposite edge is called the trailing edge. The spacing between the trailing edge of the ABS and the disk surface is $\sim$ 10–15 nm in current HDDs. The read/write area is also located near the trailing edge on the ABS.

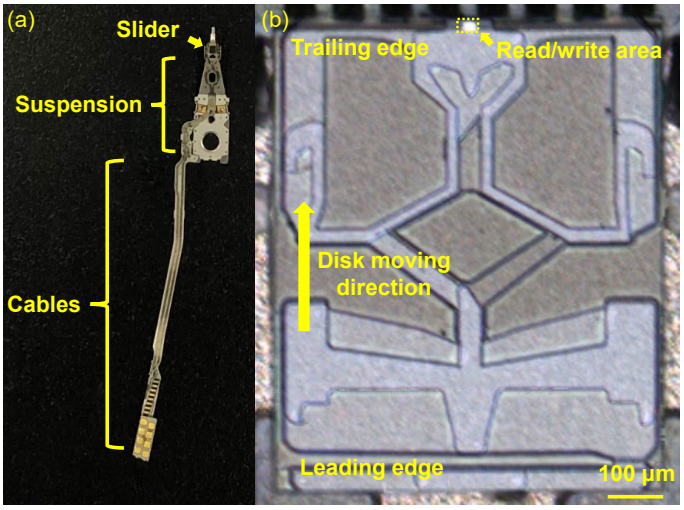

Figure 1.3: Optical images of (a) a recording head and (b) the air bearing surface (ABS).

Figure 1.4 shows the multilayer disk structure. The disk has a magnetic layer that is $\sim$ 100 nm thick on an AlMg or glass substrate. The magnetic layer is coated with a carbon overcoat (protective layer, $\sim$ 2 nm thick) and a molecular layer of perfluoropolyether (PFPE) lubricant ($\sim$ 1 nm thick) [4, 8]. Common PFPE lubricants used on the disk are Zdol, Ztetraol and Ztetraol multidentate [9–12]. They have a Z-type backbone chain, but with different

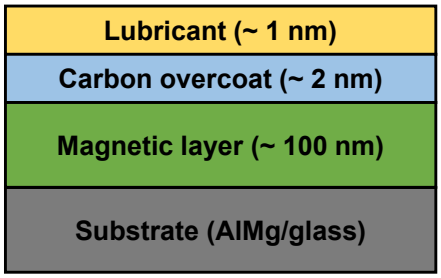

Figure 1.4: Multilayer disk structure.

end groups. The lubricant improves the high-speed tribological performance by passivating the surface against contamination, minimizing friction, and preventing corrosion [4, 13, 14].

The interface between the head and the disk is called the head-disk interface (HDI). Figure 1.5 shows a schematic diagram of the HDI. With the increasing areal density of the HDD, the sizes of the components in the head and the bits in the disk must shrink. The spacing between the head and the disk also reduces from micrometers to nanometers [15, 16]. Nowadays, the initial head-disk spacing is $\sim$ 10–15 nm controlled by the air bearing design. The spacing is further reduced by energizing a joule heater in the head [17]. The heater generates a microscale protrusion on the head surface (the bulge in Figure 1.5) by thermal expansion to achieve a physical spacing of $\sim$ 1 nm between the protrusion surface and the disk surface, which is called the fly height. Therefore, the heater is also known as the thermal fly-height control (TFC). With the physical spacing reduced to $\sim$ 1 nm, data reading/writing can be performed using the read/write transducers (reader/writer) in the head. The heater actuation and the resultant fly height dynamics have been extensively investigated [18–22]. There is also a thermometer near the head surface, which is called the touchdown sensor (TDS) or embedded contact sensor (ECS). The thermometer is a metal wire that measures the head temperature [23–26]. It is typically used to detect the head-disk contact from the head cooling effect when the head protrusion approaches the disk or from the frictional heating induced by the head-disk contact [27, 28].

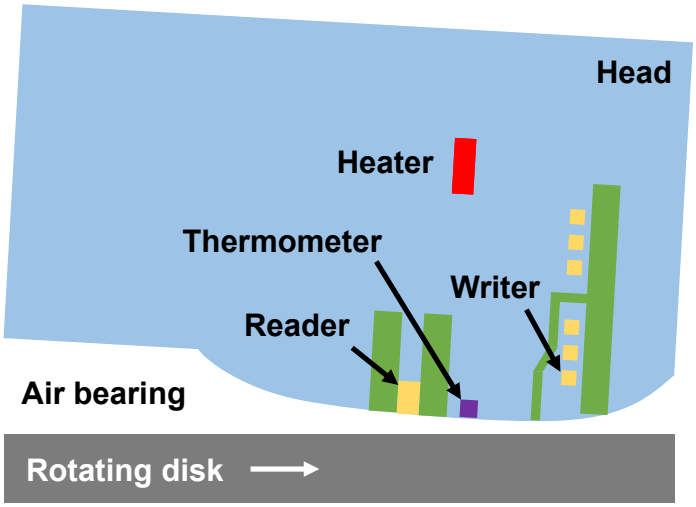

Figure 1.5: A schematic diagram of the head-disk interface (not to scale).

Head-media spacing (HMS), another commonly used term in the industry, differs from the fly height. The HMS is the distance between the bottom of the reader in the head and the top of the magnetic layer in the disk [29], while the fly height refers to the physical distance between the two bodies in the HDI. Thus, the HMS is the sum of the head carbon overcoat

thickness, the fly height, the lubricant thickness and the disk carbon overcoat thickness. It is noted that the reader performance can improve approximately by a factor of two when the HMS decreases by 0.3–0.5 nm [29]. Therefore, the HDD industry devotes much effort to the development of ultrathin protective films and further reduction of the fly height.

1.2 Heat-assisted magnetic recording (HAMR)

Conventional HDD technology, called perpendicular magnetic recording (PMR), has reached the superparamagnetic limit of ~ 1 Tb/in^2 [30]. If the magnetic bit size in the disk is further reduced to realize a higher areal density, the bits' magnetization can be randomly reversed by thermal fluctuations under room temperature without any external field, which is called superparamagnetism [31]. Then, the data can not be stored stably on the disk. If higher coercivity magnetic layers are used in the disk, the magnetic bits in the disk can be thermally stable, but data writing becomes more challenging. To address the dilemma between the high areal density and the data writing challenge, heat-assisted magnetic recording (HAMR) has been proposed [3–6].

The HAMR principle is shown in Figure 1.6 [4]. HAMR utilizes a high coercivity magnetic layer which can avoid superparamagnetism and store the data stably at room temperature. During the data writing operations, HAMR uses a laser to heat the disk to lower the magnetic layer's coercivity temporarily such that the data can be written on the disk using the head write field. The write temperature is usually in a narrow temperature range below the magnetic layer's Curie temperature [32]. Then, the disk cools down naturally (in nanoseconds) and the coercivity becomes high again to ensure stable data storage.

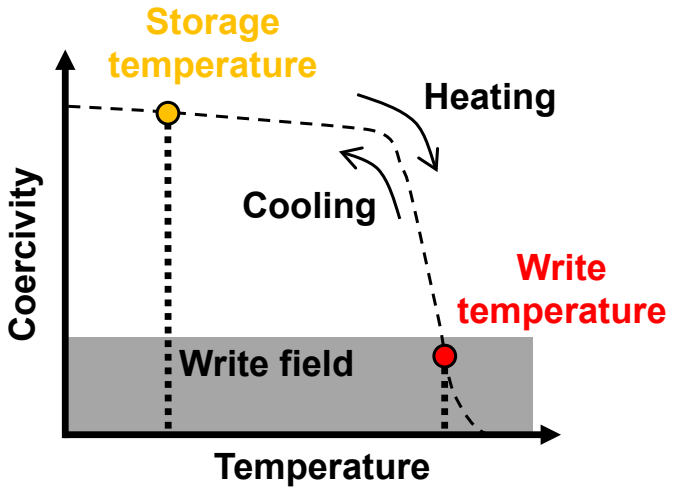

Figure 1.6: An illustration of HAMR principle. Inspired by Fig. 1 of Ref. [4].

Figure 1.7 shows a schematic diagram of a typical HAMR head-disk interface. Compared to conventional PMR technology, HAMR contains additional components such as a laser diode, a waveguide (WG), a near field transducer (NFT) in the recording head and a heat sink in the recording disk [6, 33]. As shown in Figure 1.7, a laser beam is launched from the laser diode and travels through the WG and the NFT (NFT omitted in Figure 1.7). The laser is finally focused on the recording disk to locally heat the disk to its Curie temperature (400–500 °C) with a spot size ∼ 25 nm [4, 34]. Thus, the coercivity of the magnetic layer in the disk is lowered and data writing can be performed. The head is also heated to 150–250 °C by the laser during this process [34]. Therefore, the HAMR head-disk interface is a system that combines nanoscale spacing (< 15 nm), high temperatures (head ∼ 150–250 °C, disk ∼ 400–500 °C), steep thermal gradient (∼ 10 K/nm), and a high-speed sliding condition (5–40 m/s) [4, 14]. The HDI performance directly determines the lifetime of the HAMR product [14, 29].

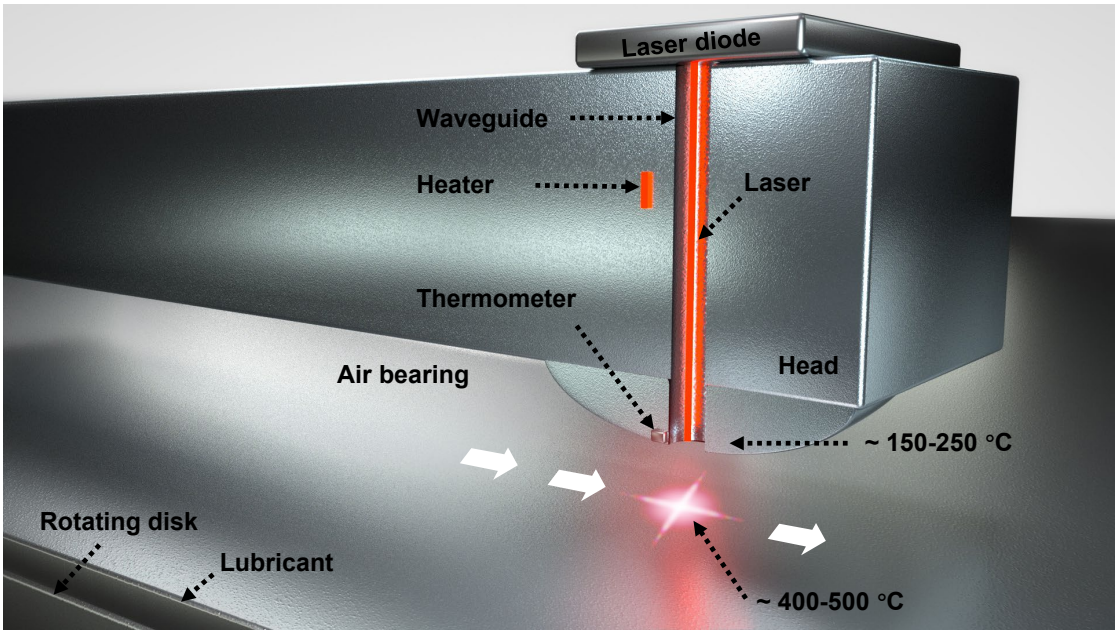

Figure 1.7: A schematic diagram of the HAMR head-disk interface (not to scale). The reader, writer and NFT are omitted.

The introduction of the laser brings several reliability issues to the head-disk interface [14, 29, 35]. First, the laser heats the head to 150–250 °C and heats the disk to 400–500 °C, which produces thermal transport across the head-disk interface. The laser heating may cause overheating issues at the NFT, and thus affects laser energy delivery and causes head failure [36, 37]. Therefore, understanding the thermal transport across the HDI is of great importance to the HAMR technology. In addition, the laser delivery proceeds with

energy loss [38], which leads to a localized angstrom-level laser-induced protrusion (LIP) and a fly height change (FHC) [34]. The LIP may cause material failure, leading to the degradation of the HDD performance [39]. Hence, the LIP and the FHC need to be considered and compensated in the spacing control [40]. During the laser exposure, material transfer also occurs due to the high level of thermal transport. The temperature of the hot spot on the disk is much higher than the lubricant evaporation/decomposition temperature [41–43], so the lubricant is evaporated/decomposed from the disk and then condenses on the cooler head surface. The material accumulation on the head surface, also known as smear, is a challenging reliability issue for HAMR [14, 36]. The smear can affect the head's flyability as well as the thermal transport and the NFT efficiency of laser delivery in the HAMR head-disk interface, which may finally lead to the device failure [36]. These reliability issues on thermal transport, thermal protrusion, and thermally-induced material transfer need to be investigated both for fundamental understanding and for practical applications such as HAMR or other microelectronics devices.

This dissertation focuses on HAMR, but there are other emerging technologies besides HAMR such as energy-assisted perpendicular magnetic recording (ePMR) and microwave-assisted magnetic recording (MAMR). To assist data writing, ePMR applies a bias current to the writer and generates an additional magnetic field, while MAMR uses a spin torque oscillator to induce ferromagnetic resonance in the media grains [44]. The spin torque oscillator in MAMR undergoes a high current density ($\sim 10^8$ A/cm^2) during writing, so MAMR also has the head overheating problem (> 200 °C) [45].

1.3 Objective of this dissertation

HAMR, as one of the most promising technologies to boost the areal density of hard disk drives over 1 Tb/in^2, is approaching commercialization. However, since the HAMR drive is still in the early stage as a product, there still remain some important reliability issues to be studied such as thermal transport, thermal protrusion, and thermally-induced material transfer, as described in Section 1.2. In this dissertation, experiments were performed to investigate these issues for fundamental understanding and for practical applications. The objectives of this dissertation are as follows:

- Provide a better understanding of the thermal transport across the head-disk interface under various conditions
- Measure the angstrom-level laser-induced protrusion and modulate the head protrusion shape by use of dual heaters for protrusion management
- Investigate the smear formation and the smear mitigation, and develop a head cleaning scheme for smear management
- Propose a thermal mapping technique and a scheme for lubricant thickness measurement, and give new insights into thermal measurements and thin film measurements

1.4 Organization and novel contributions of this dissertation

The organization and novel contributions of this dissertation are presented in this section. Chapter 1 introduces the basics of HDDs and HAMR, and describes several HAMR reliability issues that need to be addressed.

Chapter 2 presents thermal transport experiments across a closing gap between a recording head and a substrate. A nanoscale gap is realized between the two macroscopic surfaces using a custom-made experimental setup. The gap is further reduced to zero by energizing a heater in the recording head. Meanwhile, a thermometer in the head is used to measure its temperature when the head surface approaches the substrate. The experiments were performed under various conditions to investigate effects of substrate material, relative humidity and laser current on the thermal transport.

In Chapter 3, we performed flying touchdown experiments using a component-level HAMR test stage. First, we present a touchdown-based method to measure the angstrom-level laser-induced protrusion (LIP). The effect of laser heating on slider dynamics is also investigated and analyzed. Then, we performed experiments to demonstrate that the head protrusion shape can be modulated by use of dual heaters, and that the touchdown area can be controlled precisely.

In Chapter 4, smear formation and smear mitigation in HAMR are investigated experimentally. Effects of disk temperature and laser exposure time on the smear formation are studied, and the smear formation mechanism is revealed. Then, two smear mitigation strategies are presented. One is a mechanical approach where the smear can be mitigated due to frictional interactions induced by the heaters in the head, and the other is a thermal approach by reversing the direction of temperature difference in the head-disk interface.

Subsequently, Chapter 5 presents a versatile thermal mapping technique based on a phase change material $Ge_2Sb_2Te_5$. By use of the change of its properties before/after the phase transition, the technique can spatially resolve devices' surface temperature from nanoscale to microscale with negligible temperature interference and minimal calibration, which is demonstrated using a recording head.

Chapter 6 presents a near-field thermal transport based scheme for lubricant thickness measurement. The effect of the lubricant on the near-field thermal transport between the head and the disk is studied. Then, we propose an in-situ scheme to measure the lubricant thickness, and report the first quantitative measurements of sub-angstrom depletion and reflow dynamics of the nanometer-thick PFPE lubricant on the disk when exposed to high-temperature HAMR-type operations.

Chapter 7 concludes this dissertation and presents potential future work.

Chapter 2

Thermal transport across a closing gap

2.1 Introduction

Nanoscale thermal transport between two bodies at different temperatures is a broadly studied topic [46–58]. As the microelectronics industry pushes the physical size of components in devices down to nanoscale dimensions, the nanoscale thermal transport leads to mass transfer and overheating problems that affect the efficiency of the devices and introduce reliability issues [4, 36, 37, 59]. Therefore, understanding the nanoscale thermal transport and its tunability is of fundamental significance and holds high economic value for various industrial applications such as hard disk drives [4, 5, 33], nanolithography [60, 61] and near-field thermophotovoltaics [62–64].

The thermal transport between the two separated macroscopic bodies strongly depends on the size of the air gap between them. For a larger gap ($\sim \mu$m), the thermal transport includes air conduction and radiation that follows the Stefan-Boltzmann law. At a smaller gap ($\sim \mu$m to $\sim$ few nm), the radiative thermal transport between the macroscopic bodies increases strongly, as a result of evanescent electromagnetic fields [50, 55, 65–67]. Further, for a narrower gap ($< \sim$ few nm), the thermal transport sharply increases and is dominated by additional mechanisms such as phonon heat conduction [68, 69]. Recent experimental observations, along with the theoretical framework of fluctuational electrodynamics, have shown that the thermal transport across nanoscale gaps exceeds the Planck's blackbody limit by several orders of magnitude [50, 55, 66, 67, 70].

In this chapter, static touchdown experiments were conducted under various conditions using a custom-made setup to study the thermal transport across a closing gap. Section 2.2 introduces the experimental setup for the static touchdown. Section 2.3 presents experimental results and discussion of the results. Specifically, effects of substrate material, relative humidity and laser current are investigated. Section 2.4 concludes this chapter.

This work was completed jointly with Siddhesh Sakhalkar, Amin Ghafari and Yuan Ma.

Siddhesh Sakhalkar performed simulations to predict the head/disk temperature and the head-disk spacing during the static touchdown. Amin Ghafari computed the thermal coefficient of phonon heat conduction. Yuan Ma built the experimental setup. I performed the static touchdown experiments under various conditions and measured the head temperature rise versus the heater power.

2.2 Experimental setup: static touchdown

In the static touchdown experiments, we study the nanoscale thermal transport across a closing gap between a recording head and a substrate in ambient conditions. The head contains a well-understood embedded microscale heater [71] and a metal wire of $\sim$ 100 nm wide, as shown in Figure 2.1. Traditionally, the heater is used to adjust the spacing between the recording head and a rotating disk. The metal wire, also known as the touchdown sensor (TDS) or embedded contact sensor (ECS), is located near the read/write transducers and is surrounded by metal shields. It is typically used to detect head-disk contact [27]. In this chapter, the metal wire functions as a resistance based thermometer that has a constant temperature coefficient of resistance (TCR). In the experiments, the resistance change of the

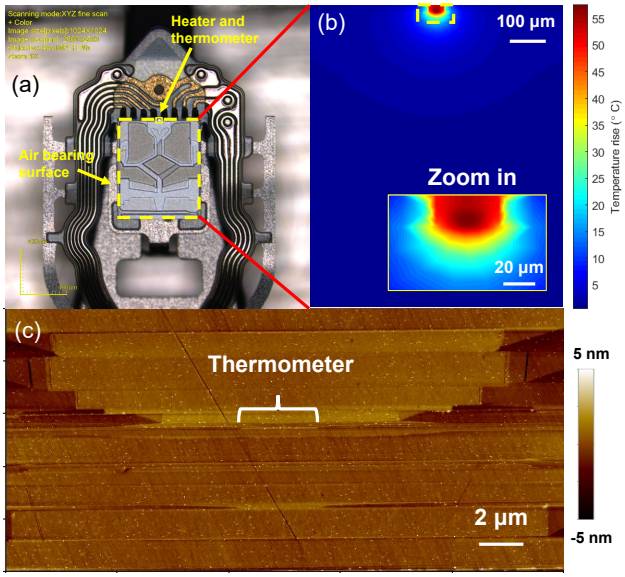

Figure 2.1: (a) An optical image of a recording head showing its ABS. (b) The simulated temperature field when the heater power is 80 mW while the head-substrate gap is around 2 nm. (c) An atomic force microscopy (AFM) image of the head surface showing the thermometer.

thermometer was used to measure the temperature rise due to the heater by:

$$R(T) = R(T_0)(1 + \alpha(T - T_0)), \tag{2.1}$$

where $R(T)$ and $R(T_0)$ are the resistances of the thermometer at any temperature T and room temperature T_0 and α is the TCR. Figures 2.1(b-c) show that the temperature field near the thermometer is uniform since the heater has a microscale heated area. Thus, the thermometer can accurately measure the temperature of the head surface. Therefore, this recording head provides an excellent platform for conducting such experiments of the nanoscale thermal transport between two bodies.

Figure 2.2 shows the calibration details of the thermometer. The thermometer has a TCR of 0.003/K, which was determined using a 4-probe measurement, as shown in Figure 2.2(a). When measuring the head temperature, the thermometer was biased using a small enough DC voltage for its overall self-heating to be ignored (~ 0.1 °C rise according to Figure 2.2(b)). The resolution of the thermometer is ~ 0.1 °C, which is estimated from the resolution of resistance measurement $\sim 0.02\ \Omega$.

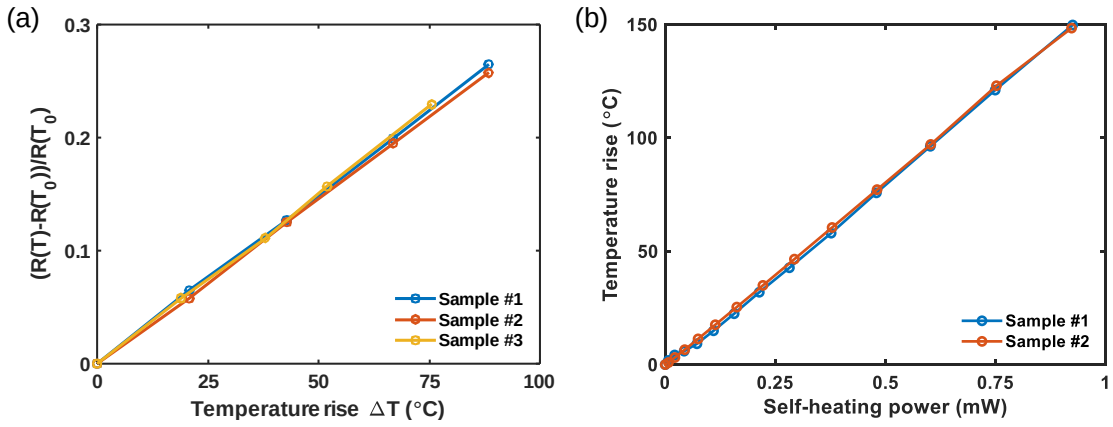

Figure 2.2: (a) Calibration of the thermometer showing that its TCR is 0.003/K. (b) The temperature rise versus the self-heating power of the thermometer (slope: 162 °C/mW).

The experimental setup for static touchdown is shown in Figure 2.3. The ABS of the head was loaded onto a substrate. The substrate was fixed on a metal heat sink, so the bottom surface of the substrate was kept at room temperature. Then the heater in the head was energized and a microscale protrusion formed on the head surface due to thermal expansion. Thus, the gap between the head surface and the substrate decreased with the heater power until they were into contact with each other. Meanwhile, the thermometer located at the center of the protrusion surface measured the protrusion's temperature as it approached the substrate. The thermal transport between the head protrusion and the substrate is dominated by air conduction and phonon heat conduction, where radiation is

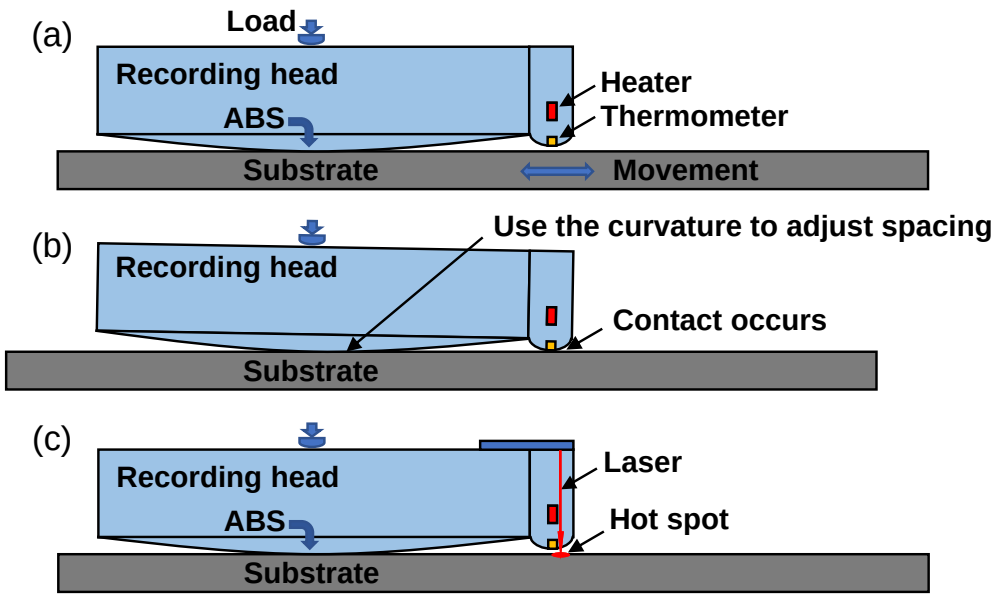

Figure 2.3: A schematic diagram of the experimental setup (not to scale). Several cases: (a) a gap between the head and the substrate; (b) direct contact between the head and the substrate; (c) with presence of the laser.

negligible [57]. Figures 2.3(a-b) show that the initial gap between the two bodies can be adjusted by movement of the substrate. The curvature of the ABS was used to adjust the initial gap between the thermometer and the substrate. For example, when the substrate moves left, the friction between the crowned ABS and the substrate forces the head to tilt and hence the gap size is decreased. Even direct contact can be realized as an initial condition as shown in Figure 2.3(b). Figure 2.3(c) shows the case with a built-in laser using a HAMR head. The heater, the thermometer and the laser were controlled by a data acquisition (DAQ) system that consisted of two synchronized Multifunction I/O Devices manufactured by National Instruments (NI): PCI-6115 and USB-6211. They have multiple analog output channels and analog input channels with high sampling rate ($\sim$ MHz).

The experimental setup is in an environment with relative humidity (RH) control as shown in Figure 2.4(a). The entire setup was put into a sealed chamber with a dry air inlet and a vacuum pump, which were used to achieve low humidity conditions. For higher RH, different types of saturated salt solutions (NaCl, KNO_3, K_2SO_4, etc.) or pure water were put into the chamber to keep the relative humidity at different levels [72]. Figure 2.4(b) shows the measured RH data in two cases, and their fittings using the exponential function $\mathrm{RH} = A - Be^{-\frac{t}{\tau}}$, where A, B, τ are the fitting parameters. The experiments were conducted after the humidity reached equilibrium in the chamber ($\sim$ 12 h according to Figure 2.4(b)). It is noted that the pressure inside the chamber was always 1 atm.

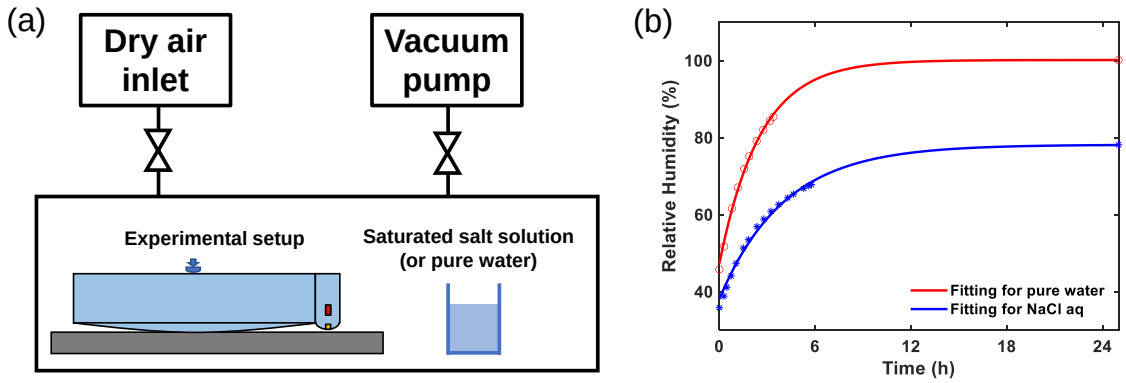

Figure 2.4: (a) A diagram showing how the relative humidity is controlled. (b) The relative humidity in the chamber over time with pure water or NaCl aq.

2.3 Results and discussion

2.3.1 Effect of substrate material

The effect of substrate material on the thermal transport is investigated in this subsection. Three substrates with various thermal properties (silicon/GaAs/glass wafers) are chosen instead of the multilayer disks that are broadly used in the HDD industry. Figure 2.5 shows the measured temperature rise as a function of the heater power in the cases of free heating, closing gaps and contact on silicon wafer and GaAs wafer. Free heating is the case where the initial gap between the head and the substrate is larger than the protrusion that 200 mW

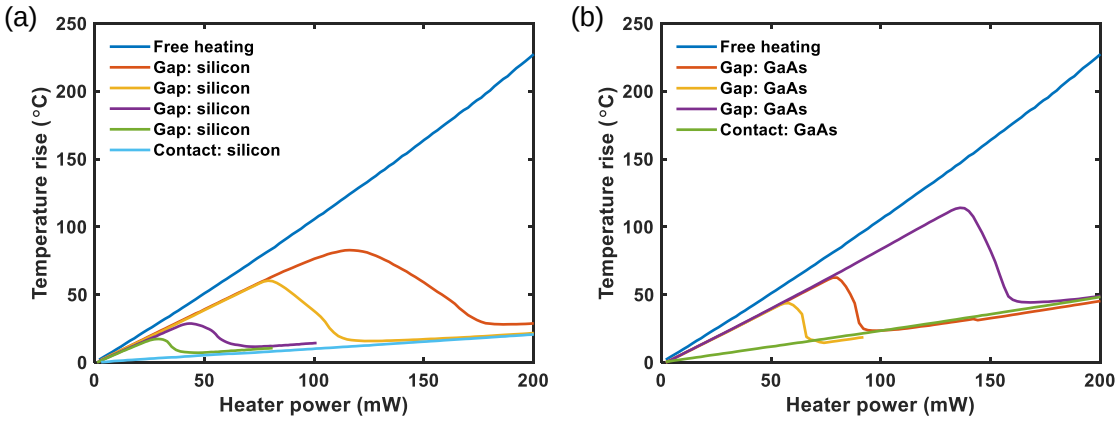

Figure 2.5: The temperature rise as a function of the heater power in the cases of free heating, closing gaps and contact on (a) silicon wafer and (b) GaAs wafer.

heater power can produce, so the gap is not closed and thus no cooling due to near-field enhanced thermal transport occurs, which makes the curve always linear. Contact case is as shown in Figure 2.3(b) with the initial gap being zero, so a smaller heating slope appears due to heat conduction through contact (contact heat conduction). The curves between the free heating case and the contact case correspond to closing gaps but with different sizes. With a larger initial gap, more heater power is required to close the gap, so the local maximum/minimum of the curves both occur at larger heater powers. Figure 2.5 demonstrates that the initial gap can be controlled using the static touchdown setup.

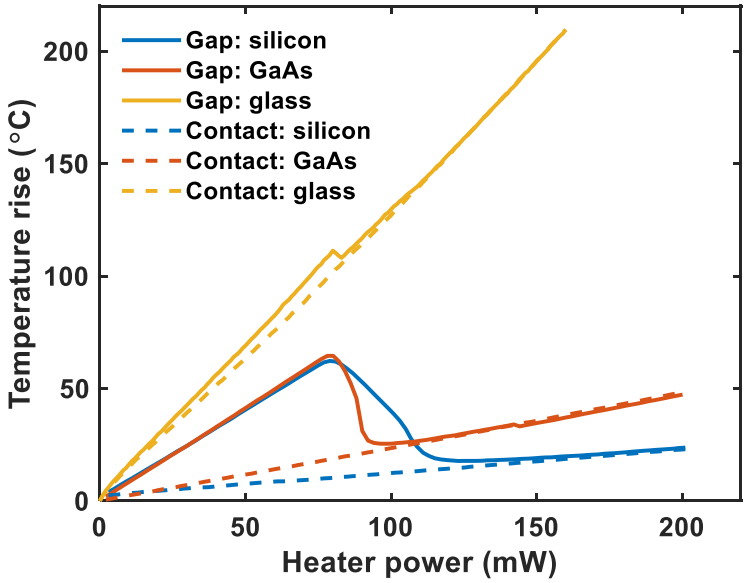

Figure 2.6: The temperature rise as a function of the heater power in the case of a closing gap or direct contact on silicon/GaAs/glass wafers under the condition of indoor humidity around 35%.

Figure 2.6 shows the measured temperature rise as a function of the heater power using the three substrates (silicon/GaAs/glass wafers, surface roughness $S_q \sim 0.1$ nm). The solid lines present the results of cases for which the initial gap size is around 21.3 nm (from simulation as shown in Figure 2.7) while the dashed lines show the cases with direct contact as the initial condition. The measured temperatures first increase linearly with the heater power where the air conduction across the gap dominates to almost 2 nm, which is called free heating stage. With the decrease of the gap, enhanced phonon heat conduction dominates and causes a drop in the temperature (cooling stage). Finally, the head protrusion makes contact with the substrate and a much smaller heating slope is observed due to contact heat conduction (contact stage). Figure 2.7 shows that the enhanced phonon heat conduction begins to take effect when the gap is within around 2 nm, which is close to the prediction of another approach using an atomic formalism [68]. The detailed description of the simulation

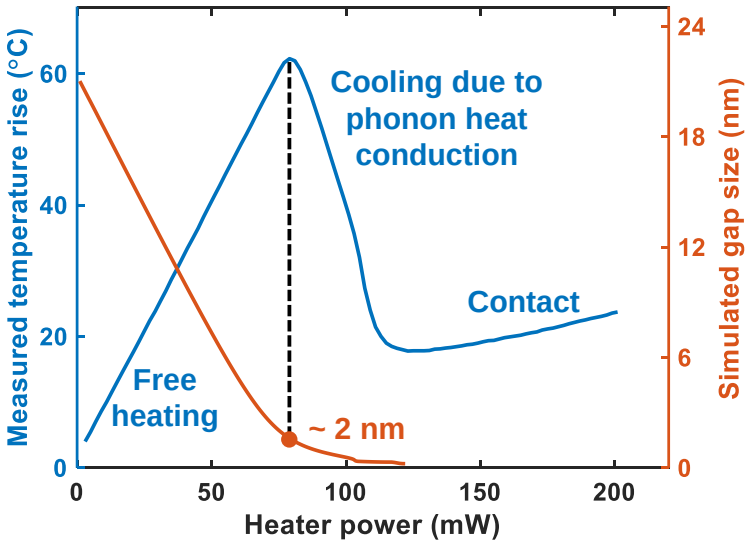

Figure 2.7: The measured temperature rise and the simulated gap size versus the heater power in the case of silicon wafer.

model used to determine the temperature field in Figure 2.1(b) and the gap in Figure 2.7 can be found in Ref. [57].

Comparing the cases of 21.3 nm initial gap (solid lines) and the cases of initial direct contact (dashed lines), we see that the contact stages of the curves with 21.3 nm gap overlap with the dashed lines. Comparing among the three substrate materials, we find that the material thermal conductivity plays an important role. The thermal conductivities of the substrates are listed in Table 2.1. During the free heating stage of each curve, the glass curve has the largest heating slope because the glass has the smallest thermal conductivity (1.3 W/(m·K)) and hence the glass substrate undergoes a higher temperature rise compared to the silicon and the GaAs substrates (148 W/(m·K) and 56 W/(m·K)). Figure 2.8 shows the simulation results of the head/substrate temperature rise, along with the experimental results. It is found that the glass substrate undergoes a temperature rise $\sim$ 120 °C before contact occurs, while the silicon substrate only has an increase $\sim$ 20 °C, which is due to its

Substrate	Thermal conductivity (W/(m·K))
Silicon	148
GaAs	56
Glass	1.3

Table 2.1: Thermal conductivity of the substrates.

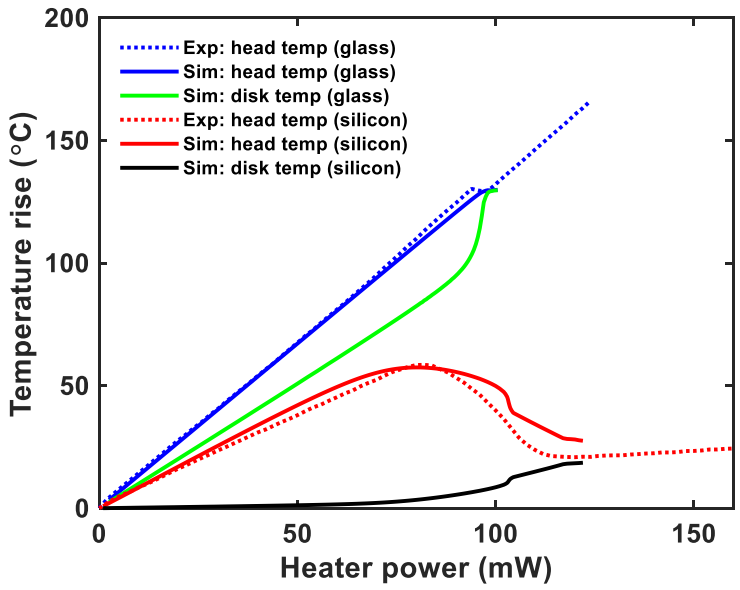

Figure 2.8: The simulation results of temperatures at both the thermometer and the top surface of the substrate (disk).

high thermal conductivity. In Figure 2.6, the GaAs also shows a similar free heating slope to the silicon because the air conduction dominates the free heating stage and the GaAs/silicon both have a thermal conductivity much larger than air ($\sim$ 0.02 W/(m·K)).

After contact occurs, the heating slope is totally determined by the thermal conductivity of the substrate. When using a better thermal conductor such as silicon, the heating slope becomes smaller because the heat conduction becomes stronger through contact. Therefore, the temperature drop (cooling) between the free heating stage and the contact stage is essentially dependent on the material thermal conductivity. The steepness of the drop depends on the van der Waals (vdW) force and the thermal coefficient of the phonon heat conduction across the gap. The vdW force between the head protrusion and the substrate causes a steeper drop in the curve of the temperature rise versus the heater power, as demonstrated in Ref. [57]. The thermal coefficient of the phonon heat conduction affects the total HDI thermal conductance and thus affects the heater power required to produce the last 2 nm of the gap until contact.

Moreover, the thermal transport experiments were also conducted in vacuum to exclude the air conduction. Figure 2.9 plots the results of static touchdown on silicon wafer in air and in vacuum ($< 10^{-4}$ Torr). Due to the absence of the air conduction, the vacuum curve has a larger heating slope in the free heating stage and an earlier local maximum ($\sim$ 2 nm gap from Figure 2.7) than the air curve, which makes sense because the same amount of the heater power can produce a higher temperature and a larger thermal protrusion when the cooling across the interface becomes less. Finally, the two cases present the same heating

slope in the contact stage where the contact heat conduction dominates regardless of the air conduction.

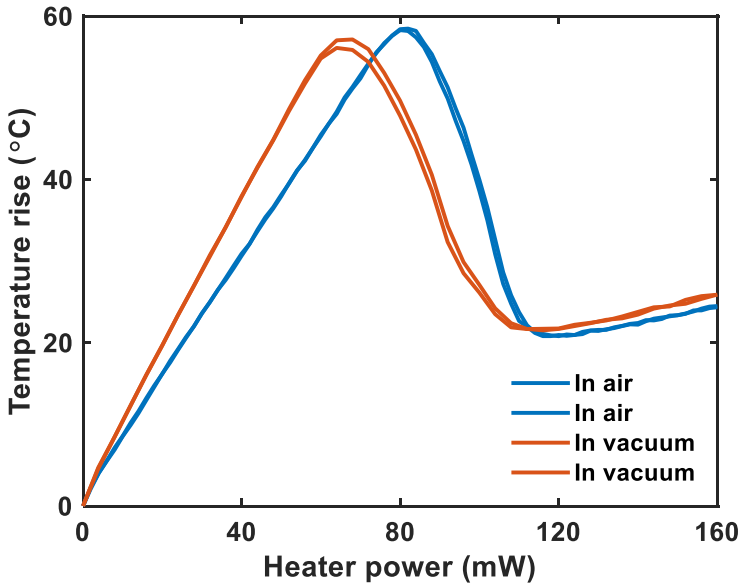

Figure 2.9: The results of static touchdown on silicon wafer in air/vacuum.

2.3.2 Effect of relative humidity

In this subsection, the effect of relative humidity (RH) is investigated for further understanding the thermal transport across the closing air gap. Figure 2.10 shows the experimental results of the temperature rise as a function of the heater power under different RH conditions using a silicon substrate. The case of direct contact on silicon which is independent of humidity is also added in Figure 2.10 for comparison. The curves show no change in the measurement when the RH $\leq 75\%$. When the RH $> 75\%$, the curves of the temperature rise versus the heater power show a smaller temperature rise and a more gradual temperature drop. The last linear stages of all curves, namely the contact stages, still overlap with the black dashed line, which was measured in the case of direct contact as the initial condition. Thus, we have shown that the nanoscale thermal transport depends on the ambient humidity for RH $> 75\%$.

Figure 2.10 shows that the nanoscale thermal transport is enhanced when the humidity is beyond 75%. One of the potential explanations is that a thin water layer forms under high RH conditions. The water layer reduces the gap between the head protrusion and the substrate, and absorbs a portion of heat. A previous study shows that the thickness of the absorbed water layer remains smaller than 1 nm when the RH is low and increases to 3 nm under the high RH conditions [73]. This trend matches the results in Figure 2.10 in that the

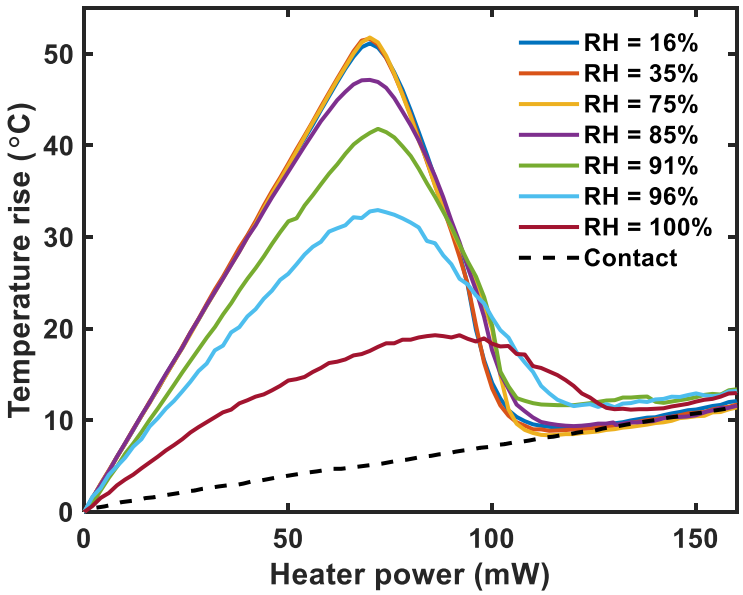

Figure 2.10: The temperature rise as a function of the heater power under different RH conditions with the substrate of silicon.

water layer takes effect when its thickness is comparable to the gap, namely under high RH conditions.

To further investigate the reason why the high RH affects the thermal transport, we need to pay attention to the transient data. Figure 2.11(a) shows the steady result on silicon wafer and Figure 2.11(b-d) show the transient data at three heater powers in the three stages. The data points in the steady curve are the average of the corresponding transient data. At the heater power of 63 mW, the curve in Figure 2.11(a) is in the free heating stage, so the temperature signal in Figure 2.11(b) ramps up and falls when turning on/off the heater. When the heater power is 101 mW in the cooling stage, two peaks are observed in Figure 2.11(c), one when the heater is turned on and the other when it is turned off, which can be explained by the proposition that the dynamic response of heater protrusion is faster than the heat dissipation. For example, the head protrusion can be temporarily larger than expected when the heater is energized, then more cooling caused by smaller gap (or contact) decreases the head temperature until equilibrium is reached. With a higher heater power 133 mW in the contact stage, Figure 2.11(d) shows that the observed peaks become steeper due to the contact heat conduction and the steady temperature decreases in accordance with Figure 2.11(a).

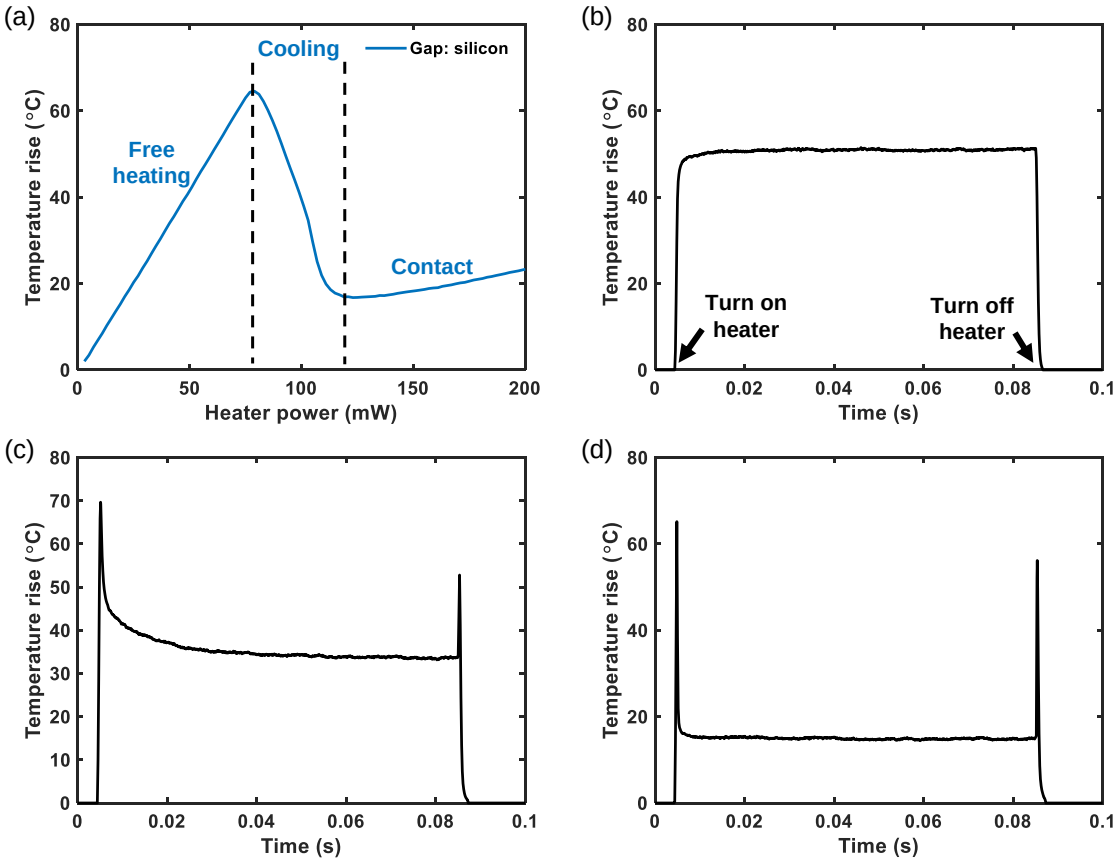

Figure 2.11: (a) The static touchdown result on silicon wafer. (b-d) The transient temperature rise at the heater power of 63 mW, 101 mW and 133 mW, respectively.

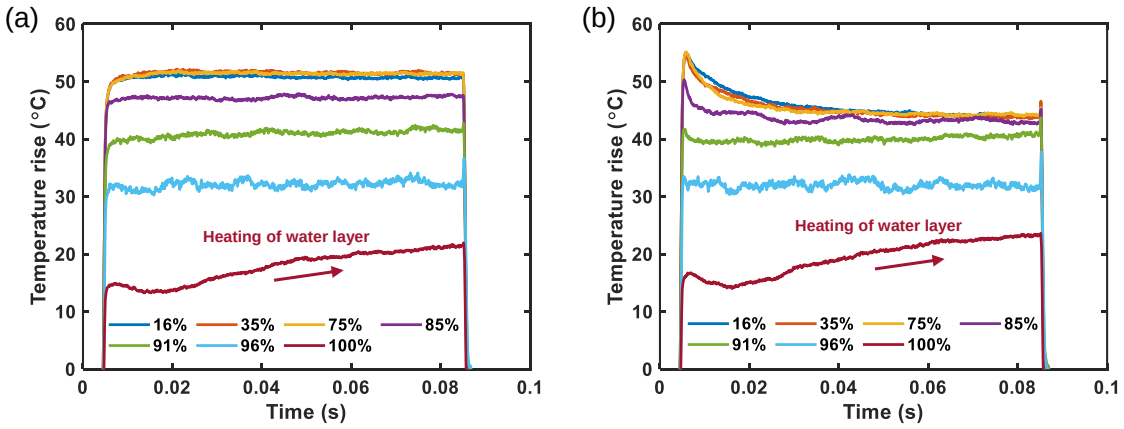

Figure 2.12: The transient temperature rise for the heater power of (a) 70 mW (b) 80 mW under different RH conditions.

Returning to the RH effect, Figure 2.12 shows the transient measurement of the temperature rise when the heater power is 70 mW or 80 mW. At the heater power of 70 mW, the gap size is a little larger than 2 nm according to Figure 2.7, but the transient curve of 100% RH shows that the water layer fills the gap and that the heater heats the layer continuously, resulting in the lower temperature at the thermometer, which is not observed for all other curves. When the heater power is 80 mW, the low RH curves in Figure 2.12(b) show an increase and then a gradual drop, similar to Figure 2.11(c). However, the 100% RH curve does not show such a dynamic evolution, indicating that the head protrusion is already into contact with some layer, which is assumed to be a thin water layer absorbed from the high RH environment. Therefore, the interaction between the water layer and the gap accounts for the smaller temperature rise when the RH increases. The more gradual temperature drop in Figure 2.10 can also be explained by the water layer as water has a large heat capacity (4.2×10^3 J/(kg·°C)) and acts as a buffer.

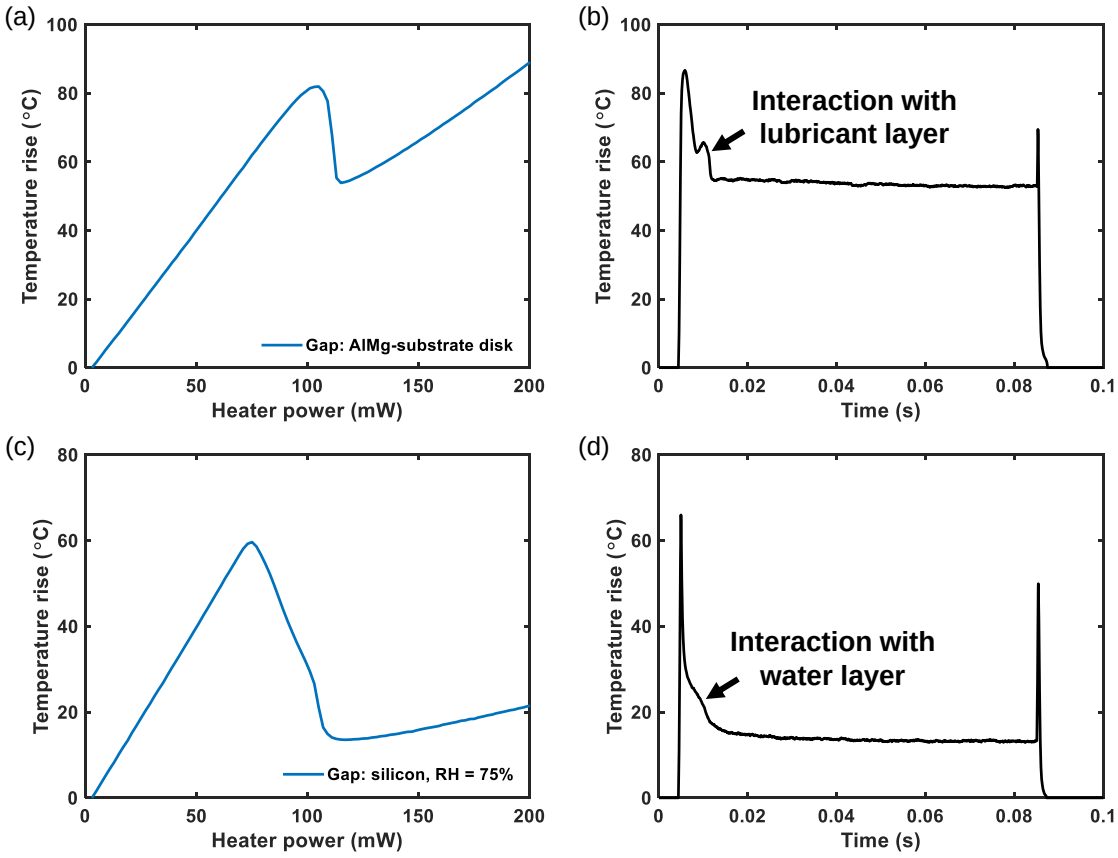

Figure 2.13: (a) The static touchdown result on AlMg-substrate disk and (b) its transient data at the heater power of 113 mW. (c) The static touchdown result on silicon under 75% RH and (b) its transient data at the heater power of 109 mW.

Figure 2.13 presents another evidence of the water layer's existence. During the cooling stage of the AlMg-substrate disk case in Figure 2.13(a), the transient data at the heater power of 113 mW shows a bump in Figure 2.13(b), which is due to the head protrusion's interaction with the lubricant layer. The head protrusion comes into contact with the disk surface and the lubricant's low thermal conductivity (0.1 W/(m·K) [74]) temporarily rises its temperature. The same phenomenon also appears in the silicon case under 75% RH as shown in Figure 2.13(c-d), which further verifies the explanations based on the water layer.

2.3.3 Effect of laser current

To study the effect of the laser current on the thermal transport across the closing gap, HAMR heads with a built-in laser are used. It is noted that this type of HAMR head has a laser spot size $\sim$ 300 nm and no near-field transducer (NFT). Figure 2.14 shows the plots of the thermometer temperature rise versus the heater power during static touchdown on the silicon wafer and the AlMg-substrate disk, with the laser current varying from 0 to 50 mA. Comparing between the two cases of silicon wafer/AlMg-substrate disk, they show a similar heating slope in the free heating stage because the gap is over several nanometers and air conduction dominates the thermal transport, which is also observed in the silicon/GaAs cases in Figure 2.6. In the contact stage, the silicon wafer case shows a much smaller heating slope than that in the AlMg-substrate disk case because silicon is a better thermal conductor. First, silicon (148 W/(m·K)) has a higher thermal conductivity than AlMg (117 W/(m·K)) [75]. Also, the multilayer structure of the disk makes the disk a much poorer thermal conductor. The disk has a lubricant layer (0.1 W/(m·K)), carbon overcoat layer (1 W/(m·K)) and a magnetic layer on the AlMg substrate [36, 74]. These layers and the interface thermal conductances between them make the overall effective thermal conductivity

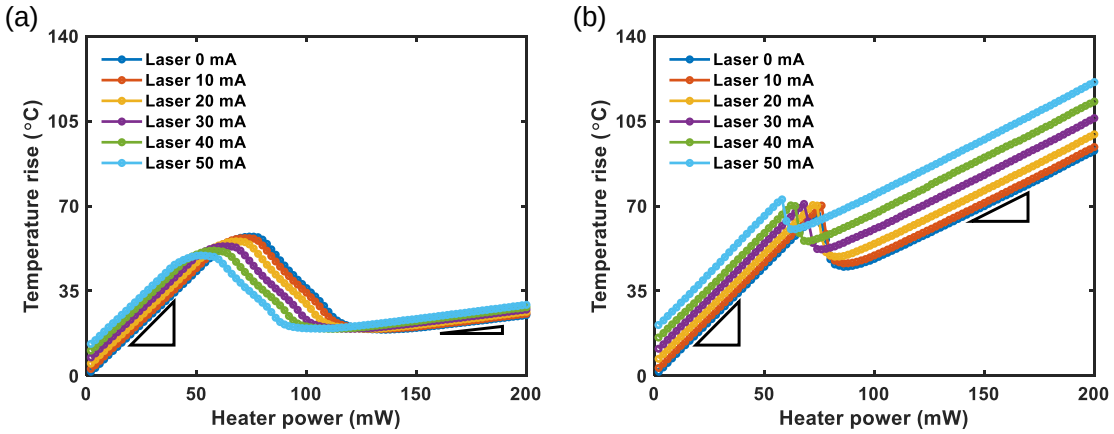

Figure 2.14: The temperature rise as a function of the heater power and varying laser currents in two cases of (a) silicon wafer and (b) AlMg-substrate disk.

of the disk smaller than 117 W/(m·K), leading to the larger heating slope during contact in the static touchdown. During the cooling stage, the AlMg-substrate disk presents a smaller temperature drop than the silicon wafer case, which is caused by the total HDI thermal conductance (3×10^7 W/(m^2·K) in the AlMg-substrate disk case versus 5×10^7 W/(m^2·K) in the silicon case due to roughness) [57]. With a lower HDI thermal conductance, a smaller heater power increase is needed to fill the last $\sim$ 2 nm of the gap until contact. Thus, the cooling stage in the AlMg-substrate disk is short in terms of the heater power.

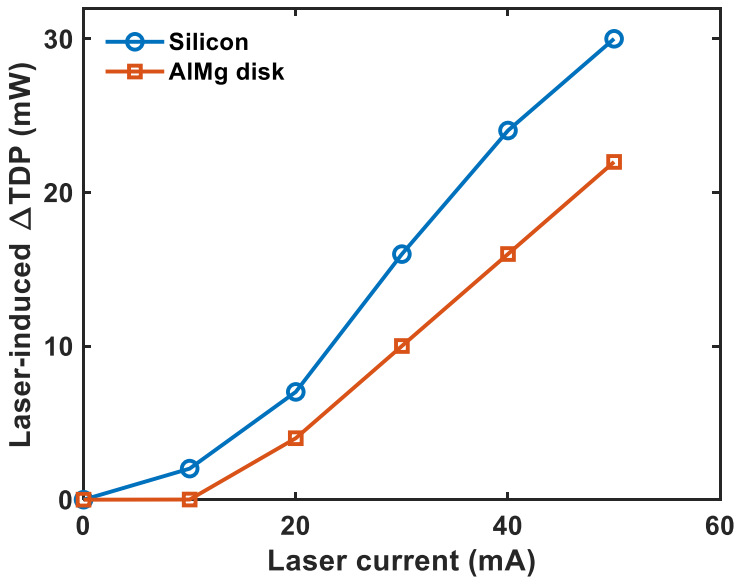

Figure 2.15: The laser-induced touchdown power change (ΔTDP).

As the laser current increases, both cases in Figure 2.14 show that the two critical heater powers, corresponding to the local maximum/minimum of the temperature rise, decrease due to the laser. The reason for this change is that the laser heating causes extra protrusions on the head surface and the disk surface, which reduce the air gap. Hence, smaller heater powers are needed for the two critical points. Additionally, the laser diode in this HAMR head has a threshold $I_{\text{th}} \sim 13$ mA, which means that there is no laser coming out in the case of 10 mA laser current. Therefore, the change of the critical heater powers in the case of 10 mA indicates that the laser-induced protrusion does form on the head surface. Figure 2.15 plots the laser-induced touchdown power change (ΔTDP) in the two cases of silicon wafer and AlMg-substrate disk. Here, the touchdown power refers to the heater power at the local minimum of the temperature rise, which is exactly between the cooling stage and the contact stage. The ΔTDP indicates the gap change due to the laser-induced protrusions. When the laser current is low (< 13 mA), no laser comes out from the head, so there is only an extra laser-induced protrusion on the head surface and the ΔTDP accordingly rises slowly versus the laser current. When the laser current goes beyond 13 mA, another laser-induced

protrusion also forms on the silicon surface or disk surface, and as a result, the ΔTDP rises linearly with a larger slope.

The thermometer temperature rise in Figure 2.14 is due to both the heater's joule heating and the laser heating. This rise grows linearly with the heater power in the free heating stage and in the contact stage. Thus, the laser heating effect can be obtained by subtracting the laser-off curve from the laser-on curves, which is called laser-induced temperature rise and is plotted in Figure 2.16. The laser-induced temperature rise is as small as 1–2 °C in the case of 10 mA laser current (below I_{th}) due to the laser's joule heat dissipation inside the head. Also, the two stages in the silicon case have smaller laser-induced temperature rises than the AlMg-substrate case due to the silicon's high thermal conductivity as discussed in Subsection 2.3.1.

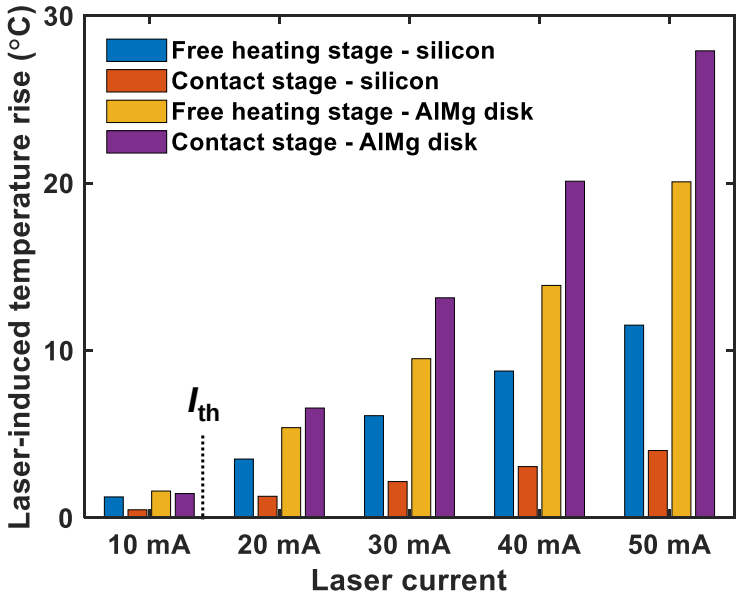

Figure 2.16: The laser-induced temperature rise in the free heating/contact stages.

Specifically, in the case of the silicon, the laser heating effect in the contact stage (red bars) is always ∼ 65% smaller than that in the free heating stage (blue bars), which is due to the contact heat conduction since silicon is a good thermal conductor and dissipates the heat effectively. However, the AlMg-substrate disk displays an opposite result with the presence of the laser. In the cases of 20 mA–50 mA laser currents, the laser heating effect in the contact stage (purple bars) becomes ∼ 40% larger than that in the free heating stage (yellow bars), which indicates that a hot spot forms on the disk due to the laser and in turn heats the head (back-heating [25]) through contact. Under such circumstance, the disk surface is hotter than the head, and hence no longer cools the head when they come into contact with each other. Furthermore, in the case of 10 mA laser current (below I_{th}) without laser

output, the laser heating effect in the contact stage (purple bar) is only a little smaller than that in the free heating stage (yellow bar) because of less contact heat conduction from the disk (compared to silicon) and the absence of back-heating. Therefore, the back-heating effect from the hot spot on the disk is directly observed on the AlMg-substrate disk using the static touchdown experiments.

It is noted that the static touchdown experiments differ from the actual HAMR drives in that the disk is not rotating and the air cooling is excluded. In the actual HAMR case with the rotating disk as shown in Figure 2.17, the thermal transport becomes more complicated because the air cooling and frictional heating are involved as compared to the non-rotating case (static touchdown results in Figure 2.14). The heater power change of the critical points ΔTDP as shown in Figure 2.15 is dependent on the ABS design because the introduction of the laser-induced protrusion is likely to change the ABS pressure distribution and the spacing under the flying condition. More investigations are needed to fully understand the thermal transport in the actual HAMR case with the rotating disk.

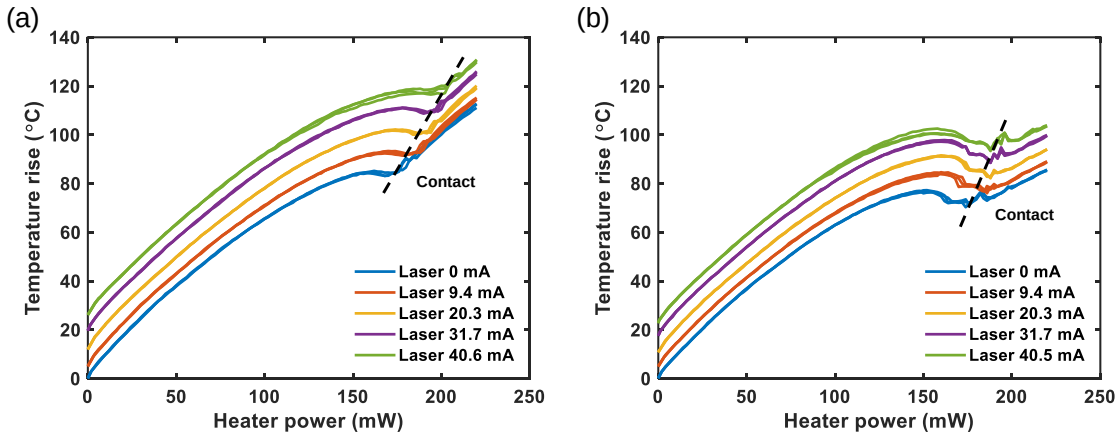

Figure 2.17: The temperature rise in the flying cases of a rotating (a) glass-substrate disk and (b) AlMg-substrate disk.

2.4 Conclusion

We performed static touchdown experiments under various conditions to study the thermal transport across a closing gap between the recording head and the non-rotating substrate. Using the custom-made experimental setup, a nanoscale air gap can be realized between the head and the substrate. The joule heater in the head was energized to generate a protrusion to reduce the gap until contact occurred. The temperature rise of the thermometer that is positioned near the head surface was measured along with the heater power. Particularly, effects of substrate material, relative humidity and laser current were investigated.

The thermometer temperature rise versus the heater power undergoes three stages: free heating, cooling and contact. The heating slopes in the free heating stage and contact stage depend on the thermal conductivity of the substrate material. The thermal transport across the gap becomes stronger when the substrate material has a larger thermal conductivity. During the cooling stage, an enhanced thermal transport due to phonon heat conduction is observed for the gap $< \sim 2$ nm. The steepness of the temperature drop depends on the vdW force and the thermal coefficient of the phonon heat conduction across the gap.

It is also discovered that the thermal transport becomes stronger when the RH is higher than 75%, along with a more gradual temperature drop in the cooling stage. A thin water layer is assumed to form under high RH conditions. The interaction between the water layer and the gap accounts for the stronger thermal transport. The more gradual temperature drop can also be explained since the water layer has a large heat capacity and can act as a buffer.

With the presence of the laser, the laser-induced protrusions form on the head surface and the disk surface, which contributes to the gap reduction and the ΔTDP. The laser also provides extra heating to the head, and the laser-induced temperature rise is separated from the experimental results. Besides the laser's joule heat dissipation inside the head, a back-heating effect from the hot spot on the disk can be directly observed in the case of the AlMg-substrate disk, while the silicon case shows no back-heating or less back-heating.

This chapter includes work published in *Applied Physics Letters* in 2020 (reproduced from [76], with the permission of AIP Publishing) and work presented at *ISPS-2019* [77] and *ISPS-2021* [78] (with the permission from ASME).

Chapter 3

Thermal protrusions in HAMR

3.1 Introduction

HAMR operations utilize a laser that travels through a waveguide (WG) and a near field transducer (NFT) and shines on the rotating disk to locally produce a nanoscale hot spot and lower the coercivity of the magnetic layer, as shown in Section 1.2. However, the laser delivery involves energy loss as shown in Figure 3.1 [38]. The laser diode has an efficiency of around 50%, and the WG-NFT interface undergoes multiple coupling losses [33, 79, 80], so only 0.5% of the input energy arrives at the disk to assist the HAMR writing.

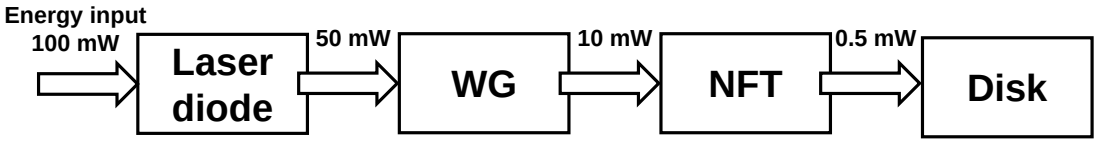

Figure 3.1: Energy loss during the laser delivery. Inspired by Fig. 3 of Ref. [38].

The energy loss at the laser diode heats the whole body of the recording head, leading to a crown/camber change and a broad fly height change (FHC) [34]. The rest of the energy that passes through the waveguide is partially absorbed by the head carbon overcoat, forming an extra localized angstrom-level protrusion, which is called laser-induced protrusion (LIP), as shown in Figure 3.2. The LIP forms in the short term ($\sim \mu$s) and the FHC happens in the longer term ($\sim$ ms) due to the crown/camber change. They need to be considered in the HDI spacing control and compensated during flying in the HAMR conditions [40]. The LIP may also cause material failure, leading to the degradation of the HDD performance [39].

In the previous studies, HAMR reliability issues such as thermal transport and material transfer were broadly investigated [26, 57, 58, 81–83]. Only a few studies focused on the LIP at the head surface. An atomic force microscopy (AFM) technique was used by Schreck *et al.* to measure the NFT protrusion in the static condition and the result was combined with

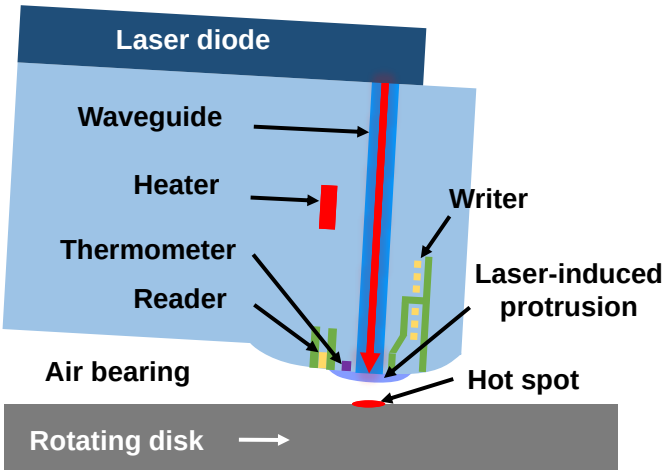

Figure 3.2: A schematic diagram (not to scale) showing the laser-induced protrusion (LIP) in the HAMR head-disk interface.

modelling to extend to the flying condition [34, 84]. A burnish method was utilized by Zhang *et al.* to characterize the LIP through contact with the rotating disk and AFM topography scans [85]. Xiong *et al.* came up with a timescale-based burst writing method to evaluate the NFT protrusion and the spacing in HAMR [86]. The LIP has hitherto been measured based on burnishing or readback signal. In this chapter, a touchdown-based method is proposed to measure the LIP.

In addition, HAMR operations may involve two heaters in the head to realize different and independent fly heights at the read and write transducers, respectively [87, 88]. By use of the dual heaters, a larger fly height reduction at the transducers can be achieved, and the heater actuation efficiency (ratio of fly height reduction to the maximum thermal protrusion) can be improved [18, 89–93].

In this chapter, flying touchdown experiments were performed to evaluate the LIP and the protrusions of the dual heaters. Section 3.2 introduces the experimental setup for the flying touchdown. Section 3.3 describes a touchdown-based method to measure the angstrom-level LIP and studies slider dynamics under laser heating. The overall effect of the LIP and the FHC on the spacing change is investigated, and then they are separated using their different time constants. The slider dynamics is characterized using acoustic emission (AE) and laser Doppler velocimetry (LDV). Section 3.4 demonstrates that the head protrusion shape can be modulated by use of the dual heaters, and that the touchdown area can be controlled precisely. Section 3.5 concludes this chapter.

This work was completed jointly with Haoyu Wang and Siddhesh Sakhalkar. Haoyu Wang assisted with the LIP measurement. Siddhesh Sakhalkar performed simulations of minimum fly height during touchdown. I proposed the LIP measurement method and performed the flying touchdown experiments to study the slider dynamics and the dual heaters.

3.2 Experimental setup: flying touchdown

In the flying touchdown experiments, a component-level HAMR test stage was built as shown in Figure 3.3. A HAMR head flies over a rotating disk with the components (the heaters, the laser and the thermometer) controlled by PC via a data acquisition (DAQ) toolbox (two synchronized NI devices: PCI-6115 and USB-6211). It is noted that the HAMR heads used in this study contain the waveguide ($\sim$ 500 nm on the head surface) but no NFT. The heater and the laser were energized to perform the touchdowns on the rotating disk. The heater generated a protrusion by thermal expansion to reduce the head-disk spacing. Contact between the head and the disk was realized by increasing the heater power. The thermometer measured the head temperature rise, which is the same as Section 2. The touchdowns, namely the contact between the head and the disk, were indicated by an acoustic emission (AE) sensor that was attached to the head fixture as shown in Figure 3.3(b). There was also a laser Doppler velocimetry (LDV) beam above the head with the LDV spot focusing on the back of the slider, exactly on the laser diode. The optical surface analyzer (OSA) controlled the spindle speed.

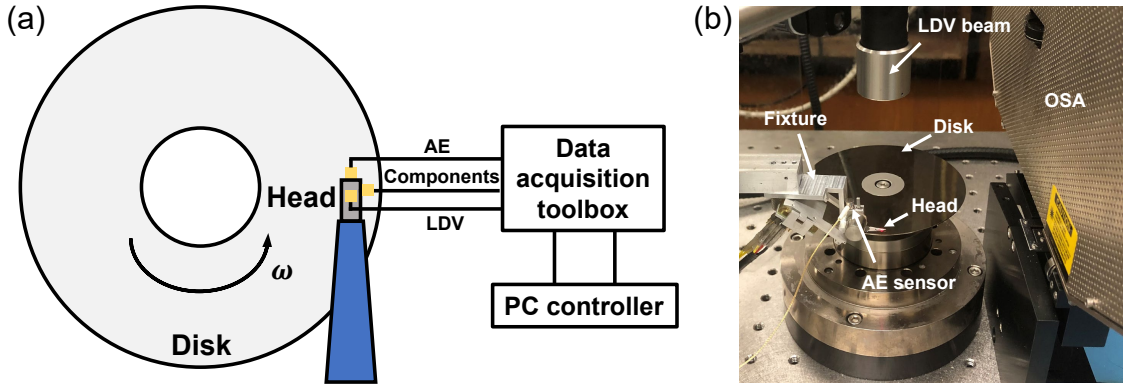

Figure 3.3: (a) A schematic diagram and (b) an overview picture of the experimental setup.

3.3 Laser-induced protrusion

3.3.1 Measurement method

The effect of laser heating on the spacing change is measured using the following touchdown-based method. When the laser is switched from OFF to ON, the touchdown power (TDP), indicated by an acoustic emission (AE) sensor, decreases due to spacing loss that results from laser heating. The touchdown power change (ΔTDP) is measured to study the LIP. We focus on the millisecond timescale effect of the laser heating during flying, and the measured ΔTDP is the overall outcome of the localized laser-induced protrusion (LIP, time constant $\tau_1 \sim \mu$s)

and the broad fly height change (FHC, time constant $\tau_2 \sim$ ms, not drawn in Figure 3.2) [86]. The ΔTDP's dependence on laser-on time, laser current and linear velocity is investigated.

The laser is biased using a constant DC current and the heater power is increased in steps (0.25 mW) to perform the touchdowns. The resolutions are 0.1 mA and 0.01 mW for the laser current and the heater power. Figure 3.4 shows a typical implementation of the heater power and the laser current. In each sampling period (120 ms), the laser is turned OFF in the first half of the sampling time (laser-off regime) and turned ON in the other half (laser-on regime). When the laser is turned ON, the laser passes through the waveguide and directly shines on the rotating disk. The TDPs measured in the laser-off regime and the laser-on regime are different due to the laser, and hence, the difference ΔTDP is measured to study the LIP. Since the heater power and AE signal are measured simultaneously in each sampling period, this implementation ensures identical initial conditions for both the laser-off regime and the laser-on regime, regardless of smear from the laser heating or wear from overpush touchdowns. Then different flying parameters such as laser-on time, laser current and linear velocity are controlled to study their effects.

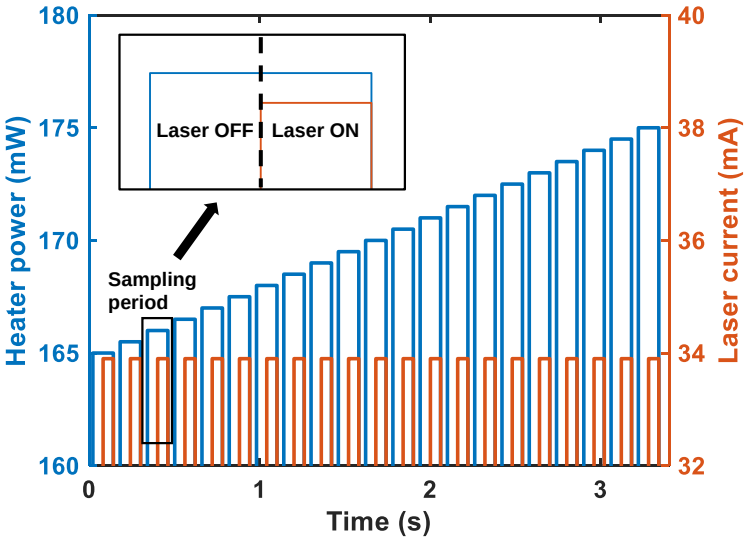

Figure 3.4: Sampling patterns in the experiments (inset: zoom in of one sampling period).

Figure 3.5 shows the AE signal results at different heater powers when flying at the linear velocity V = 18 m/s. Notice that the left and right halves, divided by the vertical red dash line in the sub-figures, correspond to the laser-off regime and the laser-on regime as demonstrated in Figure 3.4. When the heater power is 168.90 mW, the AE signal remains at its baseline value in both of the two regimes, so the head flies normally with the laser OFF and ON. Then, when the heater power is 170.90 mW or 173.90 mW, the appearance of the spikes in the right half indicates that contact occurs in the laser-on regime, but no contact is observed in the laser-off regime. At these two heater powers, the head keeps flying without

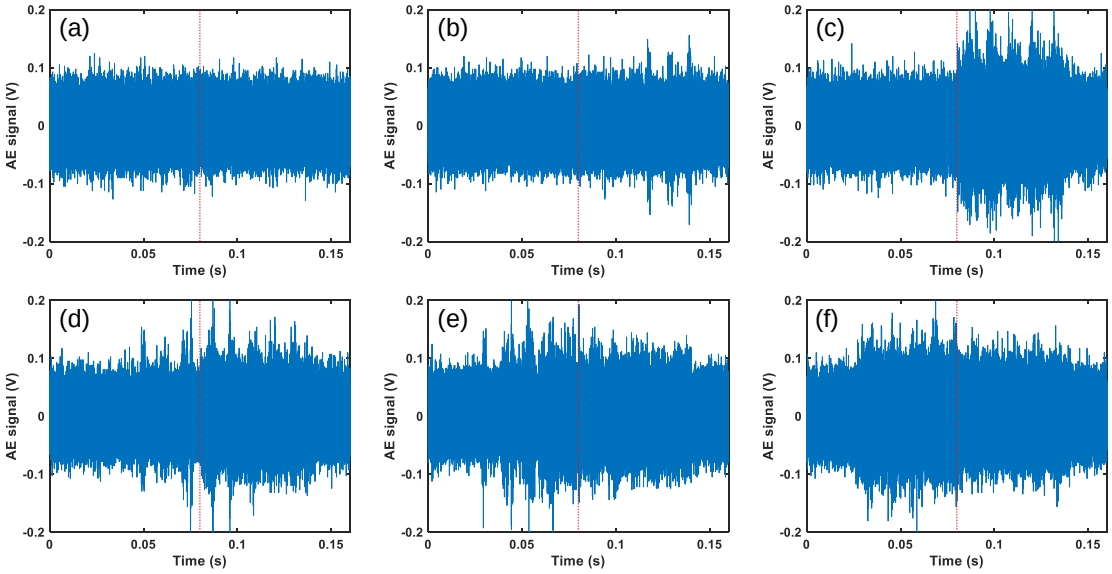

Figure 3.5: AE signals at the heater powers of (a) 168.90 mW (b) 170.90 mW (c) 173.90 mW (d) 175.40 mW (e) 175.90 mW (f) 176.90 mW when the laser current is 33.9 mA.

the laser, but turning on the laser induces spacing change (the LIP and the FHC), resulting in contact between the head protrusion and the rotating disk. Furthermore, Figure 3.5(b) does not show the contact until the laser remains ON for tens of milliseconds, which matches the time constant τ_2 of the FHC. When the heater power increases to 175.40 mW, 175.90 mW and 176.90 mW, the AE signals also indicate contact in the laser-off regime as well as in the laser-on regime. At these three heater powers, contact occurs even without the laser because the heater protrusion alone is too large compared to the head-disk spacing.

Figure 3.6 plots the root mean square (RMS) of the AE signal versus the heater power in the laser-off regime and the laser-on regime, which are also called touchdown curves, at the same flying conditions as in Figure 3.5. The two curves were measured simultaneously in each sampling period, so the only difference between them is the laser OFF/ON condition. The TDP is defined as the heater power where the AE RMS signal ramps up beyond 105% of its baseline value [94]. With the laser turned ON, the TDP decreases by several milliwatts due to the laser. In the following experiments, the ΔTDP is measured and the LIP is isolated using the time constants. Note that three states are observed in both the touchdown curves, which are termed "flying state", "bouncing state" and "surfing state" [95].

Assume that the transient responses of the LIP and the FHC can be described as

$$\begin{aligned} P_{\text{LIP}} &= A_1(1 - e^{-\frac{t}{\tau_1}}) \approx A_1 \quad (t \sim ms) \\ P_{\text{FHC}} &= A_2(1 - e^{-\frac{t}{\tau_2}}) \\ \Delta\text{TDP} &= P_{\text{LIP}} + P_{\text{FHC}} = -A_2 e^{-\frac{t}{\tau_2}} + A_1 + A_2 \end{aligned} \tag{3.1}$$

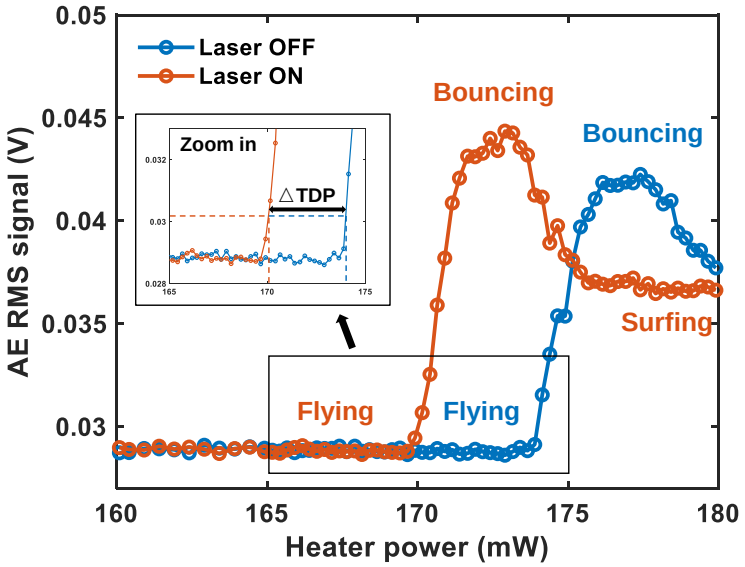

Figure 3.6: The result of ΔTDP due to laser heating (inset: zoom in of ΔTDP).

where P_X refers to the ΔTDP induced by the factor X (the LIP or the FHC) and A_1, A_2, τ_1, τ_2 are the amplitudes and the time constants of the LIP and the FHC, respectively. Figure 3.7 shows the relationship between the ΔTDP and the laser-on time with the linear velocity of 12, 18 and 24 m/s (3600, 5400, 7200 RPM) and the laser current of 40.8 mA, along with the exponential fittings. The fitting parameters can be found in Table 3.1. Figure 3.7 shows that the ΔTDP increases with the laser-on time, which matches the transient development of the LIP and the FHC at the surface of the recording head [86]. Table 3.1 indicates that the LIP and the FHC have similar contributions, and that the FHC time constant τ_2 is $\sim$ 5.6 ms in average. Thus, the ΔTDP needs $\sim$ 28 ms to reach steady state in all three cases. Actually the laser also results in a disk protrusion, however, which can be neglected because it is much smaller compared to the LIP and has a time constant in nanoseconds [34].

Velocity (m/s)	A_1 (mW)	A_2 (mW)	τ_2 (ms)
12	2.979	2.908	4.799
18	2.829	2.797	6.513
24	2.698	2.563	5.556

Table 3.1: Fitting parameters for the transient ΔTDP.

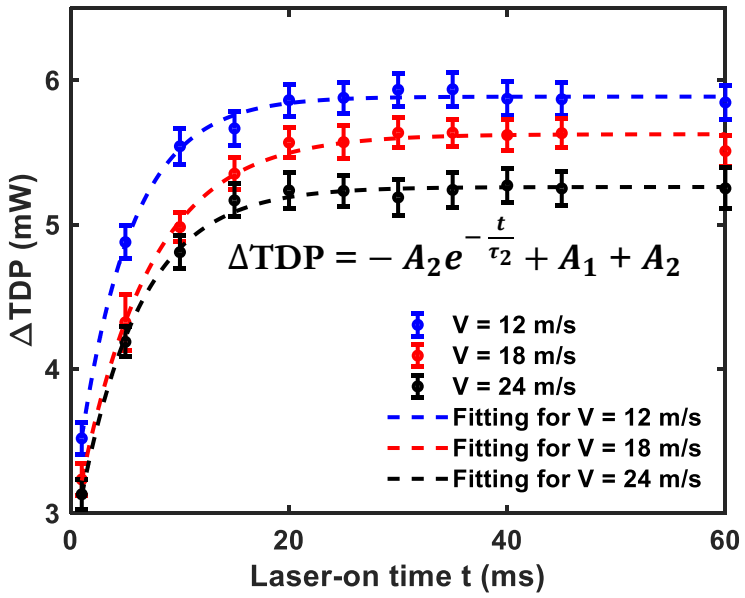

Figure 3.7: Relationship between the ΔTDP and the laser-on time when the laser current is 40.8 mA.

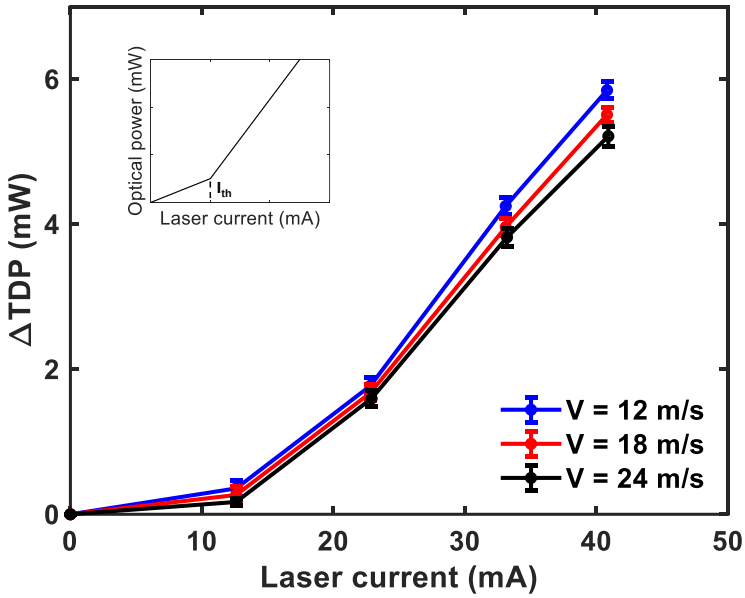

Figure 3.8: Relationship between the ΔTDP and the laser current (inset: the optical power versus the laser current [96]).

Figure 3.8 shows the relationship between the ΔTDP and the laser current at the same velocities. The laser-on time is fixed at 60 ms, which is long enough for the ΔTDP to become stable according to the experimental results in Figure 3.7. The ΔTDP has a two-stage linear relation with the laser current, which matches well with the previous calibration of the optical power with the laser current as shown in Figure 3.8 inset [96]. The LIP and the FHC are formed by the absorption of the output laser power and the thermal diffusion in the head. Hence, the ΔTDP caused by the laser is supposed to be proportional to the output laser power (optical power), which presents two slopes versus the laser current before/after the current threshold I_{th}.

So far, the touchdown power change (ΔTDP) has been used to evaluate the LIP, but the LIP size is not obtained yet. To do so, we need the heater efficiency (nm/mW) to convert the ΔTDP (mW) into absolute spacing (nm). Simulations based on CMLAir were performed using a similar slider [37]. Figure 3.9 shows the simulation results of minimum fly height versus the heater power at the three linear velocities. Since the ΔTDP is measured using the touchdown scheme, the heater efficiency near disk proximity, namely close to contact, is of interest. A constant heater efficiency near contact is assumed. The boxes in Figure 3.9 show that the heater efficiency is 0.0517, 0.0346 and 0.0281 nm/mW near disk proximity at V= 12, 18, 24 m/s, respectively. When flying at a higher velocity, the same amount of the heater power change corresponds to a smaller spacing change due to stronger air cooling and air pressure [40].

Using the heater efficiency (nm/mW) from the simulations, the ΔTDP (mW) can be

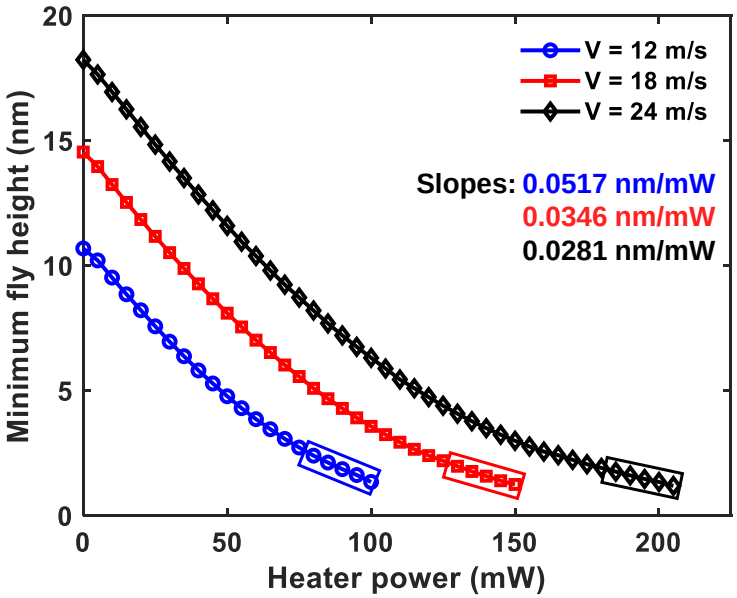

Figure 3.9: The simulation results of minimum fly height versus the heater power.

converted into the spacing change (nm), which arises from the LIP and the FHC. The LIP's portion is isolated by assuming a constant ratio A_1/A_2 at the same linear velocity. Figure 3.10 shows the separated LIP size versus the laser current. In the case of 40.8 mA laser current, the ΔTDPs measured in the three cases are 5.85, 5.51 and 5.21 mW with standard deviation $\sim$ 0.12 mW as shown in Figure 3.8, which can be converted by the heater efficiency into 3.02, 1.91 and 1.46 Å with standard deviation $\sim$ 0.05 Å. Considering the ratios A_1/A_2 in Table 3.1, the separated LIP sizes are 1.53, 0.96, 0.75 Å for the three velocities. Therefore, the LIP reduces by around half when the linear velocity increases from 12 m/s to 24 m/s, which is also caused by the stronger air cooling and air pressure.

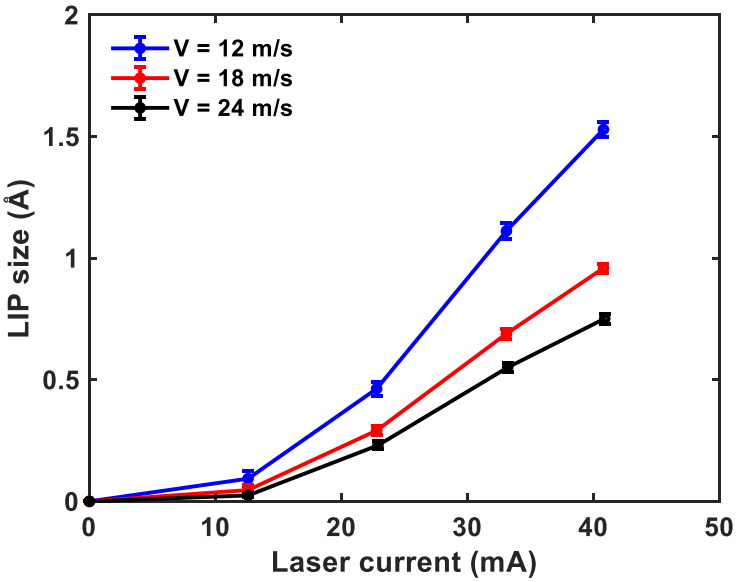

Figure 3.10: The measured LIP size as a function of the laser current and the linear velocity.

3.3.2 Effect on slider dynamics

This subsection investigates the effect of laser heating on slider dynamics. The flying touchdown experiments were performed with the laser turned ON. When the heater power increased beyond the TDP, contact occurred and the AE signal and LDV signal were recorded. The AE sensor was mounted on the head fixture as shown in Figure 3.3(b) and it detected the elastic vibrations produced by the head-disk contact events [97]. The LDV spot focused on the laser diode at the back of the slider. Therefore, the vibrations that happen during the head-disk contact can be evaluated from the AE and the LDV data.

Figure 3.11 shows the typical results of the temperature rise measured by the thermometer and the AE RMS signal during the flying touchdown achieved by increasing the heater power. As the head surface approaches the disk, the thermometer temperature increases first due

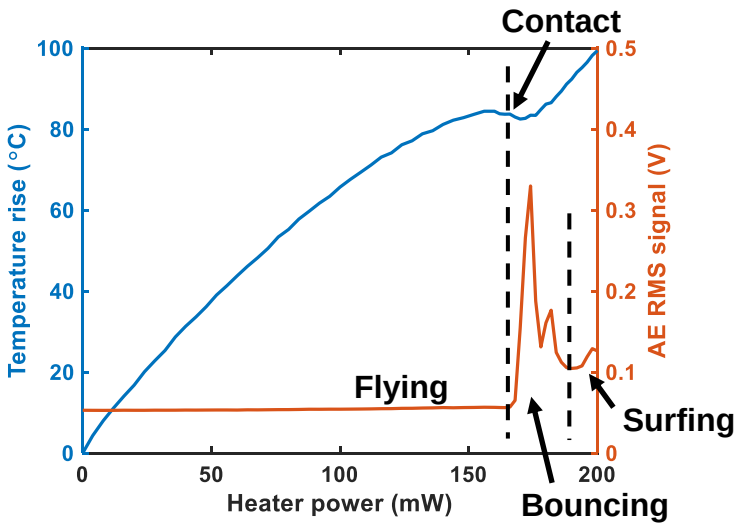

Figure 3.11: The temperature rise and the AE signal during the flying touchdown.

to the heater heating, then drops due to the enhanced thermal transport by phonon heat conduction (gap < 1 nm), and finally increases again due to the frictional heating caused by the head-disk contact. The AE RMS signal remains at its base value during flying, then undergoes a steep ramp-up at the start of the bouncing state and an oscillation during the bouncing state, and finally levels off to a value that is larger than the base value in the surfing state. It is observed from the AE RMS signal (the vertical dashed line) that the contact onset occurs at 168.0 mW, but the thermometer is still in the cooling stage at this moment, illustrating that the contact between the head and the disk is not complete and thus the frictional heating does not take effect yet. At this contact onset indicated by AE, contact only happens between the head protrusion and the disk surface asperities in terms of surface roughness. In the bouncing state, the head protrusion bounces on the rotating disk where the head's vibration is strong enough for its protrusion to randomly touch the disk surface regardless of the disk surface asperities [98]. With further increase of the heater power, the head protrusion comes into contact with the lubricant layer on the disk, featuring a second stable state besides the conventional flying state, which is called surfing state [95]. During the bouncing state and the surfing state, the frictional heating caused by the head-disk contact outweighs the thermal transport due to contact heat conduction, and this increases the thermometer's temperature again.

Using fast Fourier transform, the spectra of the AE signal and the LDV signal during the flying touchdowns are obtained and plotted in Figure 3.12 with the laser current of 0, 20.3 and 40.6 mA. The three states (flying, bouncing and surfing) are denoted in Figure 3.12(a1). When the laser is OFF, both the AE and the LDV spectra in Figure 3.12(a1,b1) show vibration modes near 210 kHz, 240 kHz and 300 kHz in the bouncing state and a 312 kHz

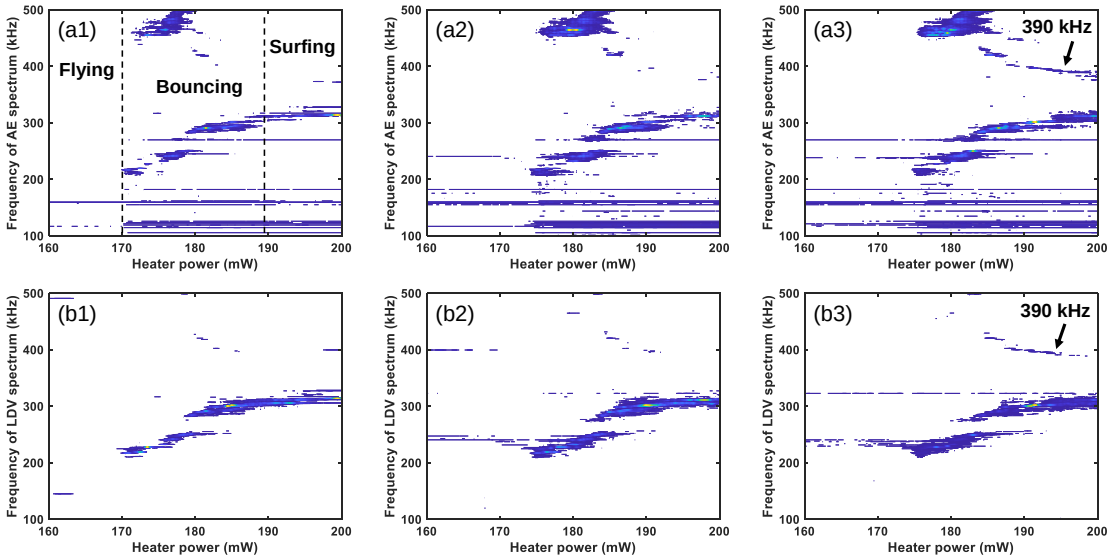

Figure 3.12: (a) AE spectra at the laser current of (a1) 0 mA (a2) 20.3 mA (a3) 40.6 mA. (b) LDV spectra at the laser current of (b1) 0 mA (b2) 20.3 mA (b3) 40.6 mA.

mode in the surfing state. The AE spectrum in Figure 3.12(a1) also shows the second harmonic of the modes near 240 kHz in the bouncing state. It is noted that the AE spectra in Figure 3.12(a1-a3) show modes near 160 kHz and 120 kHz even in the flying state, which should be inherent frequencies of the AE sensor because no physical contact occurs during flying. When the laser current increases from zero to 40.6 mA, Figure 3.12(a1-a3) show that more modes appear near 240 kHz and its second harmonic 480 kHz, and that a 390 kHz mode appears in the surfing state, which is also observed in the LDV spectra in Figure 3.12(b1-b3). The reason is likely that the localized laser-induced protrusion (LIP) comes into play and its interaction with the moving disk surface leads to more frequency modes.

3.4 Protrusions of dual heaters

HAMR operations may utilize two heaters to achieve different fly heights at the reader and the writer locations to improve the device efficiency as shown in Figure 3.13(a). Heater-1 is the commonly used heater that is embedded near the reader, while heater-2 is near the writer (if not stated explicitly, the term "heater" refers to heater-1). They can generate two thermal protrusions respectively shown as the black dashed lines drawn in Figure 3.13(a). The red dashed line is the sum of the two protrusion profiles, and it corresponds to the actual total protrusion. Figure 3.13(b) shows an AFM image of the head surface, where the thermometer is located at the center. By changing the dual heaters' powers, the total

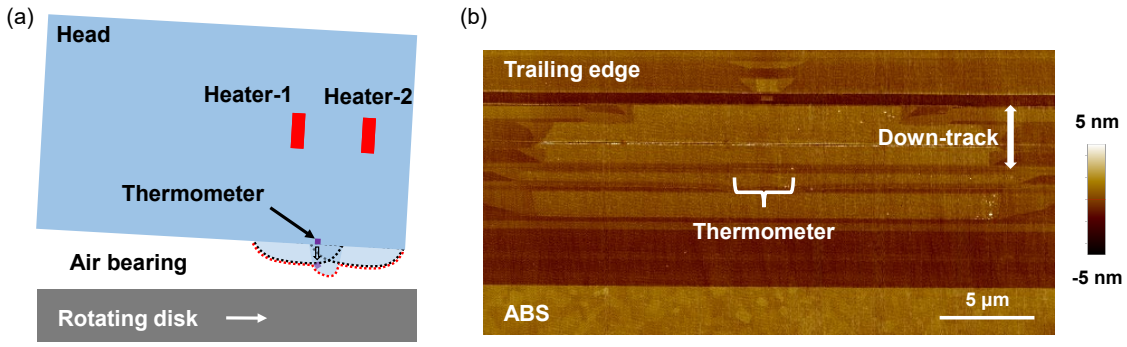

Figure 3.13: (a) A schematic diagram (not to scale) showing the dual heaters and their protrusion profiles (black dashed line: respective protrusion profiles; red dashed line: total protrusion profile). (b) An AFM image of the head surface showing the thermometer.

protrusion shape can be modulated. This section demonstrated that the thermometer can be at the peak of the total protrusion when using proper powers for the dual heaters.

The flying touchdown experiments were performed using the dual heaters in the following way. One heater was biased at a prescribed constant power, and the other heater was energized with an increasing power in steps such that the head-disk spacing was reduced to zero. Figure 3.14 shows the temperature rise measured by the thermometer and the AE RMS signal during the flying touchdown with increasing heater-1 power and a constant heater-2 power. Figure 3.14(a) shows that the thermometer undergoes a temperature translation ~ 97.8 °C when the heater-1 is OFF and the heater-2 power increases by 100.0 mW (heater-2

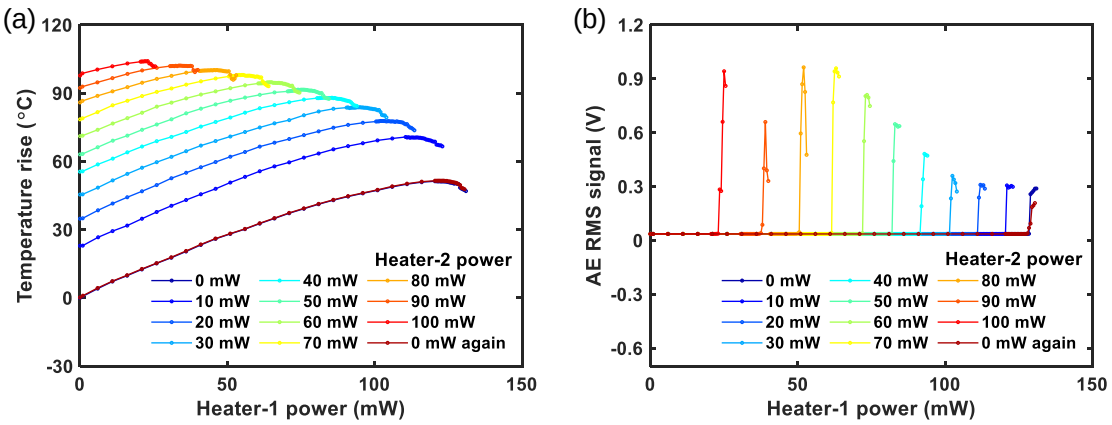

Figure 3.14: (a) The temperature rise and (b) the AE RMS signal as a function of the heater-1 power during the flying touchdown with a constant prescribed heater-2 power.

heating rate 0.98 °C/mW). Then, with the increasing power of heater-1, the head-disk spacing is reduced and contact occurs, which can be observed from the thermometer's cooling and the AE RMS signal's ramp-up shown in Figure 3.14(b). At a larger prescribed heater-2 power, a thermal protrusion by heater-2 exists in the head-disk interface, and thus a smaller heater-1 power is needed to realize contact. For example, Figure 3.14(b) shows that the initial touchdown power (TDP) is 128.2 mW using the heater-1 alone, while the TDP by heater-1 becomes 23.0 mW with a prescribed heater-2 power of 100.0 mW. The experiments were performed in the sequence of the legends in Figure 3.14. Finally, the 0 mW curve was repeated, and it coincides with the first 0 mW curve, which confirms that the head-disk interface does not change after multiple touchdowns.

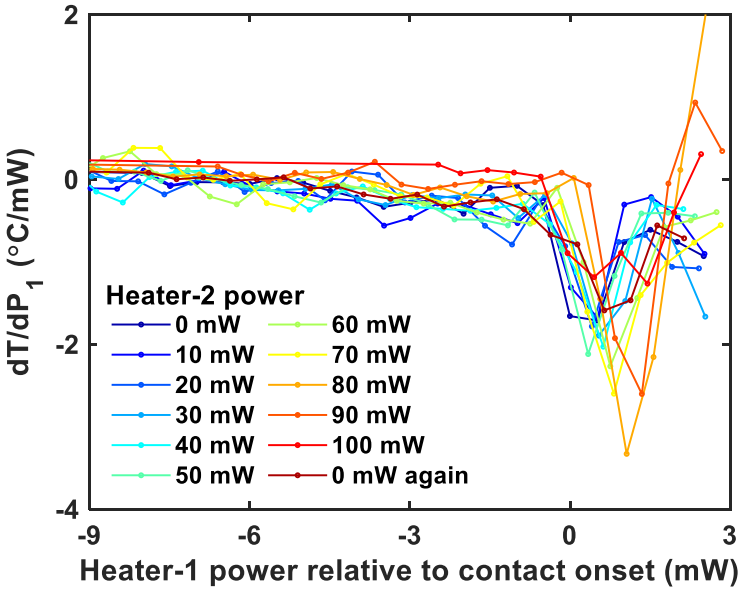

Figure 3.15: The dT/dP_1 as a function of the heater-1 power (relative to contact onset) during the flying touchdown with a constant prescribed heater-2 power.

To describe the thermal transport across the interface, the rate of change of the thermometer temperature rise with the heater-1 power, dT/dP_1, is extracted from Figure 3.14(a) and plotted in Figure 3.15, where the heater-1 power is denoted as the power relative to the contact onset with zero being the contact onset indicated by AE. The relative heater power essentially describes the spacing between the head protrusion and the disk surface. Figure 3.15 shows that the dT/dP_1 decreases with the spacing and has a minimum near 1 mW. The dT/dP_1 indicates the thermal transport across the head-disk interface. When the spacing decreases to zero, the stronger thermal transport carries the heater's joule heating away and cools the thermometer, resulting in a smaller dT/dP_1. After contact occurs, the minimum $(dT/dP_1)_{\min}$ corresponds to the maximum of total thermal transport including air

conduction, phonon heat conduction, contact heat conduction and frictional heating. Therefore, if the thermometer is at the peak of the protrusion and touches the disk surface first, the thermometer should have a smallest $(dT/dP_1)_{\min}$ due to the strongest thermal transport.

Figure 3.16 plots the $(dT/dP_1)_{\min}$ from Figure 3.15 as a function of the prescribed heater-2 power. The curve has the smallest $(dT/dP_1)_{\min}$ when the heater-2 power is 80.0 mW, indicating that the thermometer comes into contact with the disk surface first at this condition, where the heater-1 power is 51.0 mW. To put this in another way, the thermometer is located at the peak of the total protrusion with the heater-1 power of 51.0 mW and the heater-2 power of 80.0 mW. Therefore, by modulating the dual heaters' powers, the total protrusion's shape can be changed, and the touchdown area can be controlled at the thermometer's location.

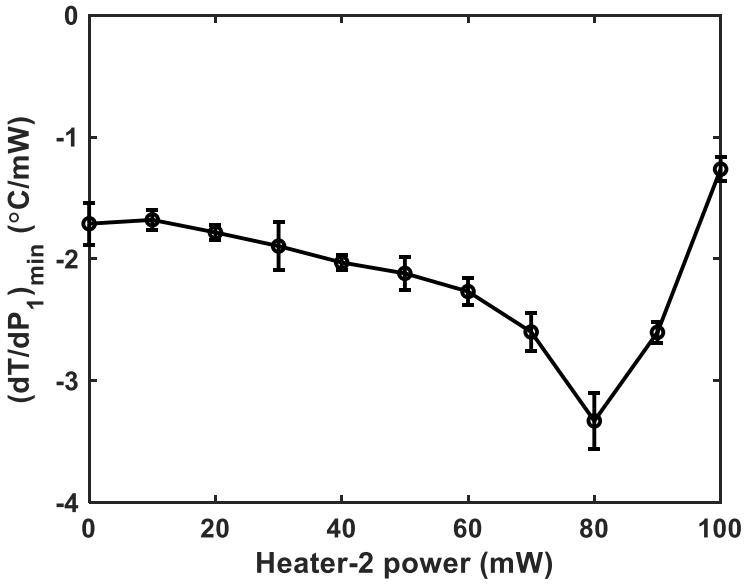

Figure 3.16: The minimum of the dT/dP_1 as a function of the heater-2 power during the touchdowns achieved by increasing heater-1 power.

Figure 3.17 shows the experiments performed in the opposite way, where the heater-1 was biased with a constant power and the heater-2 had an increasing power. Figure 3.17(a-b) show the temperature rise and the AE RMS signal during the flying touchdown achieved by increasing the heater-2 power. The thermometer's temperature translation by heater-1 is 0.48 °C/mW, which is much smaller than that by heater-2 (0.98 °C/mW) shown in Figure 3.14. The heating rate is dependent on the heater's parameters (size, distance from the thermometer) and the material parameters near the thermometer (thermal conductivity). For example, the thermometer is surrounded by metal shields as shown in Figure 3.13(b), which could affect the temperature at the thermometer location because the metals have higher thermal conductivity than the underlying alumina body (1.8 W/(m·K)) [18]. Fig-

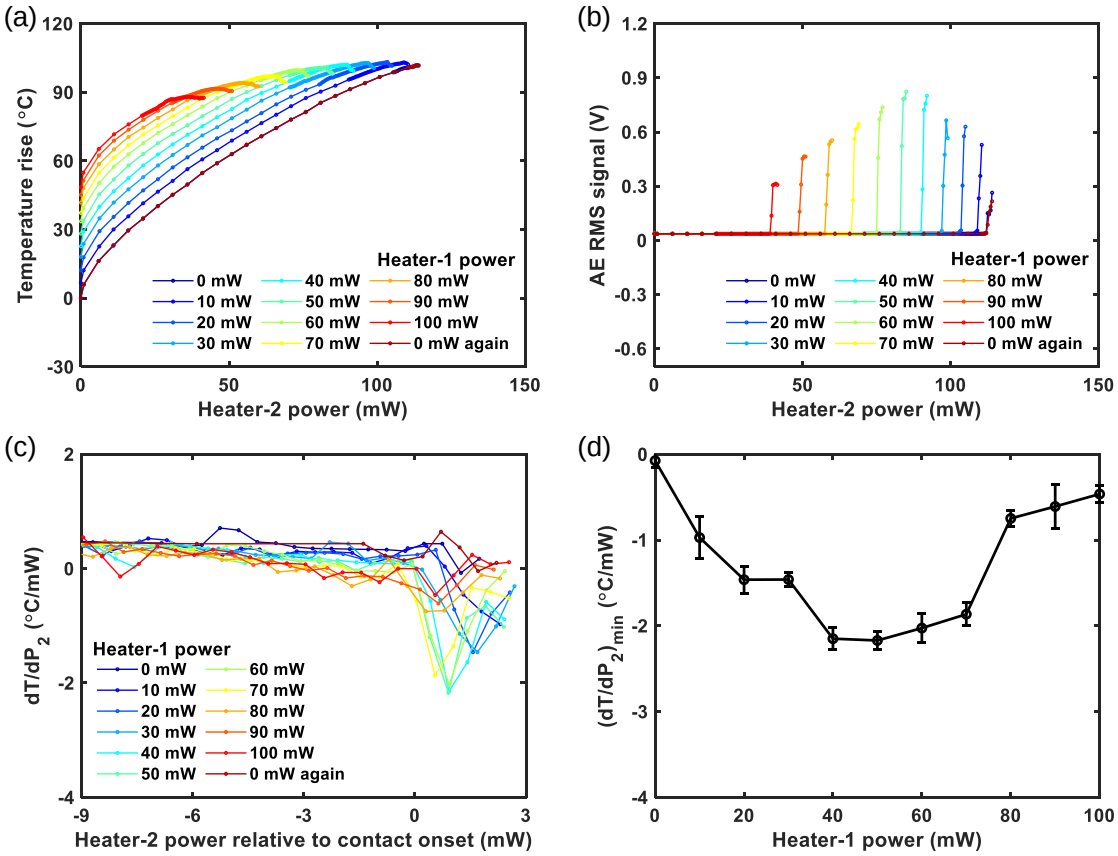

Figure 3.17: (a) The temperature rise and (b) the AE RMS signal as a function of the heater-2 power during the flying touchdown with a constant prescribed heater-1 power. (c) The dT/dP_2 as a function of the heater-2 power (relative to contact onset) during the flying touchdown with a constant prescribed heater-1 power. (d) The minimum of the dT/dP_2 as a function of the heater-1 power during the touchdowns achieved by increasing heater-2 power.

ure 3.17(c-d) show the extracted dT/dP_2 and $(dT/dP_2)_{\min}$ during the touchdown process. Similarly, the thermometer dT/dP_2 has a minimum near 1 mW after contact occurs. Figure 3.17(d) shows that the $(dT/dP_2)_{\min}$ is close to zero when the heater-1 power is 0 mW, indicating that the thermometer has almost no cooling during touchdown, which can also be seen in Figure 3.17(a). The reason is that the thermometer is far away from the center of heater-2 protrusion, and thus can not sense any cooling when the heater-2 protrusion alone touches the disk surface. The smallest $(dT/dP_2)_{\min}$ in Figure 3.17(d) occurs at the heater-1 power of 50.0 mW, where the heater-2 power is 83.5 mW from Figure 3.17(b-c). The results illustrate that the thermometer is at the peak of the total protrusion with the heater-1 power of 50.0 mW and the heater-2 power of 83.5 mW, which is very close to the circumstance derived from Figure 3.14–Figure 3.16 (51.0 mW and 80.0 mW for the dual heaters respec-

tively). Therefore, it is demonstrated that the head protrusion shape can be modulated by use of the dual heaters, and that the touchdown area can be controlled precisely.

3.5 Conclusion

We performed flying touchdown experiments to quantify the spacing change due to the laser heating in millisecond timescale during flying. When the laser was switched from OFF to ON, the touchdown power (TDP) decreased by several milliwatts, where the touchdown power change (ΔTDP) represents the spacing change induced by the laser. The spacing change originates from the localized angstrom-level laser-induced protrusion (LIP) and the fly height change (FHC), which can be separated using their time constants in μs and ms. The experimental results show that the FHC needs $\sim$ 28 ms to become stable, and that the LIP presents a two-stage relation versus the laser current. As the operating linear velocity increases from 12 m/s to 24 m/s, the LIP size reduces by around half due to the stronger air cooling and air pressure. The laser heating also affects the slider dynamics in that more vibration modes appear near 240 kHz and its second harmonic 480 kHz, and a 390 kHz mode appears according to acoustic emission (AE) and laser Doppler velocimetry (LDV) spectra, which is likely due to the mechanical interactions between the LIP and the moving disk surface.

The temperature of the thermometer was also measured during the flying touchdown by use of the dual heaters in the recording head. One heater was biased at a prescribed constant power, and the other heater was energized with an increasing power in steps such that the touchdown was achieved, or vice versa. Both the schemes show that the thermometer undergoes the strongest thermal transport (smallest $(dT/dP)_{\min}$) when contact occurs under the circumstance of the heater-1 power $\sim$ 50 mW and the heater-2 power $\sim$ 80 mW. And to sense the maximum thermal transport, the thermometer needs to be at the peak of the overall protrusion of the dual heaters such that it can touch the moving disk surface first. Therefore, it is demonstrated that the head protrusion shape can be modulated by use of the dual heaters, and that the touchdown area can be controlled precisely.

This chapter includes work published in *Applied Physics Letters* in 2020 (reproduced from [99], with the permission of AIP Publishing) and work presented at *ISPS-2020* [100] (with the permission from ASME).

Chapter 4

Thermally-induced material transfer in HAMR

4.1 Introduction

The head-disk interface (HDI) in heat-assisted magnetic recording (HAMR) is a system in which a laser beam is launched from a recording head and focused on a recording disk to facilitate data writing, as shown in Figure 4.1. The laser creates a hot spot on the recording disk to locally heat the magnetic layer to its Curie temperature and thus lower its coercivity. During the laser exposure, material transfer also happens due to the high level of thermal transport in the HAMR HDI. The temperature of the hot spot (400–500 °C) is much higher than the lubricant evaporation/decomposition temperature (150–250 °C) under

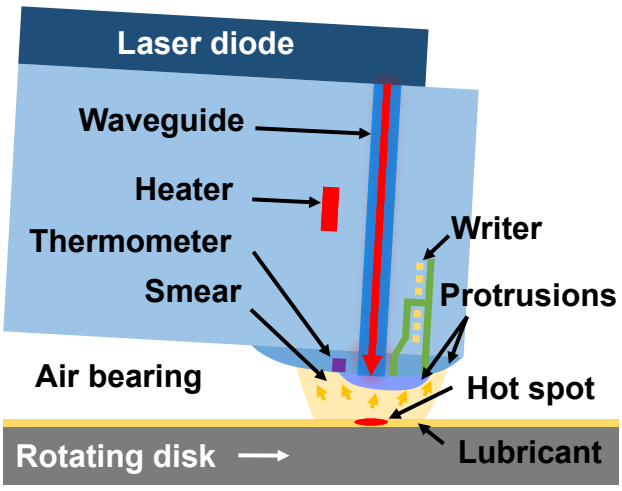

Figure 4.1: A schematic diagram (not to scale) showing the smear in the HAMR HDI.

HAMR operations [41–43], so the lubricant is evaporated/decomposed from the disk and then condenses on the head surface. The material accumulation on the head surface, also known as smear, is a challenging reliability issue for HAMR [14, 36]. The smear could affect the head's flyability as well as the heat transfer and the NFT efficiency of laser delivery in the HAMR head-disk interface, which may finally lead to the device failure [36, 101–103].

In previous studies, Raman *et al.* reported flyability failures due to contamination at the head-disk interface using a full body capacitance method [101]. Their experiments showed that the contamination could affect the flying height and result in a crash of the head-disk interface. Yang *et al.* studied the lubricant transfer and deposition from the disk to the head during HAMR writing, which was attributed to a temperature difference inversion at the head-disk interface [102]. Kiely *et al.* investigated the driving forces, growth mechanisms, and growth rates of head contamination, and they proposed an evaporation-condensation model [36]. They demonstrated that the head may be overheated and the NFT efficiency may be affected due to the presence of the contamination, which depends on the contamination properties. Xiong *et al.* found that the material accumulation on the head surface could be deposited back to the disk, where mechanical interaction played an important role [103]. To remove the contamination from the head surface, Aoyama *et al.* introduced a head cleaning procedure by placing the head surface in close proximity to the disk surface [104].

In this chapter, we experimentally investigate the smear formation mechanism and propose two smear mitigation strategies. Section 4.2 introduces the experimental setup and experimental parameters in the smear formation and smear mitigation. Section 4.3 studies effects of disk temperature and laser exposure time on the smear formation and discusses the smear formation mechanism. Section 4.4 proposes a mechanical approach and a thermal approach as smear mitigation strategies and presents the results on the head surfaces after the mitigation. Section 4.5 concludes this chapter.

4.2 Experimental setup: smear formation/mitigation

We performed experiments to generate/remove the smear for understanding the smear formation and its mitigation. The experiments were conducted using a component-level HAMR test stage as shown in Figure 4.2. A HAMR head (without NFT) flies above a rotating HAMR disk (5400 RPM) with a relative speed $\sim$ 15 m/s. The components in the head, including a heater, a writer, a laser and a thermometer, were controlled by a data acquisition (DAQ) toolbox (two synchronized NI devices: PCI-6115 and USB-6211). The heater was energized to create a local protrusion at the head surface, thus bringing it towards the disk. The writer was biased at -65 mA using a DC current source. The laser current was increased to calibrate the disk temperature. The thermometer embedded near the head surface (see Figure 4.1) was used to measure the head temperature, and an acoustic emission (AE) sensor was mounted on the head fixture to monitor the head-disk contact. The lubricant on the HAMR disk is perfluoropolyether-based Ztetraol multidentate, $\sim$ 1 nm thick, and has a bonding ratio between 70% and 85% [13]. The stationary head flies on a single track with

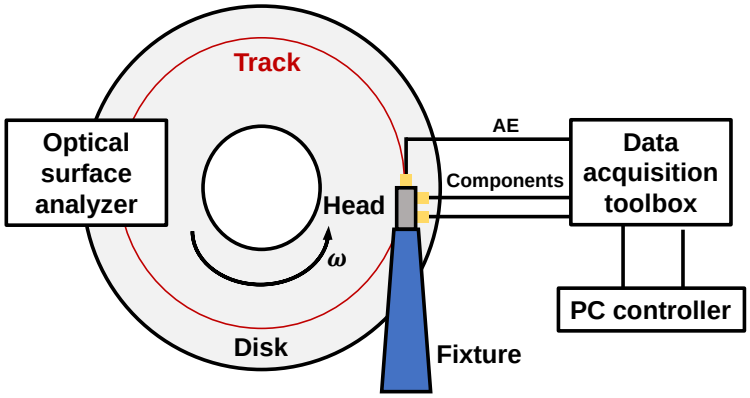

Figure 4.2: A schematic diagram of the experimental setup.

the track width ∼ 300 nm. An optical surface analyzer (OSA, Candela 5100), which was also located above the rotating disk, was used to in-situ characterize the lubricant uniformity in the track.

In the smear formation experiments, the heater power was kept at the touchdown power (TDP) minus 80 mW to maintain a head-disk clearance ∼ 5–6 nm, where the TDP denotes the heater power for which the heater protrusion comes into contact with the disk. The disk temperature and laser exposure time were controlled separately to investigate their effects on the smear formation. The smear that formed on the head surface was later characterized by atomic force microscopy (AFM). In the smear mitigation experiments, we first generated the smear on the head surface under a specific condition, and then adopted two strategies (mechanical/thermal) to remove the smear. The AFM images captured after the smear formation/mitigation display the formation/mitigation processes. The details of the experimental parameters can be found in Table 4.1.

Components	Smear formation	Mechanical mitigation	Thermal mitigation
Heater	TDP−80 mW	TDP−60 mW–TDP+2 mW	TDP−80 mW
Writer	−65 mA DC	OFF	OFF
Laser	ON, 0–40.8 mA DC	OFF	OFF/10.0 mA
Thermometer	ON, 1 mA DC	ON, 1 mA DC	ON, 1 mA DC

Table 4.1: Experimental parameters in the smear formation and mitigation experiments.

It is worth noting that the experimental conditions in this study differ from the actual HAMR writing conditions in the following aspects. First, the laser spot size on the disk here is ∼ 300 nm due to absence of the NFT, while the actual HAMR writing requires the spot size to be smaller than 50 nm [4]. Second, the laser exposure time in this study is

much longer than that in the actual HAMR writing (∼ns [4]). Hence, this study involves a larger hot spot with a longer exposure time, which is expected to produce smear of a larger volume. In this way, the long-term smear-related reliability issues can be investigated under the worst working conditions.

4.3 Smear formation

4.3.1 Effect of disk temperature

The effect of disk temperature on the smear formation is studied in this subsection. The disk temperature is dependent on the laser current, and the relationship between them needs to be calibrated. Figure 4.3 shows the calibration of the built-in laser diode in the HAMR head. The laser equivalent resistance and the laser consumed energy are plotted as a function of the laser current. It is noted that the laser equivalent resistance is the equivalent resistance of the laser diode. The curves show that the laser equivalent resistance decreases with the laser current and finally levels off to $\sim 80\ \Omega$. The laser consumed energy generally presents a linear relation with the laser current, which is used in the following calibration for the disk temperature.

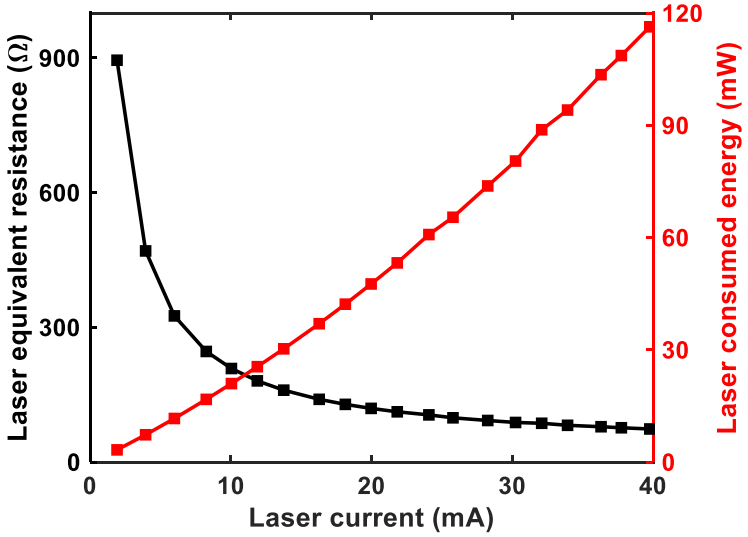

Figure 4.3: Calibration of the laser diode in the HAMR head.

Then HAMR writing was performed to calibrate the disk temperature. Figure 4.4 shows an OSA magnetic image of 20 sectors under HAMR writing with write current -65 mA and different laser currents, where sectors #1-#10 are location markers with a constant laser current (high enough to write), and sectors #11-#20 are the ones with increasing laser currents. Here, the head was moved radially by $\sim 10\ \mu$m to create a uniform band, due to the fact

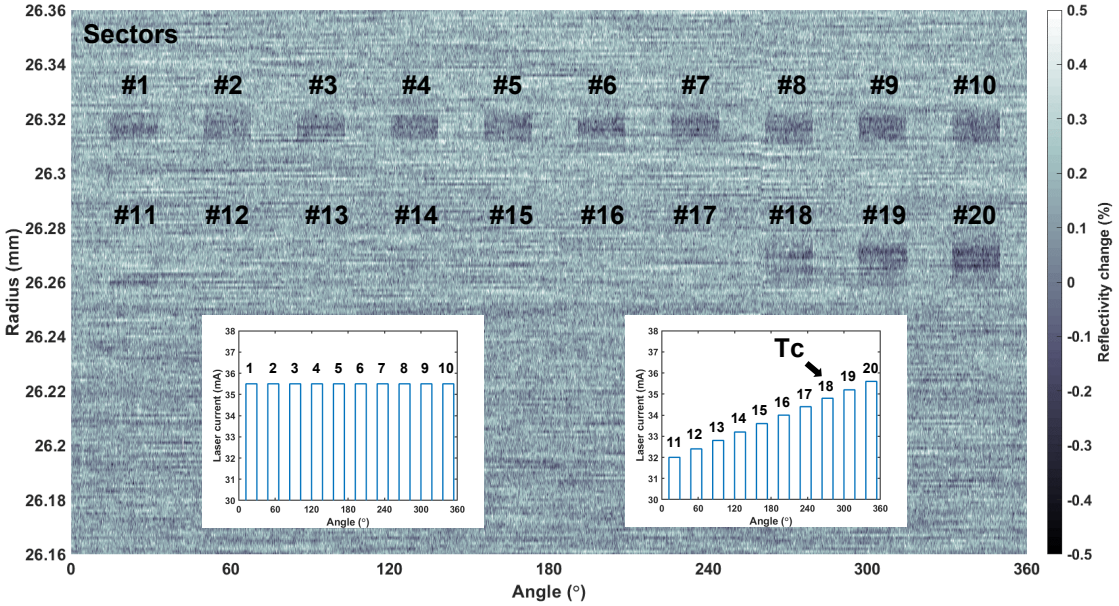

Figure 4.4: A magnetic image of 20 sectors under HAMR writing with different laser currents. Inset: the laser currents for the sectors.

that the laser spot size is $\sim$ 300 nm which is much smaller than the OSA's resolution in micrometers. It is observed that the writing effect does not appear until sector #18, indicating that the sector #18 is the writing onset, and its disk temperature corresponds to the magnetic layer's writing-onset temperature $\sim$ 367.0 °C [32] during the HAMR operations.

Also, the laser diode has a threshold I_{th} of 13.0 mA, below which no light emits. Since the laser consumed energy has an approximately linear relation with the laser current according to Figure 4.3, the disk temperature rise due to the laser heating is also assumed to be linear with the laser current. Then, linear interpolation and extrapolation were performed for the disk temperature calibration using the threshold datapoint (13.0 mA, 23 °C) and the writing-onset datapoint (34.5 mA, 367.0 °C) as plotted in Figure 4.5. As the laser current increased, the OSA was used to monitor the lubricant uniformity under the laser exposure. Figure 4.5 inset shows the reflectivity change at the lubricant depletion onset with the disk temperature of $\sim$ 220 °C. The depletion is dominated by lubricant evaporation instead of decomposition under our experimental conditions [35]. Therefore, the positive peak in Figure 4.5 inset implies that the lubricant within the band was depleted during the laser exposure, and that the lubricant has an evaporation temperature $\sim$ 220 °C.

With the disk temperature calibrated using the writing-onset temperature, we then study its effect on the smear formation. Figure 4.6 shows the AFM images of the smear on the head surface at different disk temperatures (a1) 119.0 °C (a2) 272.6 °C (a3) 367.0 °C (a4) 467.8 °C with a constant laser exposure time of 111.1 s (10^4 revolutions). The AFM images

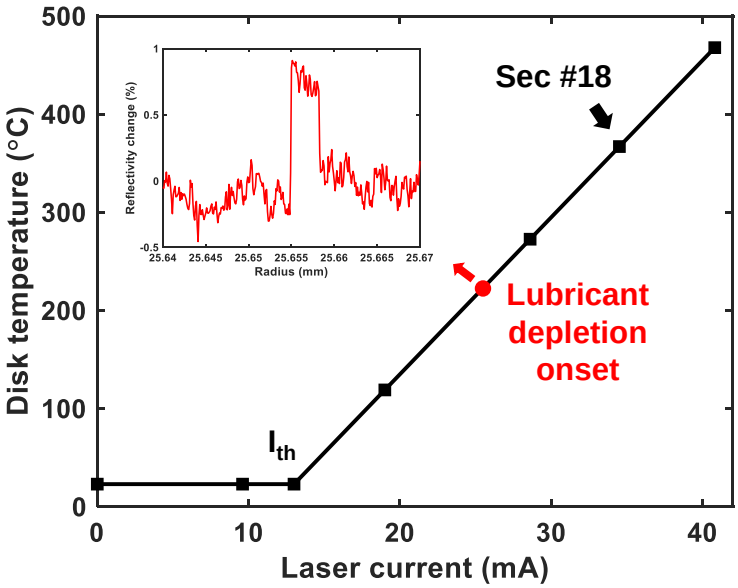

Figure 4.5: Calibrated disk temperature. Inset: reflectivity change of the band at the lubricant depletion onset.

were scanned at scan angle 45 degrees to avoid imaging artifacts. The waveguide (WG) location on the head surface is marked in Figure 4.6(a1), which is where the laser comes out of the head. The cross-track and down-track directions are also denoted in Figure 4.6(a1). The relative sliding speed between the head and the disk was along the down-track direction with a zero skew angle. In Figure 4.6(a1), no smear appears because the disk temperature 119.0 °C is much lower than the lubricant evaporation temperature $\sim$ 220 °C. For higher disk temperatures (272.6–467.8 °C), the smear forms in the shape of traces as shown in Figures 4.6(a2-a4). Figure 4.6(a2) shows that the smear traces originate from the WG location and form along the down-track direction, in both the downstream and upstream paths. The disk rotates towards the downstream down-track direction, so the air flow carries the lubricant evaporation generated near the WG location to the downstream head surface, and thus the lubricant condenses there as the smear. The smear also forms upstream from the WG location, which is caused by the mechanical interaction between the head and the disk [36, 103]. The smear fills the head-disk gap and then materials on the disk are picked up and transferred from the disk to the upstream head surface by mechanical contact, as illustrated in Figure 4.1. Figures 4.6(a3-a4) show that the smear evolves upstream as far as the AlTiC air bearing surface (ABS). Also, the AFM images show that the smear is primarily positioned along the two down-track sides of the WG location ($\sim$ 350 nm from the center), which is possibly because the thermocapillary stress dominates and pushes the condensed lubricant away from the down-track central line [82]. Furthermore, particulate-like smear is observed in Figure 4.6(a4), which comes from the magnetic layer [105], indicating that the

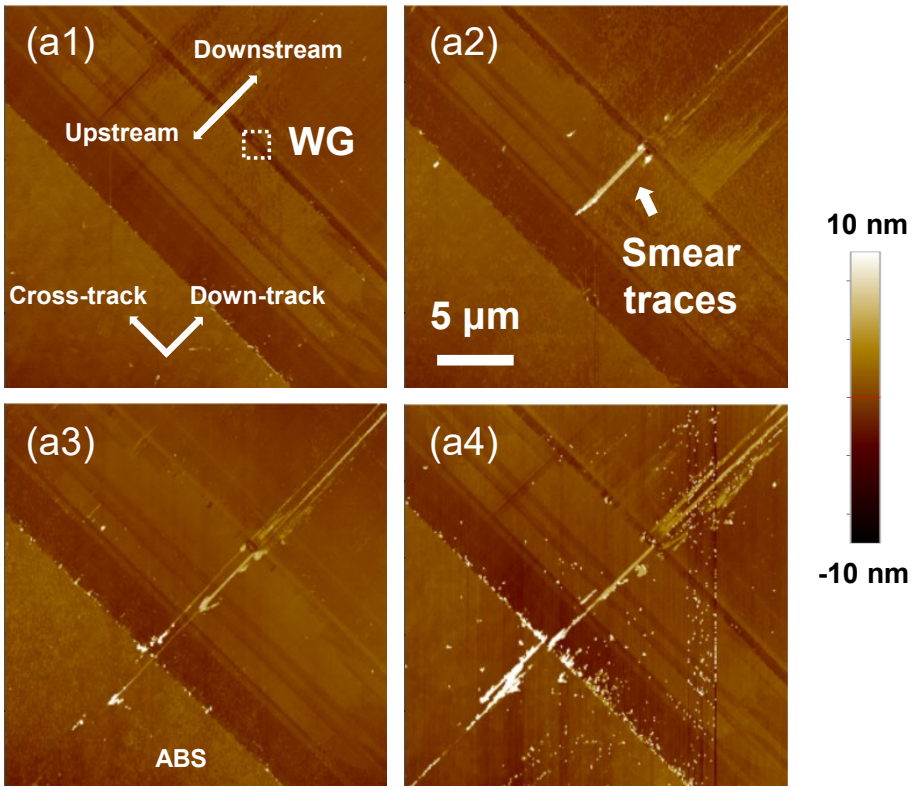

Figure 4.6: AFM images of the smear on the head surface at the disk temperature (a1) 119.0 °C (a2) 272.6 °C (a3) 367.0 °C (a4) 467.8 °C with a constant laser exposure time of 111.1 s.

lubricant and carbon protective layer may be depleted completely and the magnetic layer is damaged under such a high temperature 467.8 °C. It is also observed from Figure 4.6 that the volume of the smear that forms when the disk temperature is higher than the lubricant evaporation temperature ($\sim$ 220 °C) increases with the disk temperature.

4.3.2 Effect of laser exposure time

Next we investigate the effect of the laser exposure time on the smear formation. Figure 4.7 shows the AFM images of the smear on the head surface at different laser exposure times (a1) 1.1 s (a2) 11.1 s (a3) 111.1 s (a4) 1111.1 s with a constant disk temperature of 367.0 °C (writing-onset temperature). The disk temperature is higher than the lubricant evaporation temperature, but there is no smear present in Figure 4.7(a1), which indicates that the laser exposure time 1.1 s is too short for the smear to form on the head surface. One possible mechanism is that the laser-induced lubricant depletion can not recover after one revolution,

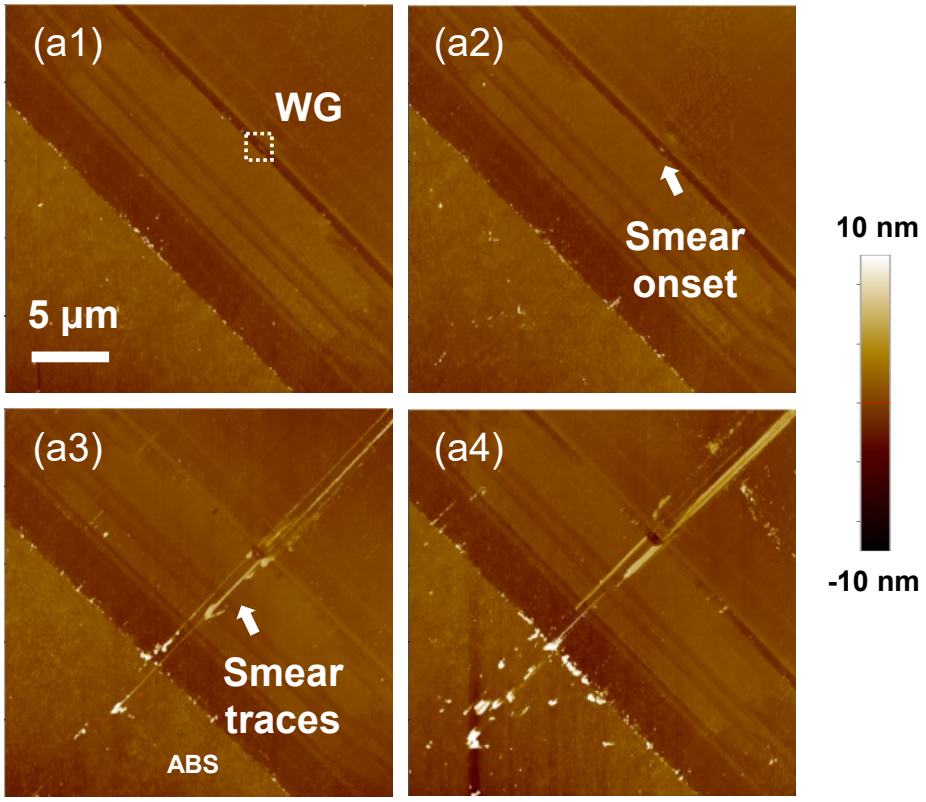

Figure 4.7: AFM images of the smear on the head surface at the laser exposure time (a1) 1.1 s (a2) 11.1 s (a3) 111.1 s (a4) 1111.1 s with a constant disk temperature of 367.0 °C.

and thus accumulates on the disk. Finally, some time is needed for the depleted lubricant to be transferred to the head surface, either by the evaporation-condensation process or mechanical interaction. At the laser exposure time 11.1 s, Figure 4.7(a2) shows a small smear dot exactly at the WG location, which is assumed to be the onset of the smear formation. Then, the smear dot evolves into traces over time which extend to the AlTiC ABS as well, as shown in Figures 4.7(a3-a4). When the disk temperature is higher than the lubricant evaporation temperature, it takes a certain time (a value between 1.1 s and 11.1 s in this study) for the smear to form on the head surface. Thereafter, the generated smear volume increases with the laser exposure time.

To better understand the smear formation, we plot in Figures 4.8 the down-track height profiles of the smear from Figure 4.7. Figure 4.8(b) shows the zoom-in height profiles of Figure 4.8(a) near the WG location. In Figure 4.8(a), the locations of the ABS, the heater protrusion and the WG are marked in the down-track position. For the laser exposure time 1.1 s, no smear appears in Figure 4.8, so the blue curve is the height profile of the head surface without any smear. When the laser exposure time is 11.1 s, a smear dot of $\sim$ 2 nm high

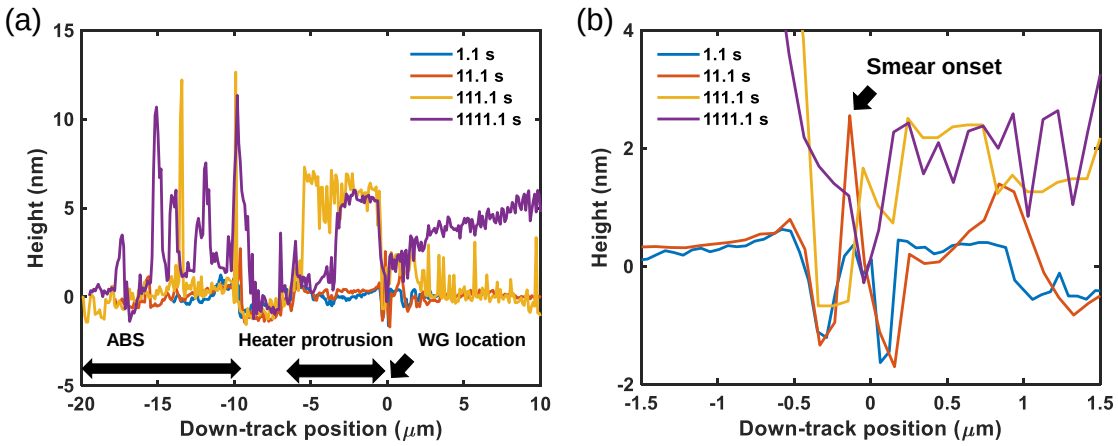

Figure 4.8: (a) Height profiles of the smear along the down-track direction and (b) their zoom-in near the WG location.

shows up at the WG location in Figure 4.8(b), which is the smear formation onset. For the cases of longer laser exposure times 111.1 s and 1111.1 s, Figure 4.8(a) shows that the smear forms both downstream (positive x axis) and upstream (negative x axis). In the downstream direction, the yellow curve (111.1 s) shows some discrete smear, while the purple curve (1111.1 s) presents a continuous smear trace, indicating that the smear accumulates over time. The smear is also observed at the heater protrusion location. During the experiments to generate the smear, the physical clearance between the heater protrusion and the disk was kept $\sim$ 5–6 nm, so the smear height can not exceed this value. In Figure 4.8(a), the smear height near the heater protrusion location is exactly $\sim$ 5–6 nm, which implies that the smear grows and fills the head-disk gap. Moreover, several smear dots are seen at the ABS location and their heights have a maximum value $\sim$ 12 nm, which is related to the initial head-disk clearance $\sim$ 10–15 nm. There is no protrusion bulging on the AlTiC ABS, so the smear height on the ABS is limited by the initial clearance. With the head-disk interface filled with the smear at the heater protrusion location, the mechanical contact drives the materials on the disk to the head surface upstream, forming the smear dots on the ABS. In summary, the height profiles in Figures 4.8 verify that the smear can fill the head-disk interface gradually, and later grow upstream to the ABS, which is caused by the mechanical interaction between the smear on the head surface and the rotating disk.

The experimental results in Figure 4.6 and Figure 4.7 show that the smear begins to form when the disk temperature is higher than the lubricant evaporation temperature, and the evaporation occurs for a certain time, which is long enough for the lubricant evaporation to reach the head surface and condense. The smear originates from the WG location and forms into traces along the down-track direction. The smear traces are primarily located at a distance from the track center, which is likely due to the thermocapillary stress. Particulate-

like smear that comes from the magnetic layer appears at a higher disk temperature. And the smear volume increases with the disk temperature and the laser exposure time.

4.4 Smear mitigation

4.4.1 Mechanical approach

Since the smear grows and fills the head-disk interface gradually as shown in Figure 4.8, the smear can be mitigated by moving the head surface closer to the rotating disk surface. In this way, the smear on the head surface touches the rotating disk surface and is burnished away due to frictional interactions, which is referred to as a mechanical approach.

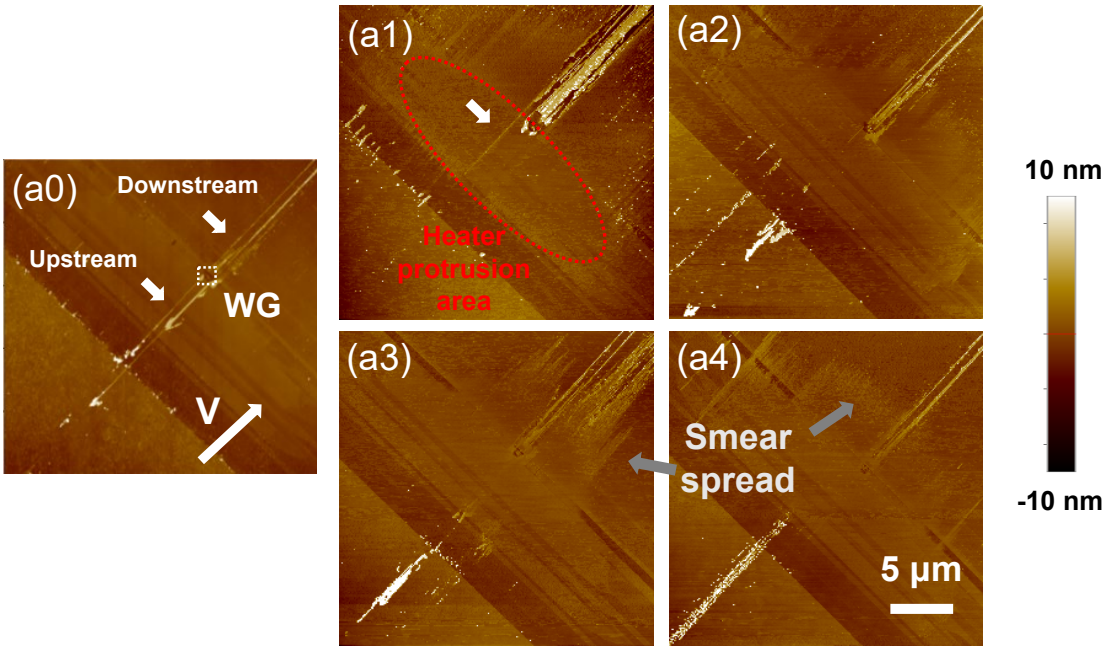

Figure 4.9: AFM images of the smear on the head surface (a0) before mitigation (a1-a4) after mitigation at the heater power of (a1) TDP−60 mW (a2) TDP−40 mW (a3) TDP−20 mW (a4) TDP for 10 r.

The smear was generated on multiple samples at the heater power of TDP−80 mW with a head-disk clearance ∼ 5–6 nm, the disk temperature of 367.0 °C (writing-onset temperature) and the laser exposure time of 111.1 s (the same condition as Figure 4.6(a3) and Figure 4.7(a3)). Then, the laser and the writer were switched OFF to stop the smear formation, and the heater was energized at TDP−60 mW, TDP−40 mW, TDP−20 mW, and TDP for ten revolutions (0.11 s) to have a smaller physical spacing between the head and the

disk for the smear mitigation. The results are displayed in Figure 4.9. Figure 4.9(a0) shows the smear before mitigation with the WG location and the downstream/upstream directions denoted. Figure 4.9(a1-a4) show the smear after mitigation by use of larger heater powers (smaller physical spacings), where the heater protrusion area is marked in Figure 4.9(a1). It is clearly seen that the smear in the heater protrusion area (red dashed oval) is removed effectively. Figure 4.9(a1) shows a clean heater protrusion area except one thin smear trace because the heater protrusion at TDP−60 mW can not cover the head-disk spacing completely and some smear remains. As the heater power increases in the mitigation step, Figure 4.9(a2-a4) show a cleaner heater protrusion area, indicating that the smear in this area is totally burnished away. It is noted that the upstream smear on the AlTiC ABS and the downstream smear are not removed because they are positioned out of the heater protrusion area, so the heater protrusion can not cause contact at their positions to remove them. In addition, Figure 4.9(a3-a4) also show spread of the smear to the downstream direction, which is due to the heater protrusion's burnishing. The smear, which is originally located within $\sim$ 350 nm from the down-track central line passing the WG location, is later burnished downstream to a broad area ($\sim$ 7 μm from the down-track central line).

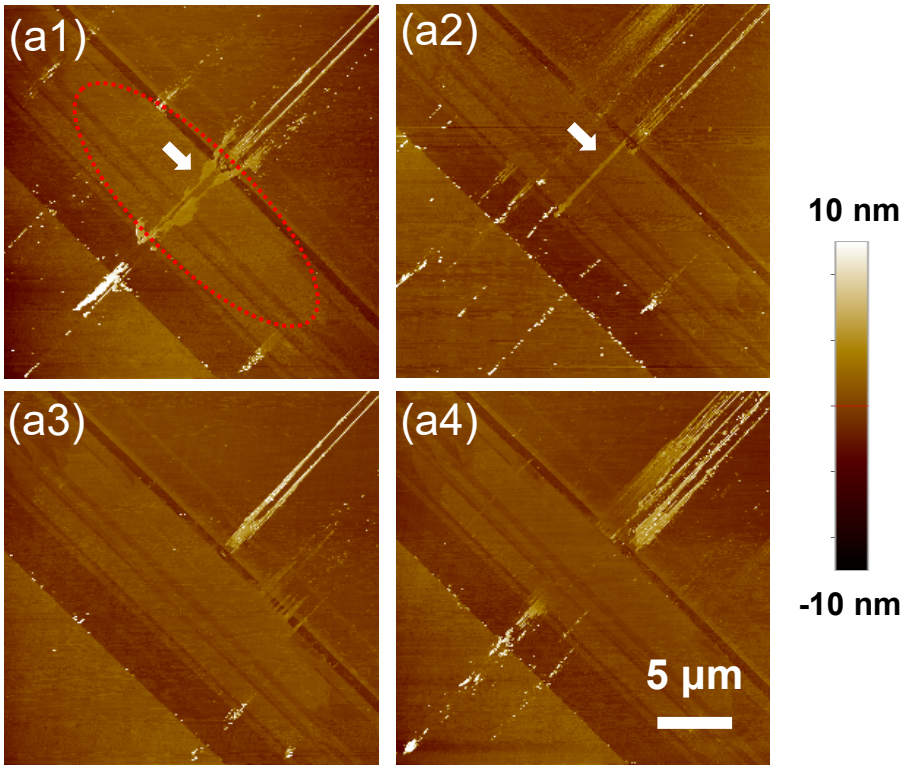

Figure 4.10: AFM images of the smear on the head surface after mitigation at the heater power of TDP−20 mW for (a1) 1 r (a2) 2 r (a3) 5 r (a4) 10 r.

Next we study the effect of duration in this mechanical mitigation strategy. Figure 4.10 shows the AFM images of the smear on the head surface after mitigation at the heater power of TDP−20 mW for one to ten revolutions. Figure 4.10(a1) still shows some smear (~ 2 μm wide in the cross-track direction) in the heater protrusion area (red dashed oval) because one revolution (0.011 s) is not long enough to remove the smear completely. Figure 4.10(a2) shows that the second revolution mitigates the smear in the heater protrusion area to a thinner trace $\sim$ 400 nm wide. At longer durations of 5 r and 10 r, it is observed from Figure 4.10(a3-a4) that the smear in the heater protrusion area are removed effectively, the same as Figure 4.9(a3). Therefore, several revolutions (5 r) are enough for the smear mitigation by this approach. Similarly, the upstream smear on the AlTiC ABS and the downstream smear can not be mitigated. It is noted that Figure 4.10(a1-a4) show different amounts of smear on the upstream ABS or downstream area, which is due to sample-to-sample variance.

Particularly, the effect of the smear on touchdowns is studied here. During the touchdowns, the heater power was increased to TDP+2 mW as a slight overpush process, which refers to the case with the heater power exceeding the TDP [98]. Thus, the heater protrusion filled the head-disk spacing and came into contact with the surface of the rotating disk with an overpush force. The writer and the laser were OFF. Ten repeated touchdowns were performed using a head that already had some smear on its surface. Figure 4.11(a) shows the AFM images of the head surface with smear and after ten repeated touchdowns. Clearly, the smear present in Figure 4.11(a1) is mostly gone after the touchdowns, except for some particles which are not positioned in the heater protrusion area. Besides, it is noted that the smear on the upstream ABS and the downstream area becomes less as well. The mechanism for the smear mitigation outside of the heater protrusion area has not been revealed, but one possible explanation is that the high shear air flow carries the poorly-bonded smear away in the overpush process. The comparison in Figure 4.11(a) demonstrates that the overpush touchdowns can remove the smear more effectively due to the frictional interactions induced by the overpush force.

Figure 4.11(b-c) show the root mean square (RMS) of the AE signal and the head temperature rise as a function of the heater power during the ten touchdowns, respectively. For each data point, the heater power was maintained for 0.11 s (10 revolutions) to obtain the AE RMS signal and the average temperature rise. Interestingly, Figure 4.11(b) shows that the 1st touchdown curve differs from the other curves (2nd-10th touchdowns, the same as without any smear) in that it has some AE signal higher than the baseline value ($\sim$ 0.039 V) at the heater power between 66 mW and 122 mW. This unusual signal during the 1st touchdown is caused by the smear removal. The heater power 0-122 mW (TDP) in Figure 4.11(b) corresponds to the spacing between the head surface (without any protrusion) and the disk surface. During the smear generation experiment for the head shown in Figure 4.11(a1), the heater power was 42 mW (TDP−80 mW) and the writer was energized with its protrusion equivalent to $\sim$ 20 mW heater power change, so the heater protrusion and the writer protrusion correspond to the regions 0–42 mW and 42–62 mW as denoted in Figure 4.11(b). The laser-induced protrusion is neglected here because it is only several

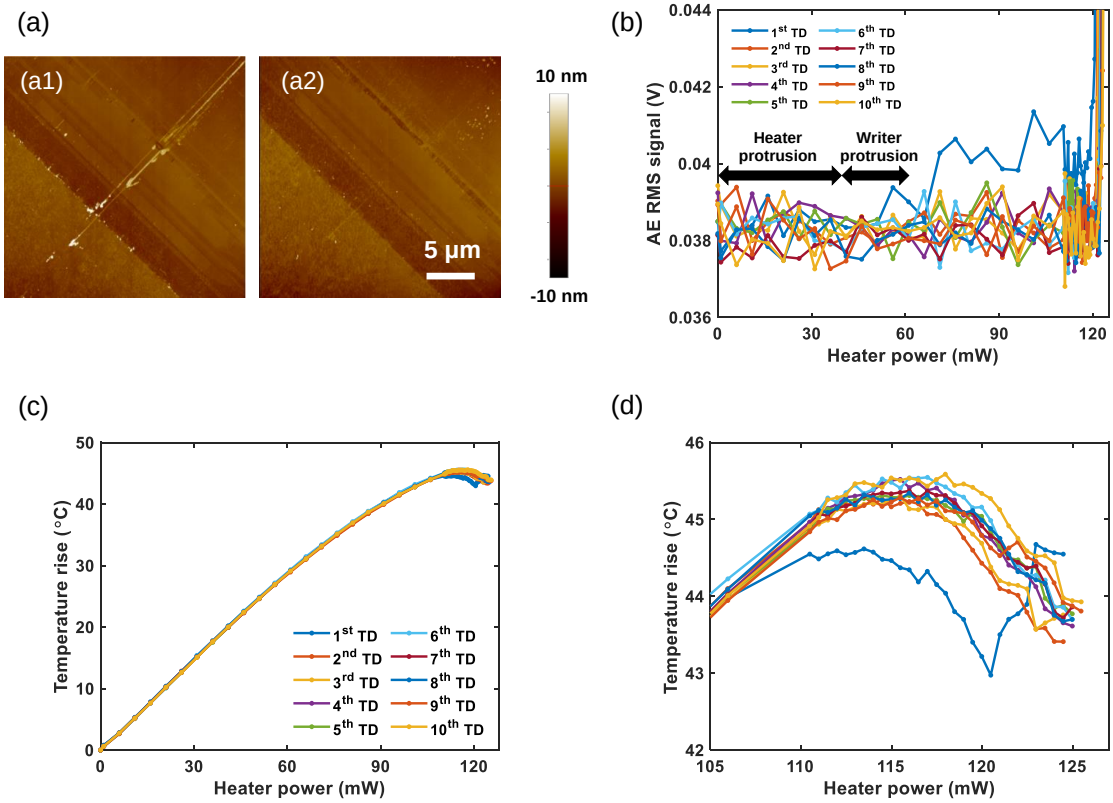

Figure 4.11: Effect of the smear on touchdowns (TDs). (a) AFM images of the head surface (a1) with smear and (a2) after 10 repeated touchdowns (TDP+2 mW). (b) AE RMS signal as a function of the heater power during the touchdowns. (c) Head temperature rise as a function of the heater power during the touchdowns and (d) its zoom-in near contact.

angstroms according to Section 3.3. The smear filled the gap between the head protrusion (heater protrusion + writer protrusion, 0–62 mW) and the disk, and thus could only occupy the region 62–122 mW, which is exactly where the unusual AE signal appears. This indicates that the smear was removed by the frictional interactions from the head-disk contact, which produced vibrations and was detected by the AE sensor. Moreover, this AE signal that appears in the region 62–122 mW vanishes from the 2nd touchdown to the 10th touchdown, implying that the smear was primarily burnished away during the 1st touchdown and that there is no smear effect thereafter.

The head temperature measurement shows a similar feature that the 1st touchdown curve is different from the other ones (the same as without any smear). Figure 4.11(c) and its zoom-in Figure 4.11(d) show that the head temperature rise is lower ($\sim$ 2 °C) during the 1st touchdown and gets back to normal from the 2nd touchdown, indicating that the smear removal leads to more thermal transport before the real touchdown that occurs at 122 mW.

The smear likely forms a material bridge at the head-disk interface and transfers the heat across it, lowering the head temperature. And the smear is primarily removed during the 1st touchdown, so the frictional heating is expected to be negligible as the smear is burnished away. In addition, the components in the head had the same resistances before/after the slight overpush process. And the thermometer, the most fragile element in the head, worked well after the +2 mW overpush touchdowns, indicating that the head remained functional. Therefore, the slight overpush process can be a more effective mechanical approach for smear mitigation without damaging the head.

So far, we have always used one heater to perform the mechanical burnishing in the smear mitigation. Nowadays, HAMR heads contain a second heater that is used to achieve more advanced spacing control as discussed in Section 3.4. Next, we investigate the smear mitigation using the second heater as well. Figure 4.12(a) shows the locations of the dual heaters. Heater-1 is the commonly used heater and is embedded upstream with regard to the WG location, while heater-2 is embedded downstream (if not stated explicitly, the term "heater" refers to heater-1). Figure 4.12(b) shows the smear after mitigation using the heater-2. The smear was generated at the heater-1 power of TDP−80 mW, the disk temperature of 367.0 °C and the laser exposure time of 111.1 s (the same condition as Figure 4.9(a0)), and was then mitigated at the heater-2 power of TDP+2 mW as a slight overpush process. An expected area of the heater-2 protrusion is marked in Figure 4.12(b). It is observed that the downstream smear and partial upstream smear are removed as compared to Figure 4.9(a0), with a small amount of smear remaining near the AlTiC ABS. Thus, the heater-2 can be used to address the downstream smear issue, which can not be fulfilled by use of the heater-1. To summarize, this subsection shows that the upstream/downstream smear can be mitigated by the heater-1 and the heater-2 respectively thanks to their distinct locations, which can be implemented as a practical application in the HAMR hard disk drive technology.

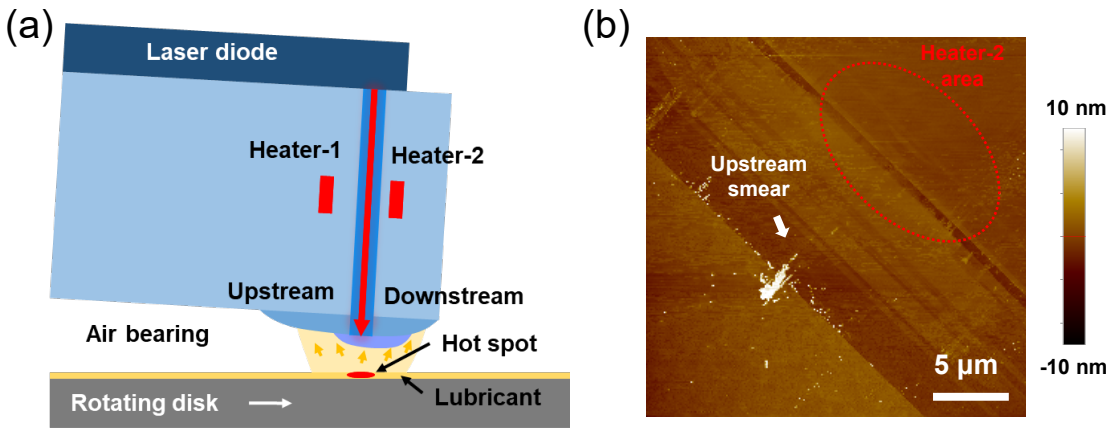

Figure 4.12: (a) A schematic diagram (not to scale) showing the dual heaters. (b) An AFM image of the smear after mitigation using the heater-2.

4.4.2 Thermal approach

Section 4.3 demonstrates that the smear forms when the lubricant evaporation occurs for a certain time, which is long enough for the lubricant evaporation to reach the head surface and condense. The lubricant condensation on the head surface is due to the fact that the disk temperature is higher than the head temperature [36, 102]. If the head temperature is higher than the disk temperature, the smear on the head should be transferred back to the disk driven by the temperature difference, which is the proposed thermal approach for the smear mitigation.

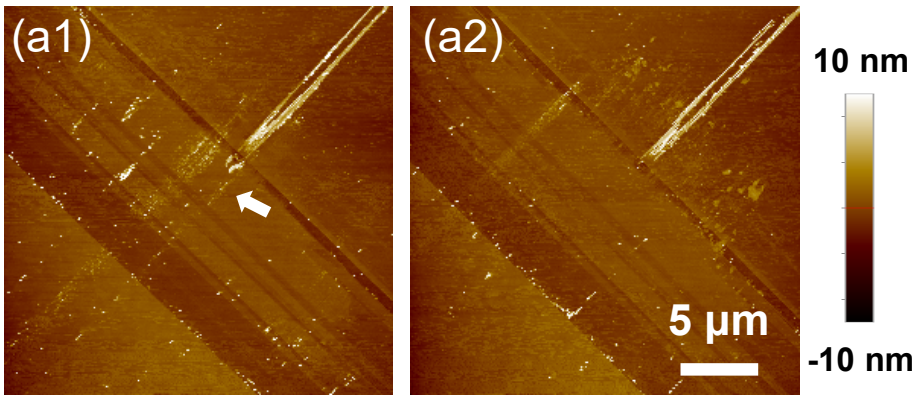

Figure 4.13: AFM images of the smear on the head surface after mitigation at the heater power of TDP−80 mW and the laser current of (a1) 0 mA (a2) 10 mA for 40 min.

The smear was first generated on the head surface at the heater power of TDP−80 mW, the disk temperature of 367.0 °C and the laser exposure time of 111.1 s, the same as the smear generation step in the mechanical approach presented previously. Then, the heater power was maintained unchanged to avoid any mechanical burnishing, and the laser current was controlled at 0 mA or 10 mA. Both of the two laser currents were below the laser diode's threshold 13.0 mA, so no laser came out, and thus the disk surface was not heated at all. In this way, the head temperature ($\sim$ 40 °C rise due to the heater and $\sim$ 5 °C rise due to the 10 mA laser current) was higher than the disk temperature (room temperature). Figure 4.13 shows the AFM images of the smear mitigation using this thermal approach for 40 min. Figure 4.13(a1-a2) show less smear on the upstream surface, which is where the heater is embedded beneath, than the surface after the smear generation as shown in Figure 4.9(a0). Also, the smear appears in the form of discrete particles instead of long traces after the thermal mitigation, which is because the long-term heating slowly makes the smear evaporate and brings the smear away from the head surface, leaving small particles behind. The remaining particles may be metals from the magnetic layer in the disk. Figure 4.13(a2) has a cleaner upstream surface than Figure 4.13(a1), indicating that the larger temperature difference induced by 10 mA laser current helps mitigate the smear.

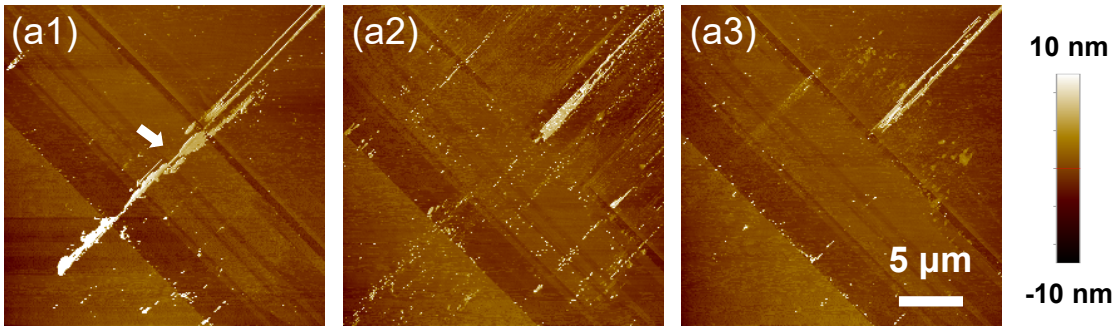

Figure 4.14: AFM images of the smear after mitigation at the heater power of TDP−80 mW and the laser current of 10 mA for (a1) 10 min (a2) 20 min (a3) 40 min.

Next we investigate the effect of duration in this thermal mitigation strategy. Figure 4.14 shows the AFM images of the smear mitigation at the heater power of TDP−80 mW and the laser current of 10 mA for (a1) 10 min (a2) 20 min (a3) 40 min. Figure 4.14(a1) has a similar head surface to the one before mitigation where the smear appears as traces. At the duration of 20 min, it is found that the upstream smear is spread out from traces to discrete dots, which is due to the slow heating and evaporation process. When the duration is 40 min, many dots disappear on the upstream surface, and thus the smear is mitigated after such a long duration. However, the downstream smear remains due to absence of any heating there.

Previously, the laser has always been energized in the continuous wave (CW) mode.

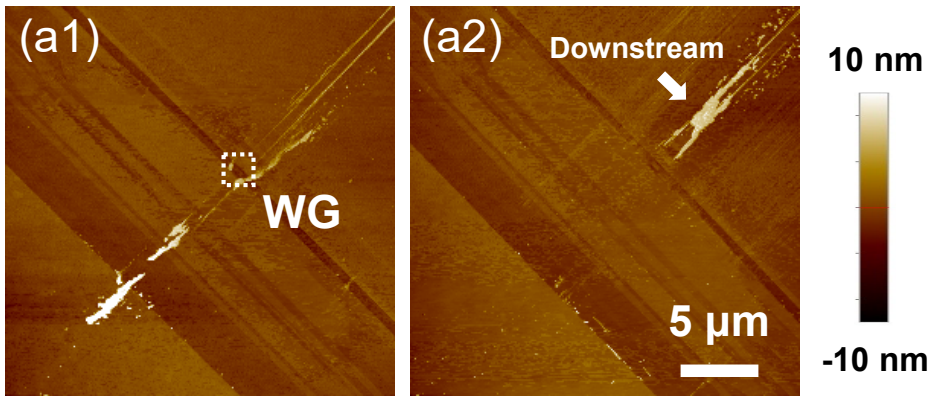

Figure 4.15: AFM images of the smear generated at the heater power of TDP−80 mW and the pulsed 34.5 mA laser current of (a1) 1 kHz and (a2) 10 kHz (duty cycle: 50%) for a total exposure time of 111.1 s.

Here, a pulsed laser was used to investigate if a high frequency laser implementation could mitigate the smear better than the CW laser does. Figure 4.15 show the AFM images of the smear generated at the heater power of TDP−80 mW and the pulsed 34.5 mA laser current of (a1) 1 kHz and (a2) 10 kHz (duty cycle: 50%) for a total exposure time of 111.1 s. The comparison between Figure 4.15(a1) and Figure 4.15(a2) shows that higher frequency laser results in a smaller amount of smear generated upstream. A possible explanation is as follows. Section 4.3 shows that the smear forms upstream when the smear at the WG location grows and fills the head-disk spacing, and then the mechanical interaction between the smear already on the head and the disk surface drives the lubricant evaporation to the upstream areas. This process takes time, so shorter laser pulse (higher frequency laser) may not be enough for the smear to fill the spacing and to form upstream. It is worth noting that the laser in the actual HAMR writing has a nanosecond timescale [4], much shorter than the laser pulse used in Figure 4.15(a2). Hence, the upstream smear should not be an issue in the actual HAMR operations. Moreover, both cases in Figure 4.15 show the appearance of the downstream smear, which is also likely to occur in the actual HAMR case but can be mitigated via the mechanical approach using the heater-2 in the head as proposed in Subsection 4.4.1. This can serve as a head cleaning scheme for smear management in the actual HAMR operations.

4.5 Conclusion

We performed experiments to investigate the smear formation and analyzed its formation mechanism. The experimental results show that the smear begins to form when the disk temperature is higher than the lubricant evaporation temperature, and the evaporation occurs for a certain time, which is long enough for the lubricant evaporation to reach the head surface and condense. The smear originates from the WG location and forms into traces along the down-track direction. The smear traces are primarily located at a distance from the track center, which is likely due to the thermocapillary stress. Particulate-like smear that comes from the magnetic layer appears at a higher disk temperature. And the smear amount increases with the disk temperature and the laser exposure time.

Furthermore, two smear mitigation strategies were proposed: a mechanical approach and a thermal approach. In the mechanical approach, the head surface can be brought closer to the moving disk surface by use of the dual heaters, and the smear on the head surface can be burnished away by the frictional interactions from the head-disk contact without damaging the head. Meanwhile, the burnishing away of the smear was detected by the AE sensor, and this led to more thermal transport at the head-disk interface, thereby lowering the head temperature by $\sim$ 2 °C. Specifically, the upstream/downstream smear can be removed by the heater-1/heater-2 respectively due to their distinct locations. This mechanical burnishing method only takes several revolutions to accomplish, so it can be implemented as a practical application in the HAMR hard disk drive technology. In the thermal approach, the head temperature was controlled higher than the disk temperature,

which is opposite to the circumstance of HAMR writing operations. It is discovered that larger temperature difference between the head and the disk helps mitigate the smear, and that the smear is spread out from traces to dots and is mitigated after a long duration $\sim$ 40 min. Additionally, it is found that a pulsed laser operating at a higher frequency can generate a smaller amount of upstream smear while the downstream smear can be mitigated using the heater-2.

This chapter reveals the mechanism of the smear formation in HAMR and presents two mitigation strategies for the smear mitigation without damaging the head. It is envisioned that the insights obtained from this smear study will be important to the HAMR hard disk drive's performance and reliability.

This chapter includes work published in *Tribology International* in 2021 (reproduced from [106], with the permission from Elsevier).

Chapter 5

Thermal mapping using a phase change material

5.1 Introduction

The microelectronics industry is pushing the fundamental limit on the physical size of individual components to produce faster and more powerful integrated devices [107–111]. These devices have nanoscale features that dissipate power resulting in nanoscale hot spots that may lead to device failures. To understand the heat dissipation process and the reliability impact of the hot spots during the device operation, the development of a versatile high-resolution thermometry technique, which is capable of reliably mapping the areal temperature of various components integrated in the device ranging from nanometer to micrometer dimensions, is required [112, 113]. Various thermometers were developed to achieve this goal such as radiation thermometry, thermocouple based contact thermometry, scanning thermal microscopy (SThM), scanning transmission electron microscopy (STEM) and transition based threshold thermometers [113–127], which can be broadly classified into two categories: non-contact and contact based thermometers. However, most of these techniques have limitations including the need for extensive calibration, perturbation of the actual device temperature, low throughput, and the use of ultra-high vacuum. Techniques such as Raman [120], fluorescence [128], luminescence [129] and transmission electron microscopy [127, 130, 131] are non-contact thermometers, with their areal resolutions limited either by the optical diffraction limit [132] or by the use of specific metals and semiconductors [127]. SThM is an extensively used contact thermometer, but it typically suffers from contact-related artifacts that lead to an under prediction of the device temperature. This is due to the thermal coupling strength between the device and the SThM tip, which is material dependent and difficult to measure [122, 133].

Here a novel facile technique, which uses a phase change material $Ge_2Sb_2Te_5$ to map the temperature of an operational microelectronic device from nanoscale to microscale, is presented. It requires minimal effort in temperature calibration and the temperature contour

can be mapped using both contact and non-contact modes such as atomic force microscopy (AFM), scanning electron microscopy (SEM) or optical microscopes. We mapped the temperature contours of a nanowire and an embedded micro-heater where the contour areas differ by three orders of magnitude. Section 5.2 introduces the experimental platform of the device. Section 5.3 shows the temperature calibration of the $Ge_2Sb_2Te_5$ phase transition. Section 5.4 demonstrates this thermal mapping technique from nanoscale to microscale. Section 5.5 concludes this chapter.

This work was completed jointly with Sukumar Rajauria, Erhard Schreck, Robert Smith, Na Wang, Jim Reiner and Qing Dai. Sukumar Rajauria and Erhard Schreck conceived the project. Sukumar Rajauria and I designed and implemented the experimental setup with the help of Na Wang. Robert Smith performed the thermal simulations. Jim Reiner deposited the phase change material. I performed and analyzed the experiments under the supervision of Sukumar Rajauria, Erhard Schreck and Qing Dai.

5.2 Experimental platform

To demonstrate the versatility and practicality of this thermal mapping technique, a recording head from a commercial hard disk drive was used. The head of the hard disk drive provides a unique platform for such studies as it has several embedded heat sources, which differ in heated area by three orders of magnitude [25, 134]. At the microscale, it has a micro-heater, which is used to adjust the clearance between the head and the rotating disk [97]. The micro-heater is embedded a few micrometers from the surface as shown in Figure 5.1(a), and it produces a microscale temperature contour. At the nanoscale, it has a nano-heater, which is used both as a heater and a thermometer. The nano-heater consists of a 200 nm wide, 1 μm long, and 20 nm thick metal wire that is embedded 2 nm from the surface as shown in Figure 5.1(b). Figure 5.1(c-d) show the simulated surface temperature contours and profiles for the micro-heater and the nano-heater. In comparison to the micro-heater's temperature field, the nano-heater's areal temperature map is three orders of magnitude smaller (see Figure 5.1(d)). It is noted that the nano-heater has a temperature coefficient of resistance (TCR) of 0.003/K, which was used to measure the average surface temperature. In this chapter, it is quantitatively demonstrated that the temperature measured from the phase change temperature contour (PCTC) technique agrees well with the measured average surface temperature and the thermal simulations for both the micro-heater and the nano-heater.

The microelectronic device was held on a metal fixture with electrical pins. The components inside the device such as the heaters were powered by Keithley 2602 SYSTEM SourceMeter, which was controlled by a Python script. A 22 nm thin film of $Ge_2Sb_2Te_5$ was sputtered on the surface of the device. The amorphous $Ge_2Sb_2Te_5$ is a chalcogenide phase change material that crystallizes to face-centered cubic (FCC) at T_g between 130 °C and 160 °C, which depends on the material composition and the heating condition [135, 136] and thus needs to be calibrated. This crystallization is accompanied with large changes in its

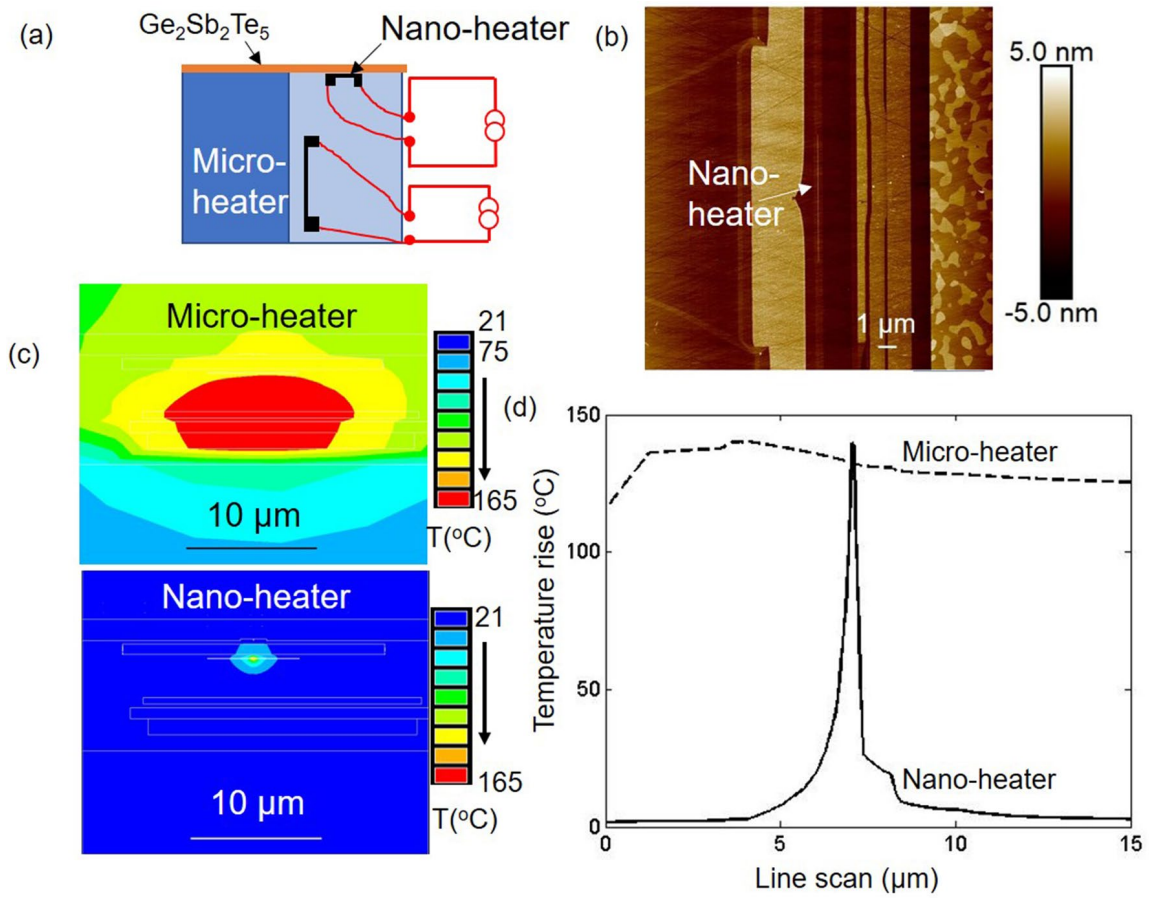

Figure 5.1: Heat sources in the device. (a) A cross-sectional diagram of the device showing the embedded heat sources: a nano-heater and a micro-heater. (b) An AFM image of the device surface: the micro-heater is embedded and cannot be seen from the surface, while the nano-heater (1 μm $\times$ 20 nm) is located at the center. (c, d) Simulation: temperature maps and profiles of the nano-heater and the micro-heater with similar peak surface temperatures.

electric conductivity, optical reflectivity and density [135, 137–140]. The density increases after the crystallization to FCC. Hence, the thickness of the $Ge_2Sb_2Te_5$ thin film reduces where the temperature is higher than T_g, as shown in Figure 5.2. The topography change or the reflectivity change of the thin film due to the phase transition were measured by Digital Instruments Dimension 3100 AFM or an optical microscope respectively.

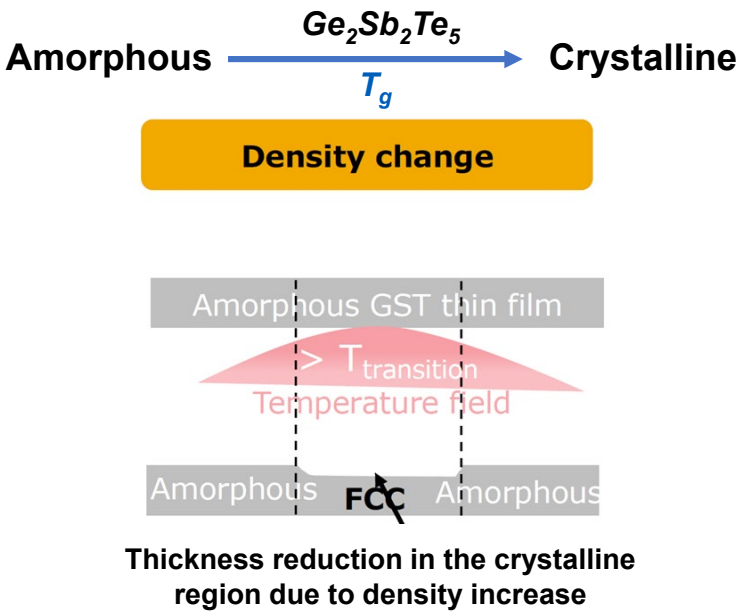

Figure 5.2: A diagram of the phase transition in the $Ge_2Sb_2Te_5$ thin film.

5.3 $Ge_2Sb_2Te_5$ transition temperature calibration

Precise and relatively simple temperature calibration is a key advantage of the PCTC method compared to other techniques that require extensive temperature calibration. To calibrate the crystallization temperature T_g of the phase change material $Ge_2Sb_2Te_5$, we relied on the pronounced structural property change at the phase change condition as shown in Figure 5.2. The rate of this transformation from an amorphous state to the crystalline rock salt structure is well characterized by an activation energy of about 2.6 eV [135, 138]. Due to this activation energy driven process, the crystallization temperature is dependent on the dwell time of the sample. For this reason, the dwell time at a constant power condition was fixed at 5 min, which is much longer than the response time of the two heat sources [141]. The calibration sample, a photo-lithography defined 22 nm thick $Ge_2Sb_2Te_5$ layer on top of a silicon wafer, was heated in a customized copper chamber, where the temperature was measured by a type-K thermocouple (Figure 5.3(a)). The dwell time at a constant chamber temperature was 5 min after which the sample was allowed to cool down to room temperature, and the film thickness was measured using the AFM with vertical resolution of 0.05 nm. Figure 5.3(b) shows the $Ge_2Sb_2Te_5$ film thickness as a function of the chamber temperature. At $T_g = 149$ °C, the film thickness reduces, indicating a phase transition from the amorphous state to the crystalline state, as confirmed by the electron diffraction patterns shown in Figure 5.4.

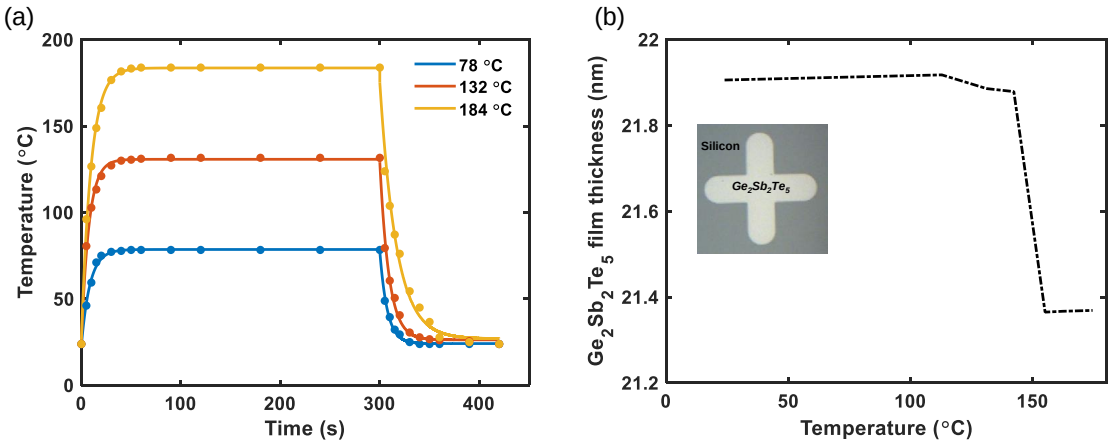

Figure 5.3: (a) The chamber temperature during the heat treatment process. (b) The $Ge_2Sb_2Te_5$ thin film thickness as a function of the chamber temperature. The glass transition temperature T_g is 149 °C. Inset: an optical micrograph of the calibration sample.

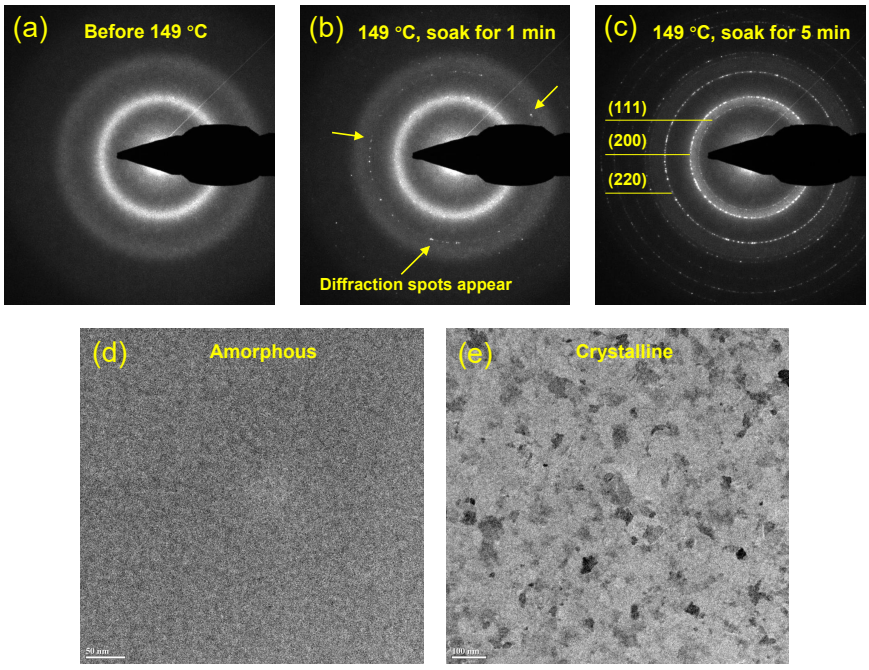

Figure 5.4: (a-c) The electron diffraction patterns of $Ge_2Sb_2Te_5$ before the transition temperature and soak at the transition temperature (1 min/5 min). (d-e) Transmission electron microscopy (TEM) images of $Ge_2Sb_2Te_5$ before and after the phase transition.

Before the glass transition temperature T_g, Figure 5.4(a) shows that the material was amorphous. Then the sample was soaked at T_g for 1 min as Figure 5.4(b), some diffraction spots appeared, indicating that the phase transition began. After soaking for 5 min, several orientations of the crystalline formed clearly. Meanwhile, Figure 5.4(d-e) are the transmission electron microscopy (TEM) images before/after the phase transition. It is obvious that $Ge_2Sb_2Te_5$ underwent the phase transition from amorphous to crystalline.

5.4 Thermal mapping

5.4.1 Nanoscale thermal mapping

To demonstrate the thermal mapping technique, we first characterized the joule heating of the nano-heater inside the head of the hard disk drives. The head surface was coated with a 22 nm thick layer of $Ge_2Sb_2Te_5$ thin film. The nano-heater was biased using a current source, across which the measured voltage drop was used to estimate the resistance increase of the nano-heater due to the dissipated joule heat (Figure 5.5(a)).

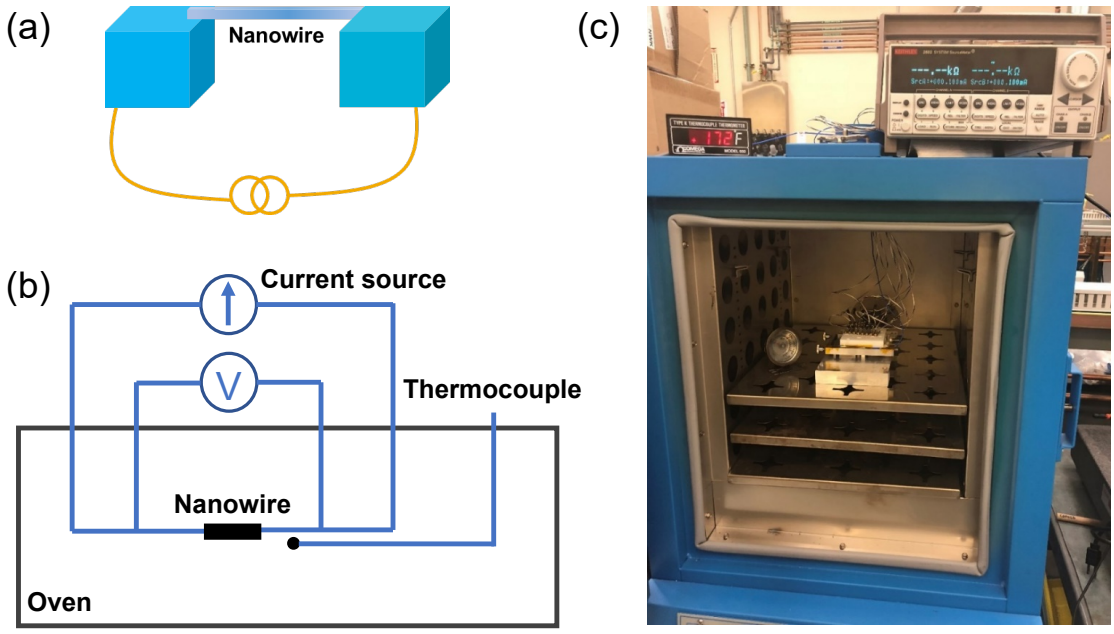

Figure 5.5: (a) A schematic diagram of the nano-heater. The nano-heater with dimension 1 μm $\times$ 20 nm $\times$ 200 nm is electrically connected to two pads within the device. (b) 4-probe measurement for the nanowire TCR. (c) An overview picture of the setup.

The resistance change of the nano-heater was used to estimate the average increase of the device temperature by $R_T = R_0(1+\alpha\Delta T)$, where R_0 is the room-temperature resistance

at a low current bias where no significant self-heating occurs, R_T is the resistance at the same bias corresponding to the temperature T, α is the temperature coefficient of resistance (TCR), and ΔT is the average temperature rise due to the joule heating. The temperature coefficient of resistance (α) 0.003/K was determined separately in an isothermal Cascade Tek Oven using a 4-probe measurement scheme as shown in Figure 5.5(b-c). The current source was at a low bias of 0.1 mA such that the self-heating of the nanowire could be ignored (about 0.1 °C increase). The oven temperature rose from room temperature to around 115 °C in steps. For each temperature, the resistance and the oven temperature were recorded when steady. All the samples show the same TCR of 0.003/K. Therefore, the nanowire, with known TCR, can be used as a thermometer too.

Since the device surface was coated with the $Ge_2Sb_2Te_5$ thin film, its effect on the thermal transport of the system needs to be clarified, which turns out to negligible. Figure 5.6 shows the measured average temperature rise of the nanowire as a function of its power before and after $Ge_2Sb_2Te_5$ coating. Both two samples show that the $Ge_2Sb_2Te_5$ coating has almost no effect on the thermal transport ($\sim$ 0.2 °C difference, which is negligible).

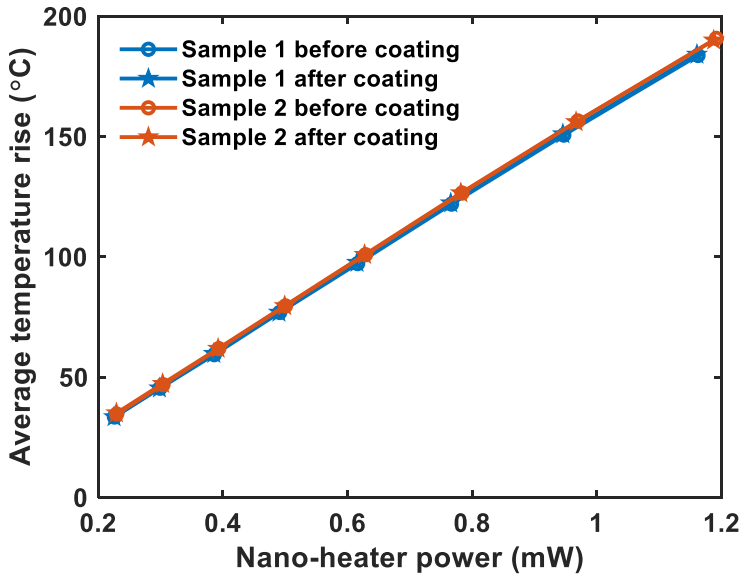

Figure 5.6: The average temperature rise as a function of the nano-heater power before/after $Ge_2Sb_2Te_5$ coating .

Exposed to the temperature field by the nano-heater, the $Ge_2Sb_2Te_5$ phase transition took place along with the density increase and volume reduction, where AFM topography measurement shows as a reduction in the film height. Figure 5.7 shows the AFM topography micrographs corresponding to different powers in the nano-heater. For nano-heater power smaller than 0.60 mW, the AFM shows no change in the topography of the $Ge_2Sb_2Te_5$ film over the nano-heater, indicating that the surface temperature is lower than the crys-

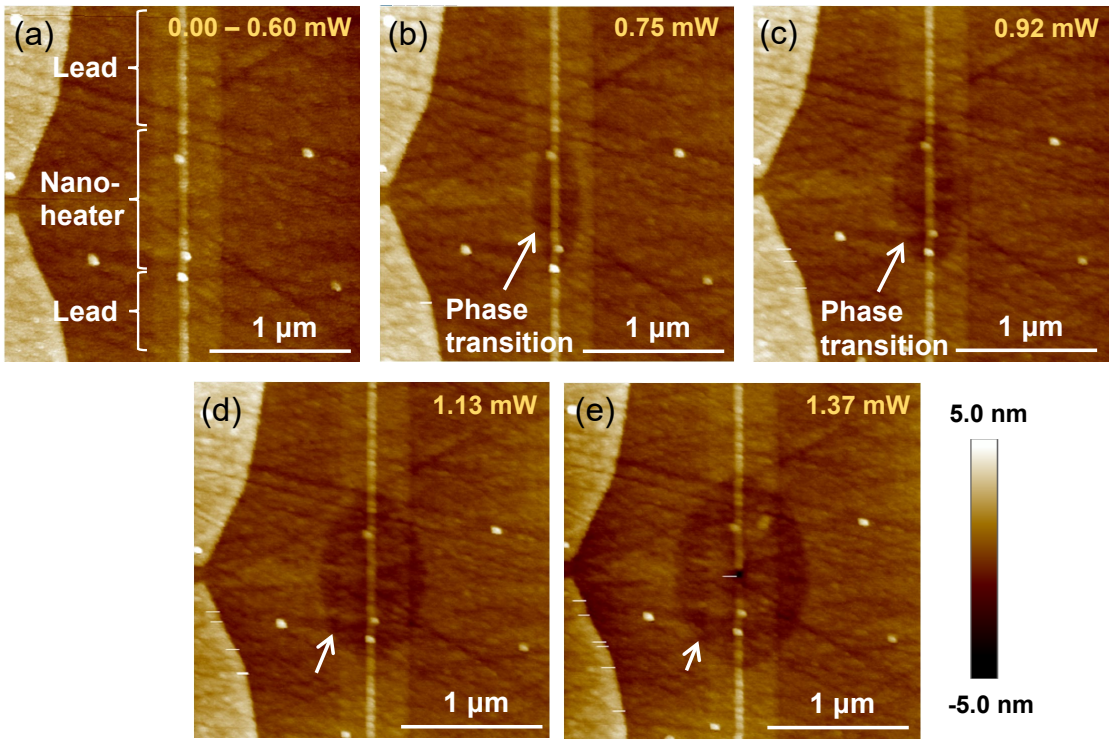

Figure 5.7: AFM images of the device at different nano-heater powers: (a) original surface; (b–e) the depression in the topography from the phase transition around the nano-heater.

tallization temperature T_g. When the nano-heater power is 0.75 mW, a small depression in the topography is observed centered at the hot spot of the nano-heater as shown in Figure 5.7(b). A further increase in the nano-heater power leads to a gradual increase in the area undergoing the crystallization, which is indicated by the lateral growth of the depressed area in the AFM images. Note that the boundary of the topography depression corresponds to the isotherm of the crystallization temperature T_g. Furthermore, we use the transition boundary measured at different nano-heater powers to map the temperature of the device. The rate of the $Ge_2Sb_2Te_5$ phase transition is a function of both the temperature and time. Here, the power in the nano-heater was increased incrementally with a fixed dwell time of 5 min. The last transition boundary corresponds to the calibration temperature T_g at the largest heater power $P_o = 1.37$ mW (Figure 5.7(e)). Assuming that the temperature is a linear function of the applied power, the temperature isotherm T_i at each previous transition boundary (Figure 5.7(b-d)) is given by:

$$T_i = T_g \frac{P_o}{P_i} \tag{5.1}$$

where T_g is the calibrated $Ge_2Sb_2Te_5$ crystalline transition temperature for the dwell time of

5 min, P_o is the nano-heater power at which the final transition boundary is measured, and P_i is the previous power with $P_i < P_o$ in the nano-heater. Figure 5.8 shows the constructed temperature map of the device along with the simulation result for $P_o = 1.37$ mW, with a good agreement between them. The nano-heater thermal simulation was modeled using a finite element model in ANSYS Workbench Thermo-electric module version 17.2.

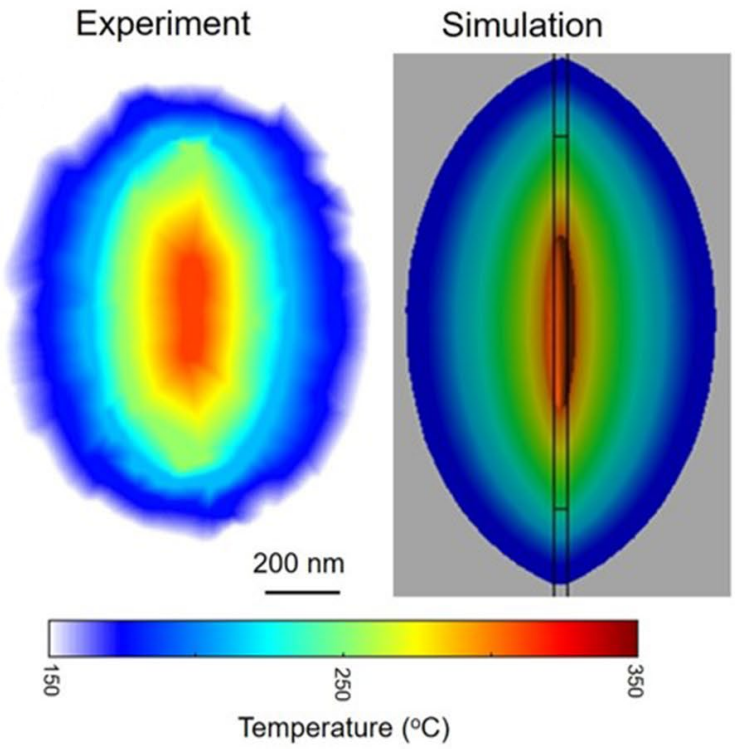

Figure 5.8: The constructed temperature contour from the PCTC technique and the simulation for the nano-heater power of 1.37 mW.

Figure 5.9(a) shows the phase transition area calculated from the topography depression in the AFM image as a function of the power dissipated in the nano-heater. When the nano-heater power is lower than 0.60 mW, the transition area is zero, signifying that the surface temperature is lower than the glass transition temperature T_g everywhere. At higher powers the transition area grows linearly with the dissipated power in the nano-heater. The simulation results are shown as the red dashed line, which agrees reasonably well with the evolution of the transition area. Both the experiment and the simulation show a sharp increase in the phase transition area beyond 0.60 mW. At much larger nano-heater powers, the poor match is because of our inability to capture the exact structural details in the simulation such as the actual thermal boundary conditions and the various material parameters. To further confirm the surface temperature, we simultaneously measured the resistance of the nano-heater and used its TCR $\alpha = 0.003$/K to estimate its average temperature. Figure 5.9(b) shows the

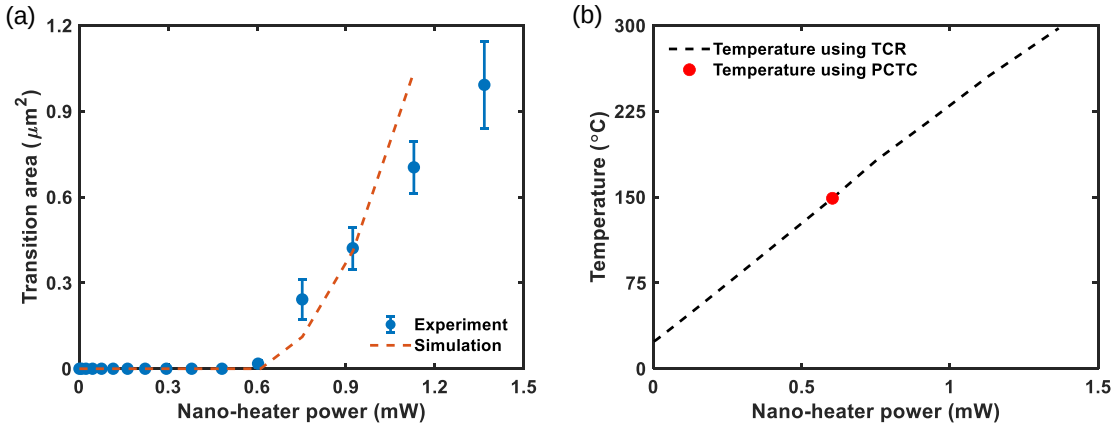

Figure 5.9: (a) The measured phase transition area as a function of the dissipation power in the nano-heater power. The red dashed line corresponds to the simulation of the T_g isotherm contour. (b) The black dashed line shows the estimated average surface temperature along the nano-heater from its resistance change and the measured isotherm from the PCTC technique (red dot). Estimated error bar in the average surface temperature measurement is 0.04 °C.

measured surface temperature of the nano-heater as a function of the power dissipated. The red dot is the temperature from the PCTC technique at 0.60 mW derived from the x-axis intercept of Figure 5.9(a). As expected, the temperature from the PCTC technique matches the temperature reading given by the resistance change. The excellent agreement between the temperature measured using the PCTC and TCR technique along with the simulation demonstrates that the PCTC technique can precisely map the high operational temperature of the nanoscale heater embedded in the device.

The uncertainty in the temperature derived from this PCTC technique is primarily due to the fact that the crystallization rate of the phase change material $Ge_2Sb_2Te_5$ does not have a large abrupt jump at a single temperature (as in a first order phase transition). Hence, the full temperature history of the sample, not just the last power used, can influence the size of the observed contour. The activation energy E_A required to undergo the structural change from amorphous to FCC structure is around 2.6 eV [135, 138]. When temperature T is below the glass transition temperature T_g, there is still a small portion of the material that transits to FCC. The proportion can be expressed as

$$P_i = e^{-\frac{E_A}{k_B}(\frac{1}{T_i}-\frac{1}{T_g})} \tag{5.2}$$

where P_i refers to the proportion of transition at the temperature T_i and k_B is Boltzmann constant. Therefore, when we heat the same material in multiple heating cycles (N cycles),

the total proportion of transition P is the sum of all the previous heating cycles:

$$P = \sum_{i=1}^{i=N} P_{\mathrm{i}} \tag{5.3}$$

Figure 5.10 plots the modelling result of the transition proportion of $Ge_2Sb_2Te_5$ under a single heating and an accumulating heating. In the single heating, 100% of the material transits at 149 °C. However, as for the accumulating heating, all the heating cycles have contributions to the phase change although below the transition temperature T_g. For the nano-heater, the step of the temperature increase was kept at 10 °C, so finally the measured transition temperature corresponding to 100% transition was about 2 °C below the actual value, which is acceptable.

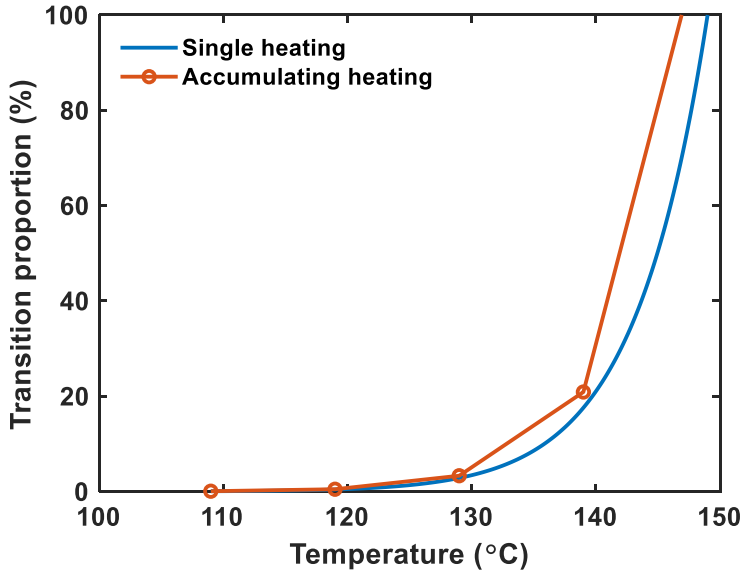

Figure 5.10: The transition proportion of the $Ge_2Sb_2Te_5$ under a single heating and an accumulating heating.

Next we study the time response of the $Ge_2Sb_2Te_5$ film to construct a transient temperature map of the device at a constant nano-heater power. The growth of the transition boundary was tracked over time. It is noted that the transient response of the nano-heater is six orders of magnitude faster than the $Ge_2Sb_2Te_5$ phase change. Assuming that the phase change conversion follows an Arrhenius model and the conversion is linear with time, the temperature for each transition boundary is derived by monitoring the time needed for each transition boundary to develop. The temperature T_{i} at time t_{i} is given by:

$$T_{\mathrm{i}}(t_{\mathrm{i}}) = \left[-\frac{k_{\mathrm{B}}}{E_{\mathrm{A}}} \left(\ln \frac{1}{t_{\mathrm{i}}} - \ln \frac{1}{t_{\mathrm{cal}}} \right) + \frac{1}{T_{\mathrm{g}}(t_{\mathrm{cal}})} \right]^{-1} \tag{5.4}$$

where k_B is Boltzmann constant, $E_A \sim 2.6$ eV is the activation energy of the $Ge_2Sb_2Te_5$ transition, $T_g \sim 149$ °C is the calibrated crystallization temperature at the dwell time $t_{cal} = 5$ min. It is worth noting that the temperatures of isotherms corresponding to shorter dwell times ($t_i < t_{cal}$) are higher than T_g.

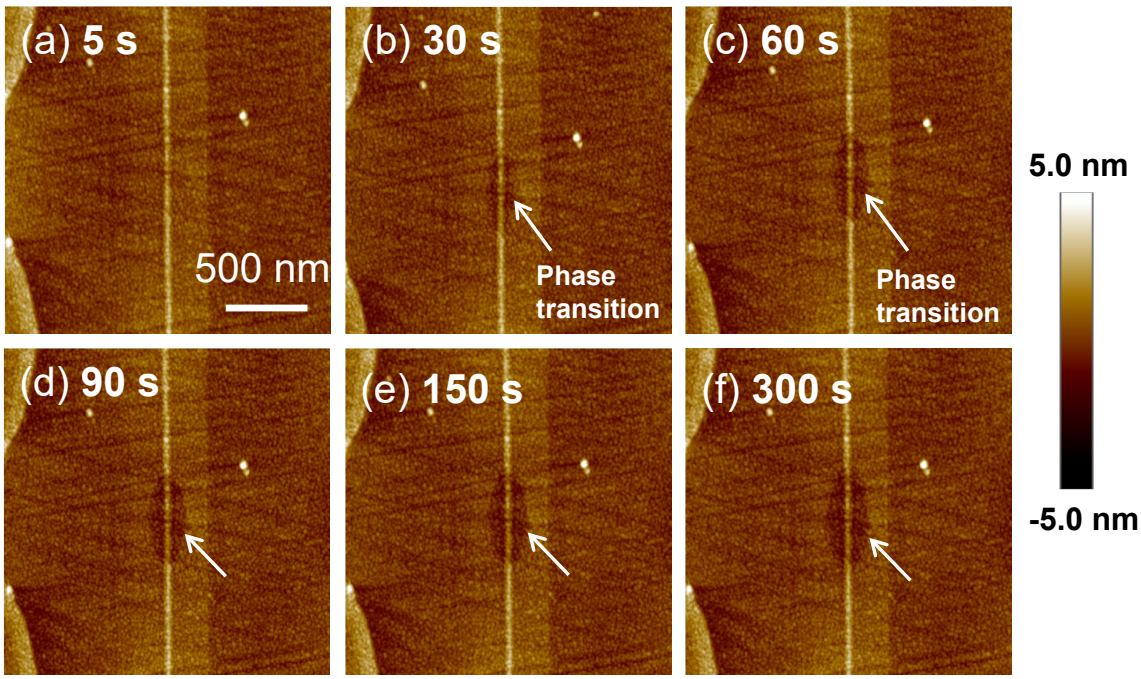

Figure 5.11: Transient response of $Ge_2Sb_2Te_5$ at a constant nano-heater power of 0.68 mW. The depression around the nano-heater denotes the phase transition.

Figure 5.11 shows the AFM images of the phase transition area around the nano-heater as a function of the accumulated time for a constant power of 0.68 mW. The phase transition area has a shape of a perfect ellipse and expands over time. The long and short axes were measured to calculate the area of the transition. Figure 5.12 shows the result of transition area with the accumulative time and the corresponding exponential fit with a time constant of 37.6 s. The transition temperature at different accumulated heating time was determined by using Eq. 5.4. Figure 5.13(a) shows the constructed temperature map of the device at the constant nano-heater power of 0.68 mW. In comparison to Figure 5.8, the temperature map is smaller and more elliptical since the nano-heater power is almost 50% smaller. Figure 5.13(b) shows the temperature across nano-heater as a function of distance demonstrating the high resolution of the PCTC scheme. The continuous nature of our thin film allows for a higher spatial resolution, which is limited only by the grain size of $Ge_2Sb_2Te_5$ (sub 20 nm) and the resolution of the imaging technique (< 10 nm) [119].

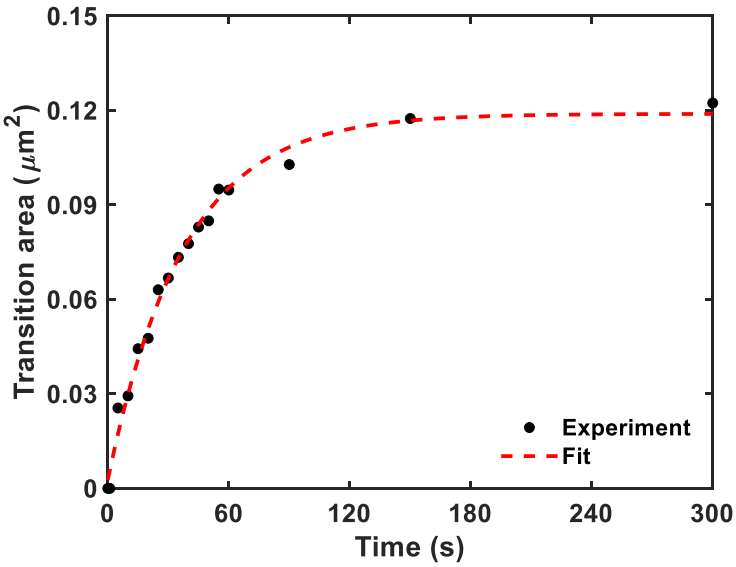

Figure 5.12: The $Ge_2Sb_2Te_5$ transition area with the accumulated time at the nano-heater power of 0.68 mW.

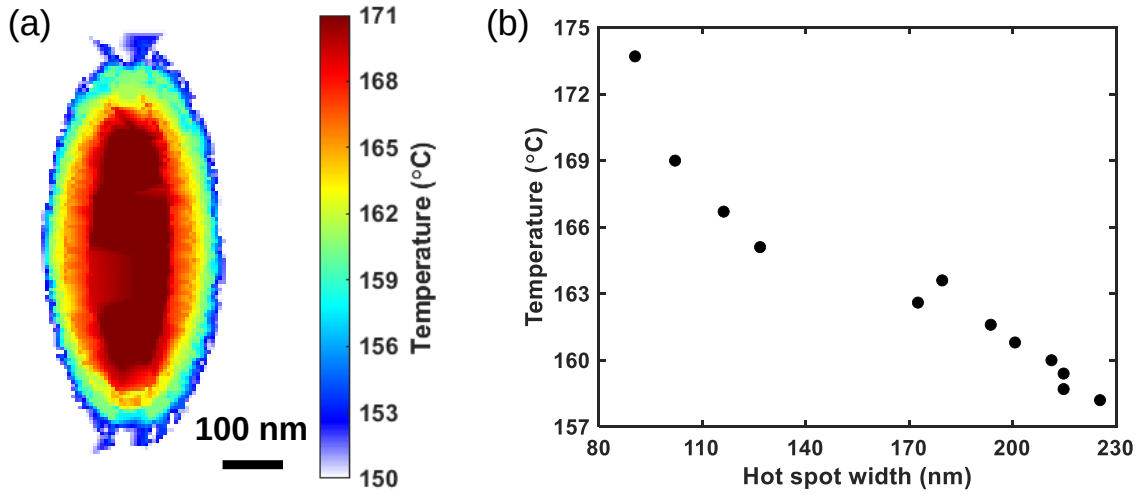

Figure 5.13: (a) The transient temperature map at the nano-heater power of 0.68 mW. (b) The temperature as a function of the hot spot width across the nano-heater.

5.4.2 Microscale thermal mapping

To demonstrate the versatility of the PCTC technique, we also characterized the joule heating of a much larger micro-heater embedded in the head of the hard disk drive. The temperature contour of the micro-heater is three orders of magnitude larger than that of the nano-heater embedded in the same device (as shown in Figure 5.1) in terms of the contour area. The micro-heater was biased continuously using a current source, and the measured voltage drop across the nano-heater (thermometer) was used to estimate the dissipated joule heat. The dwell time of 5 min at a constant micro-heater power is much longer than the thermal response time of the heater and the phase transition time beyond which the physical, optical and electrical properties change. The temperature contour of the micro-heater was mapped using an optical microscope by simply imaging the reflectivity change in the transition area as shown in Figure 5.14.

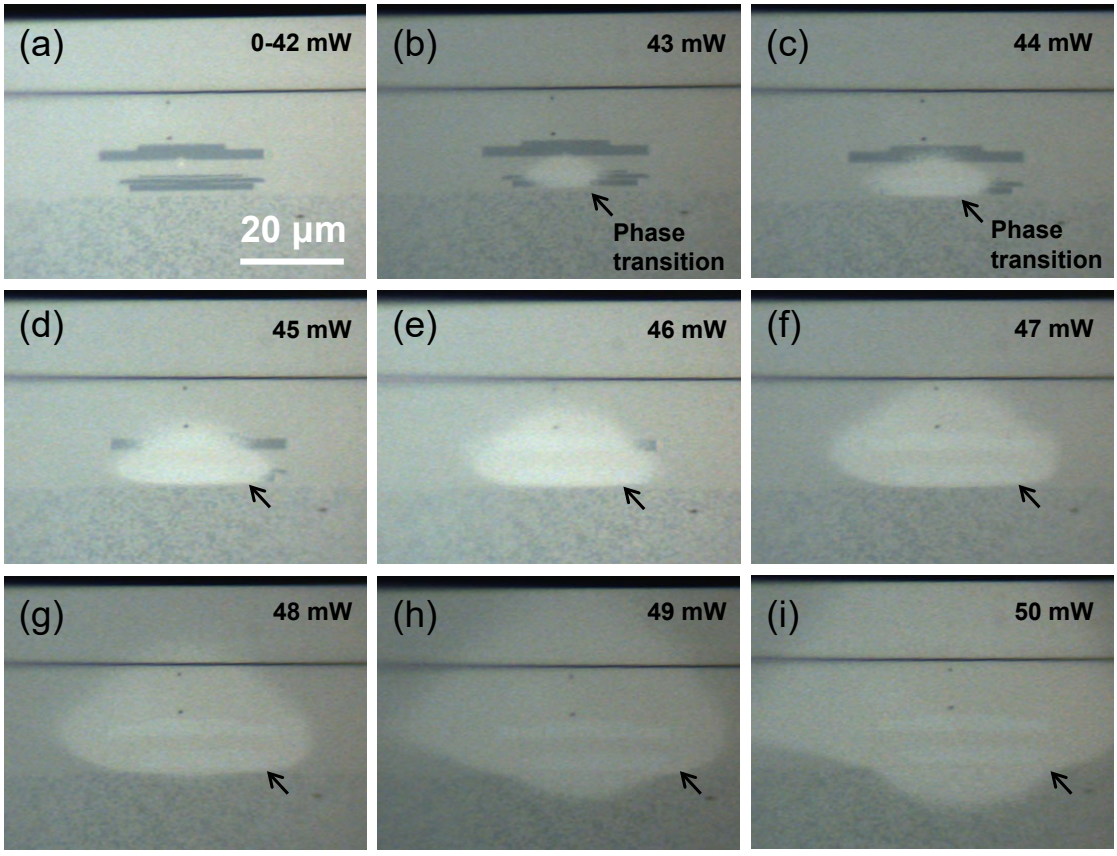

Figure 5.14: Optical micrographs of the device at different micro-heater powers (continuous single heating): (a) original surface; (b–i) The reflectivity increase at the center of the micrographs corresponding to the phase transition due to the temperature rise of the micro-heater.

Figure 5.14 shows the optical micrographs at different micro-heater powers (0–50 mW). No change in reflectivity was observed below the dissipated power of 42 mW in the micro-heater. At the power of 43 mW, an increase in the reflectivity was observed at the center of the thermal hot spot due to the micro-heater. Note that the boundary of the transition area corresponds to the crystallization temperature T_g. In comparison to the nano-heater, here the micro-heater requires 60 times more power to achieve the same surface temperature since the micro-heater is embedded deeper and heats up a much larger volume. At higher micro-heater powers, the growth in the transition area indicates an increase in the thermal spot size with the same crystallization temperature T_g isotherm. Figure 5.15 shows the constructed temperature map of the device using Eq. 5.1 along with the simulation, which was performed using finite element models in ANSYS Mechanical APDL version 17.2. The dimensions and the overall shape of the transition contour from the experiments match well with the simulated T_g isotherms.

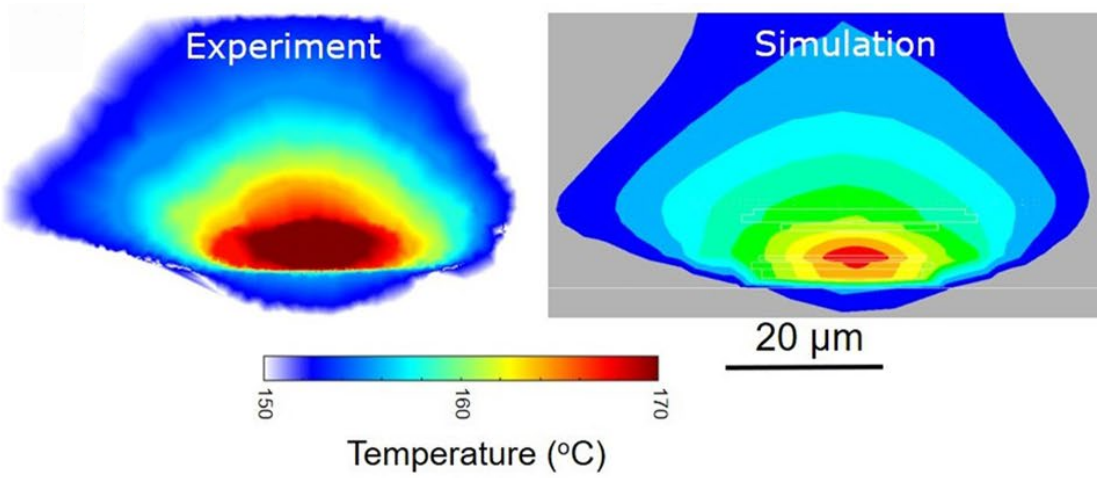

Figure 5.15: The constructed temperature map of the device along with the simulation at the micro-heater power of 50 mW.

Furthermore, we utilized the nano-heater as a thermometer by monitoring its resistance change at a very low current of 0.1 mA, in order to avoid self-heating, to measure the temperature rise due to the micro-heater. Figure 5.16 shows the surface temperature measured by the nano-heater as a function of the power dissipated in the micro-heater. The red line shows the micro-heater power of 43 mW beyond which the phase transition was observed in the optical micrographs. The expected rise of the surface temperature due to the micro-heater is 2.9 °C/mW, as derived from both the PCTC thermometry and the nano-heater's resistance change (TCR thermometry). This shows an excellent agreement between the PCTC technique, the measured surface temperature and the simulation for the temperature map of the micro-heater.

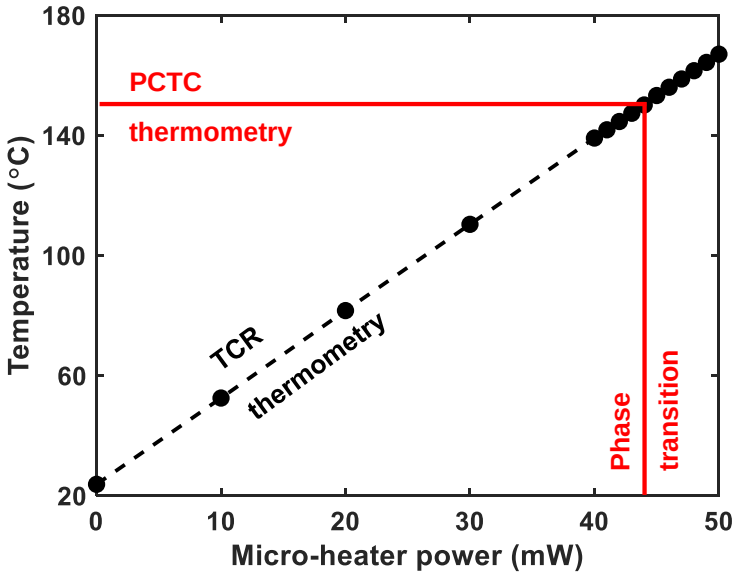

Figure 5.16: The surface temperature measured by the nano-heater (black dashed line), acting as a thermometer, along with the measured transition temperature (red line at 149 °C and 43 mW) using the PCTC thermometry from the optical micrographs. Estimated error bar in the surface temperature measurement is 0.04 °C.

5.5 Conclusion

In this chapter, we presented a facile phase change temperature contour (PCTC) technique, which uses a thin film contact thermometer based on the phase change material $Ge_2Sb_2Te_5$, to precisely map thermal contours from nanoscale to microscale. $Ge_2Sb_2Te_5$ undergoes a crystalline transition at T_g with large changes in its electric conductivity, optical reflectivity and density. Using this approach, we mapped the surface temperature of the nanowire and the embedded micro-heater in the same device where the scales of the temperature contours differ by three orders of magnitude. The spatial resolution can be as high as 20 nm thanks to the continuous nature of the thin film. This technique is extremely versatile and does not require the use of expensive microscopes like STEM. At the microscale, even an inexpensive optical microscope can be used to map the temperature of the hot spots or heat sources in operating microelectronics devices.

The limitations of the presented PCTC technique are discussed here. Although the technique is versatile and can be used for nanoscale to microscale spatial heat sources with minimal calibration challenges, it has two main limitations. On one hand, the areal contour represents the isotherm at T_g, and to extract the temperature gradient one needs to perform mapping for at least two different power levels or track the phase change with time. On the other hand, the technique is limited to a device temperature higher than the crystallization

temperature of the deposited phase change material. In our case, $Ge_2Sb_2Te_5$ crystallizes at the temperature $T_g = 149$ °C for the dwell time of 5 min. Both the heat sources are able to reach temperatures higher than this T_g. For other systems where reaching a similar temperature would be difficult or impossible, the issue could be overcome by choosing a different composition or phase change materials with lower critical temperatures [142–145].

To summarize, we introduced a versatile phase change material based thermal mapping technique for operational microelectronic devices that can spatially resolve temperature from nanoscale to microscale dimensions. It can be used to characterize surface temperatures with negligible temperature interference due to the deposited thin film and with minimal calibration. A thorough understanding of the heat dissipation in various nanoscale devices, such as the aforementioned nano-heater, may lead to more efficient and powerful integrated devices, and hence holds great economic value to the industry.

This chapter presents work published in *Scientific Reports* in 2020 (reprinted from [146], with a CC BY 4.0 license).

Chapter 6

Lubricant thickness measurement using near-field thermal transport

6.1 Introduction

Near-field thermal transport between two macroscopic bodies separated by a sub-nanometer air gap is of fundamental significance [46–49, 60, 70] and has high economic value for various industrial applications such as near-field thermophotovoltaics [62–64], nanolithography [60, 61] and hard disk drives [4, 5, 33]. Recent studies have shown that the thermal transport across nanoscale gaps exceeds the Planck's blackbody limit by several orders of magnitude [50, 55, 66, 67, 70]. Most of the studies exploring the fundamental thermal transport modes including phonons and photons are conducted using high-vacuum atomic force microscopy (AFM) or custom-fabricated nano-devices [50, 55, 66, 67]. Here, we focus on the head-disk interface in heat assisted magnetic recording (HAMR) hard disk drives, where the recording heads fly at a sub-nanometer spacing from the disk with a relative speed of 5–40 m/s. HAMR uses a laser diode coupled with a near field transducer (NFT) to locally heat the magnetic layer on the disk up to its Curie temperature ($\sim$ 400–500 °C), which is even hotter than the head temperature ($\sim$ 150–250 °C) [4, 34]. Therefore, an in-depth understanding of the thermal transport between the recording head and the disk, which are separated by a sub-nanometer air gap, along with its implications for the associated thin-film components, is critical to the HAMR hard disk drive's performance and reliability.

Another key feature for the long-term reliability of HAMR hard disk drives is the perfluoropolyether (PFPE) lubricant ($\sim$ 1 nm thick) on the disk. The lubricant improves the high-speed tribological performance by passivating the surface against contamination, minimizing friction, and preventing corrosion [4, 13, 14]. To guarantee product longevity, the lubricant must be nonvolatile, and have sufficient mobility to replenish areas where the lubricant has been depleted due to possible high-speed head-disk contact [147]. Moreover, due to the introduction of the laser in HAMR, the hot spot on the disk ($\sim$ 400–500 °C) is well beyond the lubricant evaporation temperature ($\sim$ 150–250 °C) [41, 42], so the lubricant

undergoes evaporation, decomposition and diffusion under thermal exposure [14, 82]. An in-depth understanding of the lubricant depletion under HAMR operating conditions is of great significance to the reliability of the HAMR hard disk drives. On the other hand, the lubricant has a self-healing ability, and it is also important to the reliability. Some of the depleted lubricant recovers gradually due to the lubricant reflow, which has mostly been studied using ex-situ methods [148, 149]. An in-situ measurement of the lubricant reflow is important to the tribological longevity of HAMR hard disk drives.

In this chapter, we propose a near-field thermal transport based scheme for lubricant thickness measurement. We investigate the near-field thermal transport across the head-disk interface in Section 6.2. Particularly, the effect of the lubricant on the thermal transport is studied in Section 6.3, which is then used to determine the lubricant thickness. Section 6.4 presents the quantitative in-situ measurements of the sub-angstrom depletion and reflow dynamics of the lubricant. Section 6.5 concludes this chapter.

This work was completed jointly with Sukumar Rajauria, Erhard Schreck, Robert Smith and Qing Dai. The project was conceived by Sukumar Rajauria, Erhard Schreck and me. Robert Smith provided support on the simulations. I designed the experimental scheme and performed the experiments under the supervision of Sukumar Rajauria, Erhard Schreck and Qing Dai.

6.2 Near-field thermal transport

A HAMR recording head and a HAMR disk were used for such a thermal transport study. The experimental setup is a component-level HAMR test stage, the same as the one in Section 3.2 and Section 4.2, where the head flies over the disk with a closing air gap from 10–15 nm to contact. It is a unique platform in which the head's spacing from the disk is precisely controlled with a sub-nanometer resolution using an embedded microscale heater, and the head has an active integrated thermometer of ~ 1 μm long, which is used to measure the head temperature for various air gaps [23, 26, 27]. Also, the HAMR head has an integrated laser diode that is used to locally heat the disk to a temperature higher than the Curie temperature of the magnetic layer ($\sim$ 400–500 °C) [5, 33]. It is noted that this head has a waveguide but no NFT because the waveguide head provides a larger laser spot size ($\sim$ 300 nm) than that in the NFT head ($\sim$ tens of nanometers) [4, 5, 33], and hence works better with the thermometer. On the other side of the air gap, the rotating disk has a FePt-based magnetic layer on a glass substrate that is coated with an amorphous carbon overcoat (protective layer, $\sim$ 2 nm thick) and a molecular layer of PFPE lubricant ($\sim$ 1 nm thick) [4, 8]. The head surface temperature was monitored for various air gap values to measure the thermal transport across the head-disk interface while the disk was rotating at a speed of 15 m/s (5400 RPM) relative to the stationary head, which is six orders of magnitude higher than that in the previous AFM-based studies [50, 66].

To determine the air-gap dependent thermal transport across the head-disk interface in the laser-off condition, we measured the thermometer's temperature rise (T) as the air gap

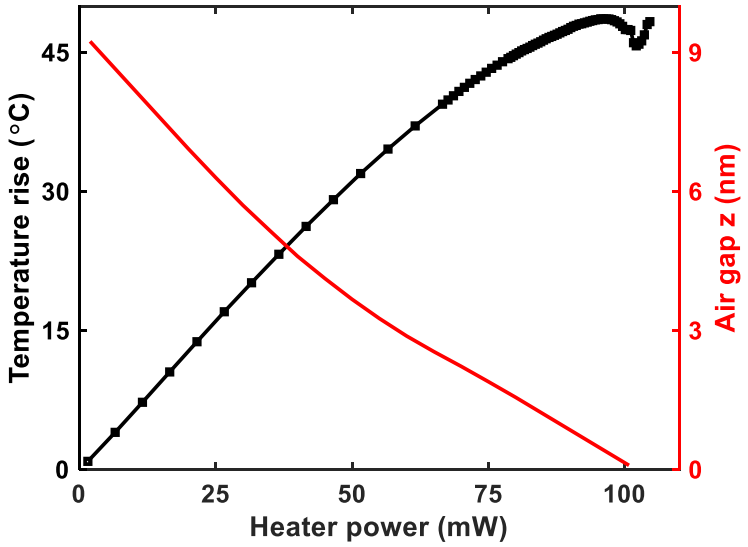

Figure 6.1: The measured temperature rise T and the simulated air gap z as a function of the heater power P in the laser-off condition.

was decreased by increasing the heater power (P). Figure 6.1 shows the temperature rise as a function of the heater power and the simulated air gap z [37]. The relationship between the heater power and the air gap z was obtained using a commercially available program named CMLAir. As the head surface approaches the disk, the thermometer's temperature evolution with the heater power can be sub-divided into three regimes (black dots in Figure 6.1). An initial increase in the thermometer temperature is due to joule heat dissipation in the heater, followed by a drop in the thermometer temperature at a narrower gap ($z < 1$ nm) where the enhanced near-field thermal transport overcomes the joule heat dissipation, and finally a sharper increase in the thermometer temperature is due to frictional heating produced by the high-speed head-disk contact, which occurs beginning at the heater power of 102 mW (contact onset). Meanwhile, the relation between the air gap z and the heater power shows nonlinearity when the gap narrows. The heater narrows the air gap with an efficiency of 0.1 nm per milliwatt when the gap is $\sim$ 8 nm, but this efficiency decreases to 0.05 nm per milliwatt for air gaps less than 1 nm.

To better interpret the experimental results, the rate of change of the thermometer temperature rise with the heater power, dT/dP, was extracted and plotted in Figure 6.2(a), along with the simulation result, where the heater power is denoted as the power relative to the contact onset with zero being the case of 102 mW heater power. The relative heater power essentially describes the gap between the head protrusion and the disk surface. Figure 6.2(a) shows that the dT/dP monotonically decreases with the gap before contact occurs, indicating an increasing heat transfer coefficient between the head and the disk. Figure 6.2(b) shows the simulation results of the heat transfer coefficients (HTCs) across the head-disk interface

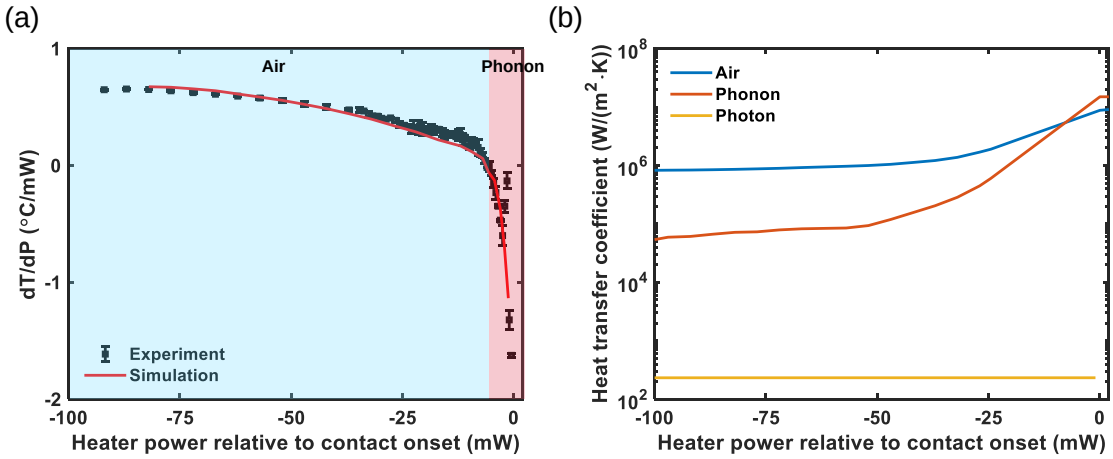

Figure 6.2: (a) The thermometer dT/dP as a function of the heater power relative to the heater power at contact onset. (b) The calculated heat transfer coefficients due to air conduction, phonon heat conduction and radiation carried by photons.

due to air conduction [150, 151], phonon heat conduction [52] and radiation [54]. The simulations in Figure 6.1 and Figure 6.2 were performed using a thermo-mechanical head-disk interface model, where the details can be found in Ref. [37]. Figure 6.2(b) shows that the radiation carried by photons is negligible compared to the two other mechanisms. Thus, the total head-disk heat transfer coefficient ($HTC_{\text{head-disk}}$) can be approximated as [37],

$$HTC_{\text{head-disk}} \approx HTC_{\text{air}} + HTC_{\text{phonon}} \tag{6.1}$$

where HTC_{air} and HTC_{phonon} are the heat transfer coefficients for the heat conduction by air and by phonons, respectively. They have comparable values when the relative heater power is larger than -14 mW ($z < 1$ nm). In Figure 6.2(a), the dT/dP is positive and decreases gradually for the large air gap regime (relative heater power < -6 mW, $z > \sim 0.4$ nm) where the air conduction generally dominates the head-disk thermal transport as shown in Figure 6.2(b). Then, at very small air gaps (-6 mW $<$ relative heater power < 0 mW, $z < \sim 0.4$ nm), the dT/dP drops steeply and goes below zero as the nonlinear phonon heat conduction begins to dominate cooling of the head thermometer. Moreover, the good agreement between the experimental result and the simulation result of dT/dP as shown in Figure 6.2(a) testifies that the phonon heat conduction is dominant at the sub-nanometer sized air gap between the head and the disk.

6.3 Thermal effect of lubricant

Here, the effect of the lubricant on the near-field thermal transport at the small head-disk gap ($z \sim$ several Å) is investigated. The dT/dP was measured as a function of the heater power

on disks with the lubricant thickness varying from 8.0 to 12.5 Å, as shown in Figure 6.3(a). As the head approaches the rotating disk, the rate of change of the head temperature versus the heater power, dT/dP, decays fast with the head-disk gap size and then increases due to the frictional heating after contact occurs, where the minimum $(dT/dP)_{\min}$ occurs at the heater power of 101.5 mW. It is noted that the bump around 100 mW may be because the thermometer is not at the closest point to the disk. The $(dT/dP)_{\min}$ for each lubricant thickness was extracted from the red dashed box in Figure 6.3(a), corresponding to the maximum of total thermal transport including air conduction, phonon heat conduction, contact heat conduction and frictional heating. Figure 6.3(b) shows the extracted $(dT/dP)_{\min}$ as a function of the lubricant thickness, where the inset shows a sketch for the $(dT/dP)_{\min}$. The disk with a thicker lubricant provides a larger $(dT/dP)_{\min}$ indicating a relatively stronger thermal barrier effect, while the disk with a thinner lubricant shows a smaller measured $(dT/dP)_{\min}$ and, thus, more cooling.

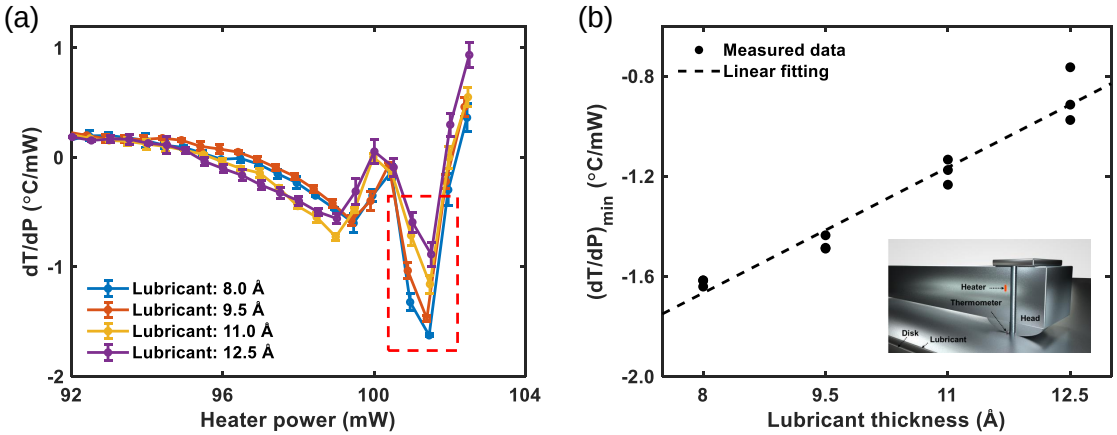

Figure 6.3: (a) The thermometer dT/dP as a function of the heater power on the disks with the lubricant thickness from 8.0 to 12.5 Å. (b) The extracted thermometer $(dT/dP)_{\min}$ as a function of the lubricant thickness. Inset: a sketch for the $(dT/dP)_{\min}$, corresponding to the maximum thermal transport.

To further study the thermal effect of the lubricant, Figure 6.4(a) plots the simulated dT/dP as a function of the HTC across the head-disk interface using the model in Ref. [37]. With the decrease of the air gap between the head and the disk, the increasing HTC causes a smaller dT/dP. By use of this relation, the measured $(dT/dP)_{\min}$ in Figure 6.3(b) was converted into maximum total HTC as shown in Figure 6.4(b). When the lubricant thickness increases by 1.0 Å, the total HTC decreases by 2.76×10^6 W/(m^2·K), which demonstrates the effect of the lubricant as a thermal barrier on the thermal transport between the head and the disk. It is known that the thermal conductance (tc) of the lubricant layer can be

expressed as [57],

$$\frac{1}{tc} = \frac{h}{k}; \quad k = \frac{k_{\text{bulk}}}{1 + \frac{4\Lambda_{\text{bulk}}}{3h}} \tag{6.2}$$

where h is the lubricant thickness, k is the effective thermal conductivity of the lubricant considering boundary scattering using Matthiessen's rule [152], k_{bulk} is the bulk thermal conductivity, and Λ_{bulk} is the bulk mean free path of the thermal energy carrier. Eq. 6.2 shows that the lubricant's thermal conductance (tc) decreases with its thickness (h), which qualitatively matches the previous experimental findings. In the following, we use the near-field thermal transport ($(dT/dP)_{\text{min}}$) at the small head-disk gap ($z \sim$ several Å) to in-situ measure the lubricant depletion and reflow dynamics according to Figure 6.3(b).

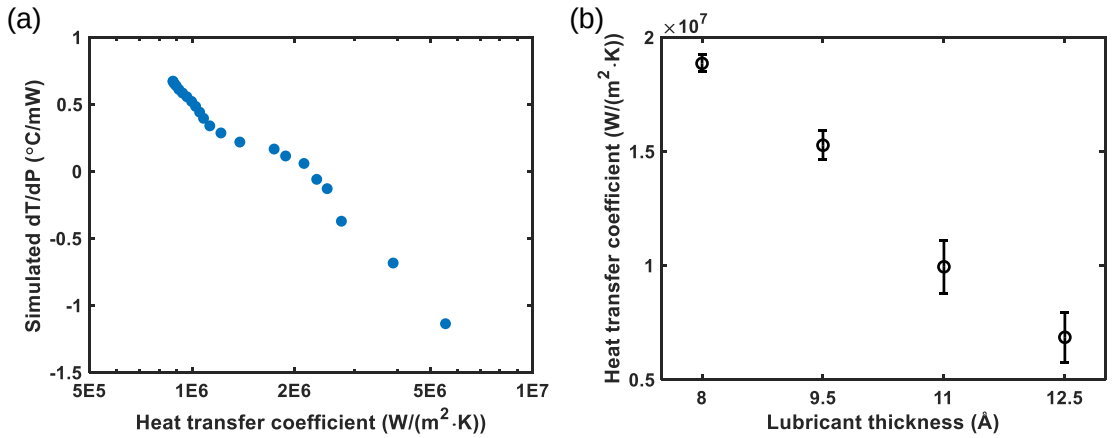

Figure 6.4: (a) The simulated dT/dP as a function of the HTC. (b) The maximum total HTCs for the four lubricant thicknesses.

6.4 In-situ measurements of lubricant dynamics

6.4.1 Lubricant depletion

In this subsection, we track the lubricant depletion dynamics by measuring the maximum thermal transport between the head and the disk, namely the $(dT/dP)_{\text{min}}$, as the lubricant is evaporated under thermal exposure. The head flying above the disk has an integrated laser diode to heat the disk to a temperature higher than the Curie temperature of the magnetic layer ($\sim$ 400–500 °C) to assist data writing [8]. By making use of the HAMR writing, we calibrated the disk peak temperature at each laser power condition as previously done in Section 4.3. Figure 6.5 illustrates the experimental scheme for the depletion dynamics of the lubricant as the disk was exposed to high temperature. First, the thermal transport was measured using the dT/dP as a function of the air gap on the original disk. Then, the disk

was heated to a constant temperature using the built-in laser diode, and the lubricant was depleted over a band of width ~ 10 μm. Considering that the laser spot size is ~ 300 nm, which is smaller than the thermometer's length (~ 1 μm), we moved the head back and forth by ~ 10 μm in the radial direction to generate a uniform band. Finally, we re-measured the dT/dP on the lubricant-depleted band as a function of the air gap to quantify the change in the $(dT/dP)_{\min}$ to derive the lubricant depletion, according to the calibration curve in Figure 6.3(b). This in-situ scheme has a resolution ~ 0.2 Å.

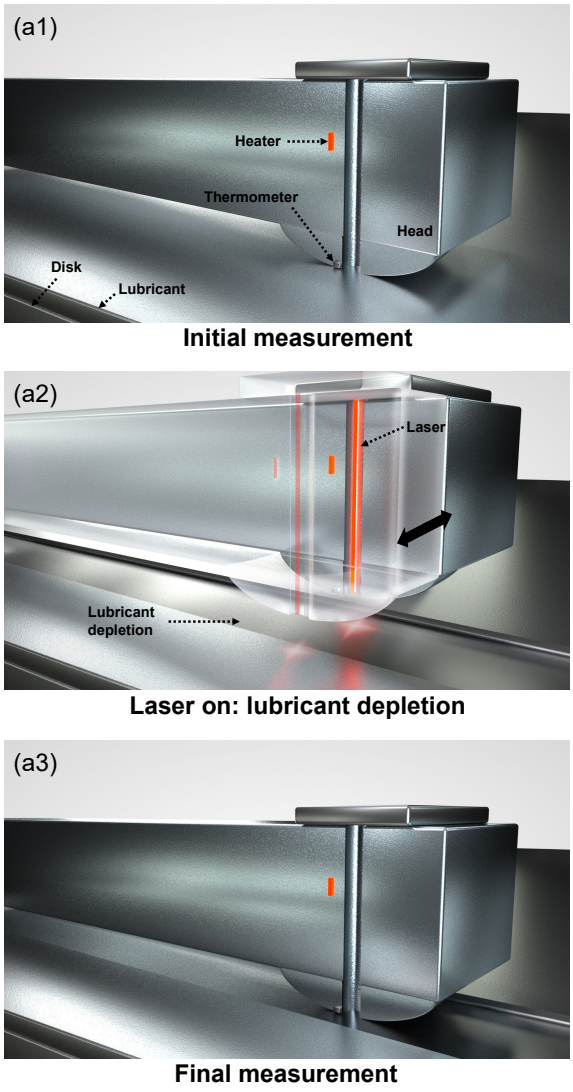

Figure 6.5: The experimental scheme for the measurement of lubricant depletion: (a1) initial measurement of the original lubricant thickness; (a2) lubricant depletion with laser on; (a3) final measurement of the lubricant thickness after depletion.

Figure 6.6 shows the in-situ measured lubricant depletion as a function of the disk peak temperature, where the accumulated laser exposure time was 60 s for the whole band and each track was heated by 1.8 s on average. All of the four lubricant thicknesses show similar results. When the disk peak temperature is lower than 220 °C, there is almost no reduction in the lubricant thickness, which indicates the lubricant's thermal stability. For temperatures higher than 220 °C, the lubricant depletion is proportional to the disk peak temperature rise. It is noted that the in-situ measured thermal stability of the lubricant bonded on a disk matches the bulk thermogravimetric analysis (TGA) experiments for the PFPE lubricant [153].

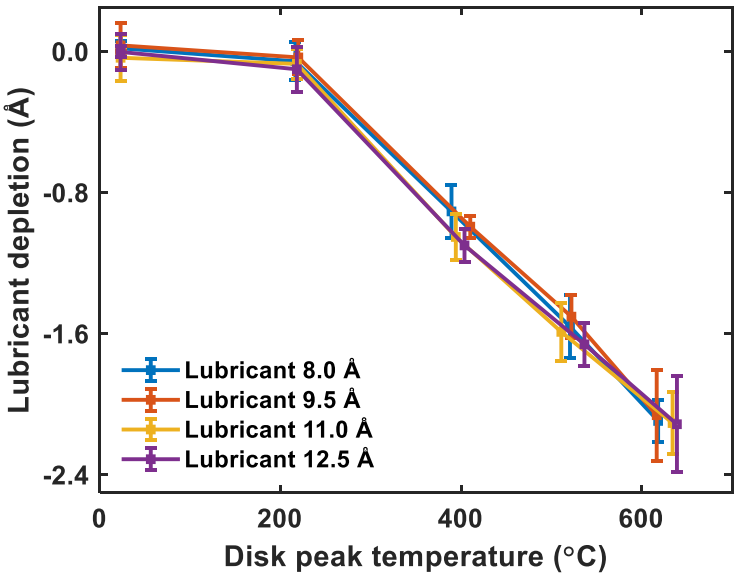

Figure 6.6: The lubricant depletion as a function of the disk peak temperature at the laser exposure time of 1.8 s/track.

We also explore the temporal evaporation dynamics of the lubricant depletion at a constant disk peak temperature of 650 °C. The thermometer dT/dP at the close spacing was measured to quantitatively determine the lubricant depletion at different laser exposure times. Figure 6.7(a) shows the lubricant depletion as a function of the laser exposure time. Interestingly, the initial 1.5 Å loss happens at the rate 3.4 Å/s, which is much faster than the subsequent lubricant loss at the rate 0.37 Å/s. We attribute the larger rate to the depletion of unbonded lubricant, which can be evaporated faster. To further confirm this behavior, we used an ex-situ optical surface analyzer (OSA, Candela 5100) to characterize the lubricant uniformity on the heated disk. Figure 6.7(b) shows the reflectivity change before/after the depletion as a function of the exposure time. The excellent agreement between the in-situ thermal transport based and the ex-situ optically based techniques verifies that the thermometer dT/dP measurement at the close spacing can track the lubricant depletion/loss

that occurs under the high-temperature HAMR operations. Moreover, this in-situ scheme can be implemented as a practical application in the HAMR hard disk drive technology.

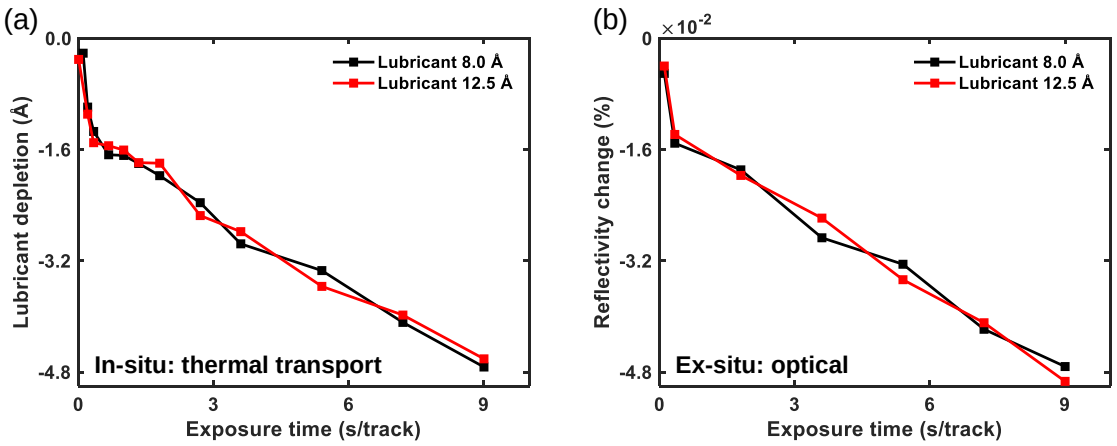

Figure 6.7: (a) The lubricant depletion and (b) the reflectivity change as a function of the laser exposure time at the disk peak temperature of 650 °C.

6.4.2 Lubricant reflow

Since the lubricant layer undergoes evaporation, decomposition and diffusion under thermal exposure [14, 82], its self-healing ability, also know as reflow, is crucial to reliability. Here, the reflow dynamics of the lubricant was quantitatively tracked by measuring its thickness over time after the thermal exposure, using the thermometer dT/dP at the close spacing. Figure 6.8 illustrates the experimental scheme. First, a depletion band was made on the disk using the built-in laser diode in the head, which is the same as Figure 6.5(a2). The disk was exposed to a high temperature of 650 °C for 1.8 s/track such that the lubricant was depleted by ~ 3 Å. Then, the laser was switched off for some time to allow the lubricant reflow, and the lubricant thickness in the band was measured as a function of the reflow time.

Figure 6.9(a) shows the measured lubricant thickness using the thermometer dT/dP at the close spacing as a function of the reflow time. The black and red dots correspond to the reflow dynamics on the two disks with initial lubricant thicknesses of 8.0 and 12.5 Å, respectively. The governing equation for the reflow dynamics can be derived using continuum theory as [149, 154]:

$$\frac{\partial h}{\partial t} + \frac{1}{3\mu}\frac{\partial}{\partial x}\left[h^3 \frac{d\prod(h)}{dh}\frac{\partial h}{\partial x}\right] = 0 \tag{6.3}$$

where $h = h(x,t)$ is the lubricant thickness, μ is the effective viscosity, $\prod(h) = A/h^3$ is the disjoining pressure due to van der Waals interactions between the lubricant and the disk carbon overcoat with A being the Hamaker constant. The governing partial differential equation

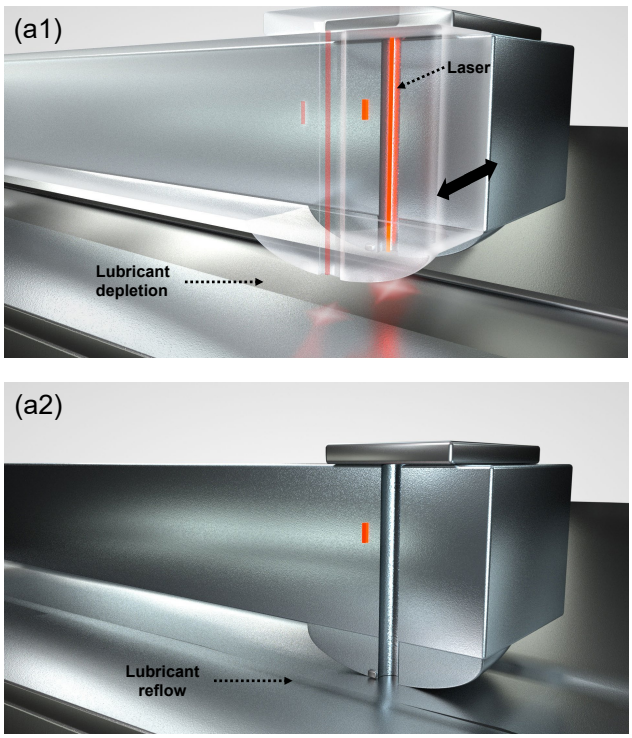

Figure 6.8: The experimental scheme for the measurement of lubricant reflow: (a1) lubricant depletion with laser on; (a2) measurement of the lubricant thickness after reflow.

was solved numerically by a MATLAB script, where the spatial derivative was approximated using the centered finite difference scheme (second order accurate) and the time derivative was discretized using the forward Euler method. The dashed lines in Figure 6.9(a) show the simulated reflow using Eq. 6.3 with the unknown Hamaker constant A as a fitting parameter ($A = 4.5 \times 10^{-21}$ J, close to the value used in Ref. [155]). It is noted that the time constant for the lubricant reflow is ~ 120 s for both thicknesses. To independently confirm the reflow dynamics, the lubricant reflow was also measured using the ex-situ OSA. In Figure 6.9(b), the black and red dots show the reflectivity change with respect to the non-heated condition as a function of the reflow time on the two disks. At $t = 0$ s, the absolute value of the reflectivity change is large due to the in-situ lubricant depletion as the disk is exposed to the high temperature. Subsequently, the laser is turned off, and the reflectivity change goes to zero indicating that the lubricant reflow occurs, with a similar time constant. It is worth noting that the in-situ thermal transport based and ex-situ optically based techniques show an excellent match for both the lubricant depletion and the reflow dynamics. In addition, this in-situ scheme only takes ~ 1 s, while the ex-situ OSA takes ~ 20 s because an annular region needs to be scanned. Hence, the in-situ scheme works more efficiently to capture the reflow dynamics precisely and timely.

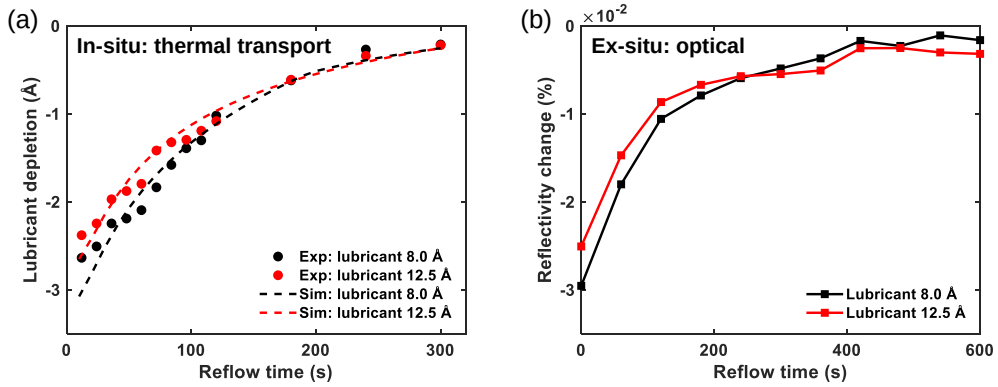

Figure 6.9: (a) The lubricant depletion and (b) the reflectivity change as a function of the reflow time after the disk was heated for 1.8 s/track at 650 °C.

6.5 Conclusion

In this chapter, we performed a near-field thermal transport study using the HAMR head-disk interface, which is a unique system for exploring the fundamental thermal transport mechanisms between two macroscopic bodies separated by sub-nanometer spacings. The thermal transport is dominated by air conduction and phonon heat conduction between the head and the disk, where the relative speed is six orders of magnitude higher than that in the previous AFM-based studies. The good agreement between the dT/dP measurement and the simulation provides the evidence that the phonon heat conduction is dominant at the operating sub-nanometer sized air gap between the head and the disk. Furthermore, the effect of the lubricant thickness on the thermal transport between the head and the disk was investigated. The lubricant layer behaves as a thermal barrier in that an increase of 1.0 Å in the lubricant thickness causes the decrease of 2.76 $\times$ 10^6 W/(m^2·K) in the HTC across the head-disk interface.

By use of the lubricant's thermal effect, we proposed the in-situ scheme to measure the lubricant thickness, and reported the first quantitative measurements of the sub-angstrom depletion and reflow dynamics of the nanometer-thick PFPE lubricant on the disk when it was exposed to the high-temperature HAMR-type operations. This in-situ scheme has a sub-angstrom resolution ($\sim$ 0.2 Å) and a faster response time than the ex-situ method (OSA), and hence it can be implemented in the HAMR hard disk drives. We envision that the insights obtained from this study will be important for future technology including HAMR hard disk drives, where two macroscopic objects are at a sub-nanometer spacing.

Chapter 7

Conclusion and future work

7.1 Conclusion

Heat-assisted magnetic recording (HAMR) has been proposed to increase the areal density of the hard disk drive (HDD) over the superparamagnetic limit of ~ 1 Tb/in^2. During the data writing process in HAMR, a built-in laser is used to locally heat the disk to lower the magnetic layer's coercivity. Therefore, the HAMR head-disk interface (HDI) is a system that combines nanoscale spacing (< 15 nm), high temperatures (head $\sim$ 150–250 °C, disk $\sim$ 400–500 °C), steep thermal gradient (~ 10 K/nm), and a high-speed sliding condition (5–40 m/s). However, the introduction of the laser brings several reliability issues on thermal transport, thermal protrusion, and thermally-induced material transfer, which need to be addressed. In this dissertation, experiments were performed to investigate these issues both for fundamental understanding and for practical applications such as HAMR and other microelectronics devices. Furthermore, a thermal mapping technique and a scheme for lubricant thickness measurement were proposed and demonstrated using the HDD technology.

Chapter 2 presented an experimental study of the thermal transport across a closing gap between the recording head and the non-rotating substrate. When the head surface approached the substrate using a joule heater, the thermal transport across the gap was investigated by measuring the head temperature. The effects of the substrate material, relative humidity and laser current on the thermal transport were studied. At the gap $< \sim 2$ nm, an enhanced thermal transport due to phonon heat conduction was observed. The thermal transport across the gap became stronger when a substrate with a higher thermal conductivity was used or when a thin water film formed in the gap under high relative humidity conditions (RH $> 75\%$). It was also found that the head could sense a back-heating from the hot spot on the substrate that was due to the built-in laser.

In Chapter 3, we performed the flying touchdown experiments to investigate the thermal protrusions involved in the HAMR. A touchdown-based method to measure the angstrom-level laser-induced protrusion (LIP) and the fly height change (FHC), which were caused by the energy loss during the laser delivery, was introduced. The experimental results showed

that the FHC needed $\sim$ 28 ms to become stable, and that the LIP was 1.53–0.75 Å at the operating linear velocity of 12–24 m/s. Under the laser heating, more vibration modes appeared in the slider dynamics, which was likely due to the mechanical interactions between the LIP and the moving disk surface. Moreover, it was demonstrated that the head protrusion shape could be modulated by use of the dual heaters inside the head, and thus the touchdown area could be controlled precisely.

In Chapter 4, the smear formation and mitigation in HAMR were investigated experimentally. The disk temperature and the laser exposure time were controlled to study the smear formation mechanism. The smear began to form when the disk temperature was higher than the lubricant evaporation temperature, and the evaporation occurred for a certain time. The smear on the head surface presented a unique pattern of two major traces located at a distance from the track center, which was possibly because of the thermocapillary stress. Then two smear mitigation strategies were proposed: a mechanical approach and a thermal approach. In the mechanical approach, the upstream/downstream smear could be burnished away by use of the dual heaters respectively within several revolutions, and the head remained undamaged. In the thermal approach, the smear was spread out from traces to dots and was mitigated after a long duration $\sim$ 40 min. Additionally, it was found that a pulsed laser operating at a higher frequency could produce less upstream smear.

Subsequently, Chapter 5 presented a versatile thermal mapping technique based on the phase change material $Ge_2Sb_2Te_5$, which had negligible temperature interference and required minimal calibration. The technique was demonstrated using a nano-heater and a micro-heater inside the recording head. The $Ge_2Sb_2Te_5$ was deposited as a thin film on the head surface, and underwent a crystalline transition at T_g with large changes in its density and optical reflectivity. Due to the property changes, the phase transition was characterized by atomic force microscopy (AFM) at the nanoscale or an optical microscope at the microscale. The thermal mappings for the nano-heater and the micro-heater were constructed using the phase change temperature contours (PCTCs), and they agreed well with the simulation results. This technique could spatially resolve the surface temperatures of operational microelectronic devices from nanoscale to microscale dimensions with a resolution as high as 20 nm thanks to the continuous nature of the thin film.

Chapter 6 demonstrated a near-field thermal transport based scheme for the lubricant thickness measurement. The effect of the lubricant as a thermal barrier on the thermal transport between the head and the disk was calibrated, which was then used to determine the lubricant thickness. Using the scheme, we reported the first quantitative measurements of the lubricant depletion and reflow dynamics under the high-temperature HAMR-type operations. This in-situ scheme had a sub-angstrom resolution $\sim$ 0.2 Å and a faster response time compared to the commonly-used optical surface analyzer (OSA), and hence it could be implemented in the HAMR hard disk drives.

To summarize, our hope is that our findings will provide a better understanding of the thermal transport across the head-disk interface, contribute towards the protrusion management and the smear management in the HAMR technology, and give new insights into thermal measurements and thin film measurements.

7.2 Future work

Since the HAMR hard disk drive is still in the early stage as a product, more studies can be performed in the future to increase its reliability and its lifetime. Also, more research on the nanoscale thermal transport can be conducted to further the fundamental understanding.

In Chapter 2, the effects of the relative humidity (RH) and the laser current on the thermal transport across a nanoscale gap were explained qualitatively. Simulations need to be performed to quantitatively understand the experimental results. The simulation for the relative humidity should consider the water layer's formation from the ambient humidity and how it affects the nanoscale thermal transport. To fully understand the laser effect, a detailed HAMR head model with the built-in laser delivery needs to be established. The model can also be used to verify the experimental findings of thermal protrusions and thermally-induced material transfer in Chapter 3 and Chapter 4.

Furthermore, the HAMR heads used in this dissertation only had the waveguide (WG) and did not have the near-field transducer (NFT). The NFT-HAMR head will behave differently from the WG-HAMR head because the laser is focused to a much smaller area at the NFT and causes a higher temperature rise. The laser spot size in the NFT-HAMR head is also much smaller than that in the WG-HAMR head, which will lead to a steeper thermal gradient and affect the results presented in Chapter 3 and Chapter 4, but the methods still work. Therefore, future studies using the NFT-HAMR heads are worth doing if the NFT-HAMR heads become available, and will be closer to the actual HAMR technology.

Finally, the author sincerely hopes that the challenges in the HAMR technology can be conquered and the HAMR hard disk drive can be released to the public soon.

Bibliography

[1] D. Reinsel, J. Gantz, and J. Rydning. "The digitization of the world from edge to core". In: *Framingham: International Data Corporation* (2018), p. 16.

[2] R. Fontana and G. Decad. "The 2018 Storage Landscape-An 11 Year Perspective (2008-2019): LTO Tape Media HDD NAND". In: *the 2018 Storage Landscape–Library of Congress*. 2019.

[3] R. E. Rottmayer et al. "Heat-assisted magnetic recording". In: *IEEE Transactions on Magnetics* 42.10 (2006), pp. 2417–2421.

[4] M. H. Kryder et al. "Heat assisted magnetic recording". In: *Proceedings of the IEEE* 96.11 (2008), pp. 1810–1835.

[5] W. Challener et al. "Heat-assisted magnetic recording by a near-field transducer with efficient optical energy transfer". In: *Nature Photonics* 3.4 (2009), pp. 220–224.

[6] L. Pan and D. B. Bogy. "Heat-assisted magnetic recording". In: *Nature Photonics* 3.4 (2009), pp. 189–190.

[7] A. K. Himes and J. C. Chaffee. *Head gimbal assembly including dampening for air bearing vibration*. US Patent 6,967,821. Nov. 2005.

[8] D. Weller et al. "A HAMR Media Technology Roadmap to an Areal Density of 4 Tb/in2". In: *IEEE Transactions on Magnetics* 50.1 (2013), pp. 1–8.

[9] X.-C. Guo et al. "Multidentate functionalized lubricant for ultralow head/disk spacing in a disk drive". In: *Journal of Applied Physics* 100.4 (2006), p. 044306.

[10] M. S. G. Sarabi and D. B. Bogy. "Simulation of the performance of various PFPE lubricants under heat assisted magnetic recording conditions". In: *Tribology Letters* 56.2 (2014), pp. 293–304.

[11] T. E. Karis. "Lubricants for the disk drive industry". In: *Lubricant Additives*. CRC Press, 2017, pp. 503–559.

[12] S. Sarabi and D. B. Bogy. "Effect of functional end-groups on lubricant reflow in heat-assisted magnetic recording (hamr)". In: *Tribology Letters* 65.1 (2017), pp. 1–10.

[13] X.-C. Guo et al. "A multidentate lubricant for use in hard disk drives at sub-nanometer thickness". In: *Journal of Applied Physics* 111.2 (2012), p. 024503.

[14] J. D. Kiely, P. M. Jones, and J. Hoehn. "Materials challenges for the heat-assisted magnetic recording head–disk interface". In: *MRS Bulletin* 43.2 (2018), pp. 119–124.

[15] L.-Y. Zhu and D. Bogy. "A comparison of head-to-disk spacing fluctuation on hard and stretch-surface recording disks". In: *IEEE Transactions on Magnetics* 23.5 (1987), pp. 3447–3449.

[16] E. Grochowski and R. F. Hoyt. "Future trends in hard disk drives". In: *IEEE Transactions on Magnetics* 32.3 (1996), pp. 1850–1854.

[17] D. W. Meyer, P. E. Kupinski, and J. C. Liu. *Slider with temperature responsive transducer positioning*. US Patent 5,991,113. Nov. 1999.

[18] M. Kurita et al. "Flying-height reduction of magnetic-head slider due to thermal protrusion". In: *IEEE Transactions on Magnetics* 41.10 (2005), pp. 3007–3009.

[19] J.-Y. Juang et al. "Numerical and experimental analyses of nanometer-scale flying height control of magnetic head with heating element". In: *IEEE Transactions on Magnetics* 44.11 (2008), pp. 3679–3682.

[20] N. Liu, J. Zheng, and D. B. Bogy. "Predicting the flying performance of thermal flying-height control sliders in hard disk drives". In: *Journal of Applied Physics* 108.1 (2010), p. 016102.

[21] J. Zheng and D. B. Bogy. "Investigation of flying-height stability of thermal fly-height control sliders in lubricant or solid contact with roughness". In: *Tribology Letters* 38.3 (2010), pp. 283–289.

[22] S. V. Canchi and D. B. Bogy. "Thermal fly-height control slider instability and dynamics at touchdown: explanations using nonlinear systems theory". In: *Journal of Tribology* 133.2 (2011), p. 021902.

[23] Y. Ma et al. "Controlled heat flux measurement across a closing nanoscale gap and its comparison to theory". In: *Applied Physics Letters* 108.21 (2016), p. 213105.

[24] Y. Ma et al. "Measurement and simulation of nanoscale gap heat transfer using a read/write head with a contact sensor". In: *IEEE Transactions on Magnetics* 53.2 (2016), pp. 1–5.

[25] H. Wu et al. "Nanoscale heat transfer in the head-disk interface for heat assisted magnetic recording". In: *Applied Physics Letters* 108.9 (2016), p. 093106.

[26] H. Wu and D. Bogy. "Use of an embedded contact sensor to study nanoscale heat transfer in heat assisted magnetic recording". In: *Applied Physics Letters* 110.3 (2017), p. 033104.

[27] J. Xu et al. "Contact/clearance sensor for HDI subnanometer regime". In: *IEEE Transactions on Magnetics* 50.3 (2014), pp. 114–118.

[28] Y. Ma et al. "Study of head-disk interface characterization using touchdown sensor and electromagnetic signal in hard disk drives". In: *IEEE Transactions on Magnetics* 51.11 (2015), pp. 1–4.

[29] B. Marchon et al. "The head-disk interface roadmap to an areal density of Tbit/in2". In: *Advances in Tribology* 2013 (2013).

[30] M. Cordle et al. "Impact of radius and skew angle on areal density in heat assisted magnetic recording hard disk drives". In: *AIP Advances* 8.5 (2018), p. 056507.

[31] V. Skumryev et al. "Beating the superparamagnetic limit with exchange bias". In: *Nature* 423.6942 (2003), pp. 850–853.

[32] A. Chernyshov et al. "Measurement of Curie temperature distribution relevant to heat assisted magnetic recording". In: *Journal of Applied Physics* 117.17 (2015), p. 17D111.

[33] B. C. Stipe et al. "Magnetic recording at 1.5 Pb m- 2 using an integrated plasmonic antenna". In: *Nature Photonics* 4.7 (2010), pp. 484–488.

[34] E. Schreck et al. "Thermal aspects and static/dynamic protrusion behaviors in heat-assisted magnetic recording". In: *IEEE Transactions on Magnetics* 50.3 (2014), pp. 126–131.

[35] B. Marchon et al. "Head–disk interface materials issues in heat-assisted magnetic recording". In: *IEEE Transactions on Magnetics* 50.3 (2014), pp. 137–143.

[36] J. D. Kiely et al. "Write-induced head contamination in heat-assisted magnetic recording". In: *IEEE Transactions on Magnetics* 53.2 (2016), pp. 1–7.

[37] S. Sakhalkar et al. "Investigation of heat transfer across a nanoscale air gap between a flying head and a rotating disk". In: *Journal of Applied Physics* 128.8 (2020), p. 084301.

[38] J. B. Dahl and D. B. Bogy. "Static and dynamic slider air-bearing behavior in heat-assisted magnetic recording under thermal flying height control and laser system-induced protrusion". In: *Tribology Letters* 54.1 (2014), pp. 35–50.

[39] C. Zhong et al. "Effective heat dissipation in an adiabatic near-field transducer for HAMR". In: *Optics Express* 26.15 (2018), pp. 18842–18854.

[40] S. Xiong et al. "Spacing control in heat-assisted magnetic recording". In: *IEEE Transactions on Magnetics* 55.3 (2018), pp. 1–6.

[41] M. S. Lim and A. J. Gellman. "Kinetics of laser induced desorption and decomposition of Fomblin Zdol on carbon overcoats". In: *Tribology International* 38.6-7 (2005), pp. 554–561.

[42] N. Tagawa and H. Tani. "Lubricant depletion characteristics induced by rapid laser heating in thermally assisted magnetic recording". In: *IEEE Transactions on Magnetics* 47.1 (2010), pp. 105–110.

[43] K. Yakata et al. "Smear and decomposition mechanism of magnetic disk PFPE lubricant film by laser heating in air and helium conditions". In: *Tribology Online* 15.3 (2020), pp. 186–193.

[44] J.-G. Zhu, X. Zhu, and Y. Tang. "Microwave assisted magnetic recording". In: *IEEE Transactions on Magnetics* 44.1 (2007), pp. 125–131.

[45] C. Boone et al. *Heat sink for a spin torque oscillator (STO) in microwave assisted magnetic recording (MAMR)*. US Patent 8,995,088. Mar. 2015.

[46] D. Polder and M. Van Hove. "Theory of radiative heat transfer between closely spaced bodies". In: *Physical Review B* 4.10 (1971), p. 3303.

[47] A. Volokitin and B. N. Persson. "Near-field radiative heat transfer and noncontact friction". In: *Reviews of Modern Physics* 79.4 (2007), p. 1291.

[48] A. Narayanaswamy and G. Chen. "Thermal near-field radiative transfer between two spheres". In: *Physical Review B* 77.7 (2008), p. 075125.

[49] E. Rousseau et al. "Radiative heat transfer at the nanoscale". In: *Nature Photonics* 3.9 (2009), pp. 514–517.

[50] S. Shen, A. Narayanaswamy, and G. Chen. "Surface phonon polaritons mediated energy transfer between nanoscale gaps". In: *Nano Letters* 9.8 (2009), pp. 2909–2913.

[51] B. V. Budaev and D. B. Bogy. "Computation of radiative heat transport across a nanoscale vacuum gap". In: *Applied Physics Letters* 104.6 (2014), p. 061109.

[52] B. V. Budaev and D. B. Bogy. "Heat transport by phonon tunneling across layered structures used in heat assisted magnetic recording". In: *Journal of Applied Physics* 117.10 (2015), p. 104512.

[53] K. Kim et al. "Radiative heat transfer in the extreme near field". In: *Nature* 528.7582 (2015), p. 387.

[54] B. V. Budaev, A. Ghafari, and D. B. Bogy. "Intense radiative heat transport across a nano-scale gap". In: *Journal of Applied Physics* 119.14 (2016), p. 144501.

[55] B. Song et al. "Radiative heat conductances between dielectric and metallic parallel plates with nanoscale gaps". In: *Nature nanotechnology* 11.6 (2016), p. 509.

[56] B. V. Budaev and D. B. Bogy. "Systems with a constant heat flux with applications to radiative heat transport across nanoscale gaps and layers". In: *Zeitschrift für angewandte Mathematik und Physik* 69.3 (2018), p. 71.

[57] S. Sakhalkar et al. "Numerical and experimental investigation of heat transfer across a nanoscale gap between a magnetic recording head and various media". In: *Applied Physics Letters* 115.22 (2019), p. 223102.

[58] Y. Ma et al. "A Study of the Nanoscale Heat Transfer in the HDD Head–Disk Interface Based on a Static Touchdown Experiment". In: *IEEE Transactions on Magnetics* 56.3 (2020), pp. 1–7.

[59] S. V. Sakhalkar and D. B. Bogy. "Effect of rheology and slip on lubricant deformation and disk-to-head transfer during heat-assisted magnetic recording (HAMR)". In: *Tribology Letters* 66.4 (2018), p. 145.

[60] J. Pendry. "Radiative exchange of heat between nanostructures". In: *Journal of Physics: Condensed Matter* 11.35 (1999), p. 6621.

[61] V. Fernández-Hurtado et al. "Enhancing near-field radiative heat transfer with Si-based metasurfaces". In: *Physical Review Letters* 118.20 (2017), p. 203901.

[62] M. Laroche, R. Carminati, and J.-J. Greffet. "Near-field thermophotovoltaic energy conversion". In: *Journal of Applied Physics* 100.6 (2006), p. 063704.

[63] M. Francoeur, R. Vaillon, and M. P. Mengüç. "Thermal impacts on the performance of nanoscale-gap thermophotovoltaic power generators". In: *IEEE Transactions on Energy Conversion* 26.2 (2011), pp. 686–698.

[64] A. Fiorino et al. "Nanogap near-field thermophotovoltaics". In: *Nature nanotechnology* 13.9 (2018), pp. 806–811.

[65] A. Kittel et al. "Near-field heat transfer in a scanning thermal microscope". In: *Physical Review Letters* 95.22 (2005), p. 224301.

[66] A. Narayanaswamy et al. "Breakdown of the Planck blackbody radiation law at nanoscale gaps". In: *Applied Physics A* 96.2 (2009), pp. 357–362.

[67] D. Thompson et al. "Hundred-fold enhancement in far-field radiative heat transfer over the blackbody limit". In: *Nature* 561.7722 (2018), pp. 216–221.

[68] V. Chiloyan et al. "Transition from near-field thermal radiation to phonon heat conduction at sub-nanometre gaps". In: *Nature communications* 6 (2015), p. 6755.

[69] K. Y. Fong et al. "Phonon heat transfer across a vacuum through quantum fluctuations". In: *Nature* 576.7786 (2019), pp. 243–247.

[70] B. Song et al. "Near-field radiative thermal transport: From theory to experiment". In: *AIP Advances* 5.5 (2015), p. 053503.

[71] J. Zheng. "Dynamics and stability of thermal flying-height control sliders in hard disk drives". PhD thesis. UC Berkeley, 2012.

[72] F. O'brien. "The control of humidity by saturated salt solutions". In: *Journal of Scientific Instruments* 25.3 (1948), p. 73.

[73] D. B. Asay and S. H. Kim. "Effects of adsorbed water layer structure on adhesion force of silicon oxide nanoasperity contact in humid ambient". In: *The Journal of Chemical Physics* 124.17 (2006), p. 174712.

[74] M. Shamsa et al. "Thermal conductivity of diamond-like carbon films". In: *Applied Physics Letters* 89.16 (2006), p. 161921.

[75] M. Suk, P. Dennig, and D. Gillis. "Magnetic erasures due to impact induced interfacial heating and magnetostriction". In: *Journal of Tribology* 122.1 (2000), pp. 264–268.

[76] Q. Cheng et al. "Dependence of nanoscale heat transfer across a closing gap on the substrate material and ambient humidity". In: *Applied Physics Letters* 116.21 (2020), p. 213102.

[77] Q. Cheng, Y. Ma, and D. Bogy. "Effect of Humidity on the Nanoscale Heat Transfer at the Head-Media Interface". In: *ASME 2019 28th Conference on Information Storage and Processing Systems*. American Society of Mechanical Engineers Digital Collection.

[78] Q. Cheng and D. B. Bogy. "Experimental Study of Nanoscale Head-Disk Heat Transfer In Heat-Assisted Magnetic Recording". In: *Information Storage and Processing Systems*. Vol. 84799. American Society of Mechanical Engineers. 2021, V001T05A001.

[79] M. A. Seigler et al. "Integrated heat assisted magnetic recording head: Design and recording demonstration". In: *IEEE Transactions on Magnetics* 44.1 (2007), pp. 119–124.

[80] B. Xu et al. "Relationship between near field optical transducer laser absorption and its efficiency". In: *IEEE Transactions on Magnetics* 48.5 (2012), pp. 1789–1793.

[81] Y. Hu et al. "Head flying characteristics in heat assisted magnetic recording considering various nanoscale heat transfer models". In: *Journal of Applied Physics* 123.3 (2018), p. 034303.

[82] S. V. Sakhalkar and D. B. Bogy. "Viscoelastic Lubricant Deformation and Disk-to-Head Transfer During Heat-Assisted Magnetic Recording". In: *IEEE Transactions on Magnetics* 55.7 (2018), pp. 1–6.

[83] N. Tagawa et al. "Experimental study of lubricant depletion induced by pulsed laser irradiation heating in heat-assisted magnetic recording". In: *Microsystem Technologies* 26.1 (2020), pp. 5–10.

[84] D. Li et al. "A new AFM-based technique to detect the NFT protrusion on HAMR head". In: *IEEE Transactions on Magnetics* 49.7 (2013), pp. 3576–3579.

[85] Z. Zhang et al. "Characterization of laser-induced protrusion in HAMR by the burnish method". In: *IEEE Transactions on Magnetics* 52.2 (2015), pp. 1–6.

[86] S. Xiong et al. "Setting write spacing in heat assisted magnetic recording". In: *IEEE Transactions on Magnetics* 54.8 (2018), pp. 1–7.

[87] W.-C. D. Hsiao and X. Shen. *Magnetic head with self compensating dual thermal fly height control*. US Patent 8,634,167. Jan. 2014.

[88] J. Contreras, I. R. McFadyen, and E. Schreck. *Implementing dual partially independent thermal flyheight control (TFC) for hard disk drives*. US Patent 9,564,163. Feb. 2017.

[89] M. Suk et al. "Verification of thermally induced nanometer actuation of magnetic recording transducer to overcome mechanical and magnetic spacing challenges". In: *IEEE Transactions on Magnetics* 41.11 (2005), pp. 4350–4352.

[90] J.-Y. Juang and D. B. Bogy. "Air-bearing effects on actuated thermal pole-tip protrusion for hard disk drives". In: *Journal of Tribology* 129.3 (2007), pp. 570–578.

[91] H. Li, C.-T. Yin, and F. E. Talke. "Thermal insulator design for optimizing the efficiency of thermal flying height control sliders". In: *Journal of Applied Physics* 105.7 (2009), p. 07C122.

[92] H. Zheng, H. Li, and F. E. Talke. "Numerical simulation of a thermal flying height control slider with dual heater and insulator elements". In: *IEEE Transactions on Magnetics* 45.10 (2009), pp. 3628–3631.

[93] H. Zheng et al. "The effect of write current on thermal flying height control sliders with dual heater/insulator elements". In: *Microsystem Technologies* 17.5-7 (2011), pp. 959–964.

[94] Y. Ma. "Study of Dynamics and Nanoscale Heat Transfer of Head Disk Interface in Hard Disk Drives". PhD thesis. UC Berkeley, 2018.

[95] Y.-K. Chen, J. Zheng, and D. B. Bogy. "Light contact and surfing state dynamics of air bearing sliders in hard disk drives". In: *Applied Physics Letters* 100.24 (2012), p. 243104.

[96] J. Wang et al. "HAMR writing process model-based compensation of laser-induced transients". In: *IEEE Transactions on Magnetics* 53.3 (2016), pp. 1–7.

[97] S. Rajauria et al. "Electrostatically tunable adhesion in a high speed sliding interface". In: *Physical Review Letters* 120.2 (2018), p. 026101.

[98] Y.-K. Chen, J.-P. Peng, and D. B. Bogy. "Thermal protrusion-induced air bearing slider instability at disk proximity and light contact". In: *IEEE Transactions on Magnetics* 50.7 (2014), pp. 1–7.

[99] Q. Cheng et al. "Measurement of angstrom-level laser induced protrusion using touchdown in heat-assisted magnetic recording". In: *Applied Physics Letters* 117.15 (2020), p. 153105.

[100] Q. Cheng et al. "Experimental Study on Laser-Induced Protrusion in Heat-Assisted Magnetic Recording". In: *Information Storage and Processing Systems*. Vol. 83600. American Society of Mechanical Engineers. 2020, V001T05A002.

[101] V. Raman, D. Gillis, and R. Wolter. "Flyability failures due to organic siloxanes at the head/disk interface". In: *Journal of Tribology* 122.2 (2000), pp. 444–449.

[102] Y. Yang et al. "Head–disk lubricant transfer and deposition during heat-assisted magnetic recording write operations". In: *IEEE Transactions on Magnetics* 51.11 (2015), pp. 1–4.

[103] S. Xiong et al. "Material transfer inside head disk interface for heat assisted magnetic recording". In: *Tribology Letters* 65.2 (2017), p. 74.

[104] J. Aoyama et al. "A head cleaning procedure for heat-assisted magnetic recording". In: *IEEE Transactions on Magnetics* 53.11 (2017), pp. 1–4.

[105] S. Xiong et al. "Experimental Study of Material Pick Up on Heat-Assisted Magnetic Recording (HAMR) Heads". In: *Tribology Letters* 69.2 (2021), pp. 1–7.

[106] Q. Cheng and D. B. Bogy. "Experimental study of smear formation and removal in heat-assisted magnetic recording". In: *Tribology International* 165 (2022), p. 107258.

[107] R. Cavin et al. "Research directions and challenges in nanoelectronics". In: *Journal of Nanoparticle Research* 8.6 (2006), pp. 841–858.

[108] W. Haensch et al. "Silicon CMOS devices beyond scaling". In: *IBM Journal of Research and Development* 50.4.5 (2006), pp. 339–361.

[109] E. Pop. "Energy dissipation and transport in nanoscale devices". In: *Nano Research* 3.3 (2010), pp. 147–169.

[110] C. Y. Jin et al. "Localized temperature and chemical reaction control in nanoscale space by nanowire array". In: *Nano Letters* 11.11 (2011), pp. 4818–4825.

[111] F. Dejene et al. "Spin heat accumulation and spin-dependent temperatures in nanopillar spin valves". In: *Nature Physics* 9.10 (2013), pp. 636–639.

[112] J. Lee and N. A. Kotov. "Thermometer design at the nanoscale". In: *Nano Today* 2.1 (2007), pp. 48–51.

[113] C. D. Brites et al. "Thermometry at the nanoscale". In: *Nanoscale* 4.16 (2012), pp. 4799–4829.

[114] M. Nonnenmacher and H. Wickramasinghe. "Scanning probe microscopy of thermal conductivity and subsurface properties". In: *Applied Physics Letters* 61.2 (1992), pp. 168–170.

[115] L. Shi et al. "Scanning thermal microscopy of carbon nanotubes using batch-fabricated probes". In: *Applied Physics Letters* 77.26 (2000), pp. 4295–4297.

[116] Y. Gao and Y. Bando. "Carbon nanothermometer containing gallium". In: *Nature* 415.6872 (2002), pp. 599–599.

[117] Y. De Wilde et al. "Thermal radiation scanning tunnelling microscopy". In: *Nature* 444.7120 (2006), pp. 740–743.

[118] G. Tessier et al. "Back side thermal imaging of integrated circuits at high spatial resolution". In: *Applied Physics Letters* 90.17 (2007), p. 171112.

[119] T. Brintlinger et al. "Electron thermal microscopy". In: *Nano Letters* 8.2 (2008), pp. 582–585.

[120] V. V. Deshpande et al. "Spatially resolved temperature measurements of electrically heated carbon nanotubes". In: *Physical Review Letters* 102.10 (2009), p. 105501.

[121] K. Kim et al. "Ultra-high vacuum scanning thermal microscopy for nanometer resolution quantitative thermometry". In: *ACS Nano* 6.5 (2012), pp. 4248–4257.

[122] F. Menges et al. "Quantitative thermometry of nanoscale hot spots". In: *Nano Letters* 12.2 (2012), pp. 596–601.

[123] H. Guo et al. "Vanadium dioxide nanowire-based microthermometer for quantitative evaluation of electron beam heating". In: *Nature communications* 5.1 (2014), pp. 1–5.

[124] G. Hwang, J. Chung, and O. Kwon. "Enabling low-noise null-point scanning thermal microscopy by the optimization of scanning thermal microscope probe through a rigorous theory of quantitative measurement". In: *Review of Scientific Instruments* 85.11 (2014), p. 114901.

[125] A. A. Kinkhabwala et al. "Nanoscale thermal mapping of HAMR heads using polymer imprint thermal mapping". In: *IEEE Transactions on Magnetics* 52.2 (2015), pp. 1–4.

[126] J. Martinek, P. Klapetek, and A. C. Campbell. "Methods for topography artifacts compensation in scanning thermal microscopy". In: *Ultramicroscopy* 155 (2015), pp. 55–61.

[127] M. Mecklenburg et al. "Nanoscale temperature mapping in operating microelectronic devices". In: *Science* 347.6222 (2015), pp. 629–632.

[128] K. Okabe et al. "Intracellular temperature mapping with a fluorescent polymeric thermometer and fluorescence lifetime imaging microscopy". In: *Nature communications* 3.1 (2012), pp. 1–9.

[129] G. Kucsko et al. "Nanometre-scale thermometry in a living cell". In: *Nature* 500.7460 (2013), pp. 54–58.

[130] J. Feng et al. "Electronic structure and enhanced charge-density wave order of monolayer VSe2". In: *Nano Letters* 18.7 (2018), pp. 4493–4499.

[131] J. C. Idrobo et al. "Temperature measurement by a nanoscale electron probe using energy gain and loss spectroscopy". In: *Physical Review Letters* 120.9 (2018), p. 095901.

[132] J. Christofferson et al. "Microscale and nanoscale thermal characterization techniques". In: *Journal of Electronic Packaging* 130.4 (2008), p. 041101.

[133] F. Menges et al. "Temperature mapping of operating nanoscale devices by scanning probe thermometry". In: *Nature communications* 7.1 (2016), pp. 1–6.

[134] Y. Shimizu et al. "Nano-scale defect mapping on a magnetic disk surface using a contact sensor". In: *IEEE Transactions on Magnetics* 47.10 (2011), pp. 3426–3432.

[135] I. Friedrich et al. "Structural transformations of Ge 2 Sb 2 Te 5 films studied by electrical resistance measurements". In: *Journal of Applied Physics* 87.9 (2000), pp. 4130–4134.

[136] S. Guerin et al. "Synthesis and screening of phase change chalcogenide thin film materials for data storage". In: *ACS Combinatorial Science* 19.7 (2017), pp. 478–491.

[137] H. Fritzsche and S. Ovshinsky. "Calorimetric and dilatometric studies on chalcogenide alloy glasses". In: *Journal of Non-Crystalline Solids* 2 (1970), pp. 148–154.

[138] E. Morales-Sanchez et al. "Determination of the glass transition and nucleation temperatures in Ge2Sb2Te5 sputtered films". In: *Journal of Applied Physics* 91.2 (2002), pp. 697–702.

[139] G. W. Burr et al. "Phase change memory technology". In: *Journal of Vacuum Science & Technology B, Nanotechnology and Microelectronics: Materials, Processing, Measurement, and Phenomena* 28.2 (2010), pp. 223–262.

[140] P. Lazarenko et al. "Electrical properties of the Ge2Sb2Te5 thin films for phase change memory application". In: *AIP Conference Proceedings*. Vol. 1727. 1. AIP Publishing LLC. 2016, p. 020013.

[141] E. Schreck, R. Fontana, and G. Singh. "Thin film thermocouple sensors for measurement of contact temperatures during slider asperity interaction on magnetic recording disks". In: *IEEE Transactions on Magnetics* 28.5 (1992), pp. 2548–2550.

[142] Y.-M. Chen and P. Kuo. "Effect of Ag or Cu doping on erasable phase-change Sb-Te thin films". In: *IEEE Transactions on Magnetics* 34.2 (1998), pp. 432–434.

[143] C. Alkan et al. "Polyurethanes as solid–solid phase change materials for thermal energy storage". In: *Solar Energy* 86.6 (2012), pp. 1761–1769.

[144] X. Fu et al. "Novel solid–solid phase change materials with biodegradable trihydroxy surfactants for thermal energy storage". In: *RSC Advances* 5.84 (2015), pp. 68881–68889.

[145] F. Xiong et al. "Towards ultimate scaling limits of phase-change memory". In: *2016 IEEE International Electron Devices Meeting (IEDM)*. IEEE. 2016, pp. 4–1.

[146] Q. Cheng et al. "Precise nanoscale temperature mapping in operational microelectronic devices by use of a phase change material". In: *Scientific reports* 10.1 (2020), pp. 1–8.

[147] B. Marchon and Y. Saito. "Lubricant thermodiffusion in heat assisted magnetic recording". In: *IEEE Transactions on Magnetics* 48.11 (2012), pp. 4471–4474.

[148] J. Zhang et al. "Lubrication for heat-assisted magnetic recording media". In: *IEEE Transactions on Magnetics* 42.10 (2006), pp. 2546–2548.

[149] H. Wu et al. "Lubricant reflow after laser heating in heat assisted magnetic recording". In: *Journal of Applied Physics* 117.17 (2015), 17E310.

[150] S. Zhang and D. Bogy. "A heat transfer model for thermal fluctuations in a thin slider/disk air bearing". In: *International Journal of Heat and Mass Transfer* 42.10 (1999), pp. 1791–1800.

[151] D. Chen, N. Liu, and D. B. Bogy. "A phenomenological heat transfer model for the molecular gas lubrication system in hard disk drives". In: *Journal of Applied Physics* 105.8 (2009), p. 084303.

[152] L. M. Jiji. "Microscale conduction". In: *Heat Conduction*. Springer, 2009, pp. 347–401.

[153] M. J. Stirniman, S. J. Falcone, and B. J. Marchon. "Volatility of perfluoropolyether lubricants measured by thermogravimetric analysis". In: *Tribology Letters* 6.3 (1999), pp. 199–205.

[154] B. Marchon et al. "The physics of disk lubricant in the continuum picture". In: *IEEE Transactions on Magnetics* 41.2 (2005), pp. 616–620.

[155] B. Marchon et al. "Lubricant dynamics in the sub-nanometer clearance regime". In: *IEEE Transactions on Magnetics* 43.9 (2007), pp. 3694–3698.